POLITECNICO
MILANO 1863

Dipartimento di Elettronica, Informazione e Bioingegneria

Doctoral Program in Information Technology

Metro network capacity increase via innovative photonic technologies and communication systems

Supervisor:

Prof. Pierpaolo Boffi

Tutor:

Prof. Paolo Martelli

Chair of the Doctoral Programme:

Prof. Barbara Pernici

PhD thesis by:

Mariangela Rapisarda

ID Number 901784

XXXIII CYCLE (2017-2020)

Alla mia famiglia,
faro negli approdi della vita,
sostegno nelle difficoltà.

"Era appena passato il mezzogiorno del 12 dicembre 1901, quando mi portai all'orecchio una metà della cuffia e mi misi ad ascoltare. Sul tavolo dinanzi a me il ricevitore era assai rudimentale, poche spire di filo, qualche condensatore, un conduttore, niente valvole, niente amplificatore, niente galena. Stavo per mettere finalmente alla prova l'esattezza di tutte le mie convinzioni. [...] All'improvviso verso le dodici e mezza, risuonò il secco "clic" del martelletto contro il conduttore, segno che qualcosa stava per succedere. Ascoltavo attentissimo. Evidenti mi suonarono nell'orecchio i tre "clic" corrispondenti ai tre punti dell'alfabeto Morse; ma volevo una conferma per considerarmi pienamente sicuro. «Sente nulla, signor Kemp?», dissi porgendo la cuffia al mio assistente. Kemp sentì, ma non Paget che era un po' sordo. Capii allora che i miei calcoli erano stati perfettamente esatti. Le onde elettriche inviate da Poldhu avevano superato l'Atlantico, ignorando tranquillamente la curvatura della terra che molti increduli stimavano essere un ostacolo insuperabile, ed influenzavano ora il mio ricevitore a Terranova. Compresi allora non essere lontano il giorno in cui avrei potuto inviare veri e propri messaggi senza fili attraverso l'Atlantico"

G. Marconi

Contents

Abstract

In the following years, future Metropolitan Area Networks (MANs) will be required to support a large range of resource-hungry applications, but on the same time they will have to be efficient in terms of cost and energy consumption. This thesis takes into account a modular solution based on Sliceable Bandwidth/Bitrate Variable Transceivers (S-BVTs) developed in PASSION project. The S-BVTs are composed of transmitters constituted of directly-modulated Vertical-Cavity Surface-Emitting Lasers (VCSELs) and coherent receivers. The optimization of the transmission bandwidth is achieved by choosing adaptive modulation formats, such as Discrete Multitone (DMT). A particular focus is put on the hierarchical structure of MANs, especially taking into account the presence of two Hierarchical Levels (HLs): HL4 and HL3. The focus of the work is to analyze the potentialities of S-BVTs in MANs organized in hierarchical levels in terms of transmitted capacity. In order to achieve these results, a MATLAB® simulator has been created to emulate the behaviour of the main MAN network components: the VCSEL and its direct modulation with DMT format, the network nodes, the Standard Single-Mode Fiber (SSMF), and the coherent receiver.

The evaluation of the interplay between laser chirp parameters and tight optical filtering due to a 25-GHz channel spacing Wavelength Selective Switch (WSS) highlights that a source with lower chirp is preferred, but a small amount of chirp is however useful for higher noise levels. Moreover, due to a higher spectral efficiency, Single Sideband (SSB) DMT modulation outperforms

Dual Sideband (DSB) DMT modulation. The dependence of the interchannel crosstalk on the modulating signal bandwidth is proved and a trade-off between the impairments due to the crosstalk and the traffic carried by each channel has to be found. The Volterra equalization algorithm is demonstrated to be useful to mitigate both interchannel crosstalk and fiber non-linear impairments for hundred-km propagation of three 25-GHz spaced channels modulated with SSB DMT signal. The effect of HL4 and HL3 nodes on the transmission performance is evaluated in terms of required Optical Signal-to-Noise Ratio (OSNR) to achieve given target capacities. Real network topologies are considered, and a target capacity of 50 Gb/s per channel per polarization can be reached by optimizing the launch power and the optical amplification in a 170-km scenario. Furthermore, the presence in the network nodes of Semiconductor Optical Amplifiers (SOAs) working as Wavelength Blockers (WBLs) is evaluated in terms of capacity reduction due signal distortion caused by Self-Gain Modulation (SGM) of the amplifier. This nonlinear impairment introduces a high-pass filtering, emphasised for higher saturation conditions. The analysis is performed with two different optical sources, a Distributed FeedBack (DFB) laser and a VCSEL, which are externally and directly modulated respectively. They are modulated both with a DSB and a SSB DMT signal. SSB is more resilient to the distortion due to the SOA filtering for high currents and to the Amplified Spontaneous Emission (ASE) noise introduced by the amplifier in direct modulation systems. At last, the performance of a system composed of a DSB DMT-modulated optical signal crossing a complete HL4 node, *i.e.*, constituted of a channel Demultiplexing (DEMUX) filter, an SOA, and a Multiplexing (MUX) filter, followed by an optical SSB filtering and the addition of two SSB DMT-modulated adjacent channels in a 25-GHz grid is experimentally measured. The three channels propagate for 100 km. In this system a capacity higher than the target 50 Gb/s per channel per polarization is demonstrated.

Sommario

Nei prossimi anni, le future reti metropolitane (MAN) dovranno supportare un numero sempre crescente di applicazioni che richiedono molte risorse, ma nel contempo dovranno essere efficienti in termini di costo e consumo energetico. Questa tesi prende in considerazione una soluzione modulare basata su Sliceable Bandwidth/Bitrate Variable Transceiver (S-BVT) sviluppata dal progetto PASSION. Gli S-BVT sono costituiti da trasmettitori formati da Vertical-Cavity Surface-Emitting Laser (VCSEL) modulati direttamente e da ricevitori coerenti. L'ottimizzazione della banda di trasmissione è ottenuta sfruttando formati di modulazione adattativi, come il Discrete Multitone (DMT). Particolare attenzione è stata posta alla struttura gerarchica delle reti metro, prendendo in considerazione due livelli gerarchici (HL): HL4 e HL3. L'obiettivo del lavoro è valutare le potenzialità dell'uso di S-BVT nell'ambito di una rete MAN organizzata a livello gerarchico in termini di capacità trasportata. Per ottenere questi risultati, è stato sviluppato un simulatore MATLAB® che emula il comportamento dei principali dispositivi costituenti la rete metro: il VCSEL e la sua modulazione diretta con formato DMT, i nodi di rete, la fibra ottica standard a singolo modo e il ricevitore coerente.

La valutazione dell'interazione tra parametri di chirp della sorgente e filtraggio ottico stretto proveniente da Wavelength Selective Switch (WSS) per spaziatura tra canali a 25 GHz evidenzia come parametri di chirp più bassi siano preferibili, ma che, specialmente per livelli di rumore alti, un piccolo quantitativo di chirp sia utile. Inoltre, grazie ad una migliore efficienza spettrale,

il segnale DMT Single Sideband (SSB) mostra una migliore performance rispetto al segnale DMT Dual Sideband (DSB). Si dimostra la dipendenza del crosstalk tra canali dalla banda del segnale modulante, sottolineando la necessità di un compromesso tra deterioramento della performance dovuto al crosstalk e traffico trasportato da ciascun canale. L'efficacia dell'algoritmo di equalizzazione di Volterra è verificata in uno scenario a tre canali spaziati di 25 GHz propaganti per qualche centinaio di chilometri e modulati con DMT SSB. L'effetto del filtraggio dovuto alla presenza di nodi di rete a livello HL4 e HL3 è valutato in termini di rapporto segnale-rumore ottico (OSNR) richiesto per ottenere date capacità target. Sono analizzate due topologie di rete reali e la capacità target di 50 Gb/s per canale per polarizzazione può essere raggiunta ottimizzando la potenza di lancio e l'amplificazione ottica in una rete lunga 170 km. Dunque si considera la presenza nei nodi di rete di amplificatori ottici a semiconduttore (SOA) utilizzati come Wavelength Blocker (WBL) in termini di riduzione della capacità dovuta alla distorsione del segnale ottico causata da Self-Gain Modulation (SGM). Questo effetto non lineare introduce un filtraggio passa-alto, accentuato per condizioni di saturazione alte. L'analisi è condotta con due sorgenti ottiche diverse, un laser Distributed FeedBack (DFB) ed un VCSEL, modulati rispettivamente esternamente e direttamente. I due laser sono modulati con un segnale DMT sia DSB sia SSB. La modulazione SSB si dimostra più resistente sia alle distorsioni introdotte dal SOA ad alte correnti e potenze sia al rumore dovuto all'amplificazione dell'emissione spontanea (ASE) introdotto dall'amplificatore in sistemi a modulazione diretta. Infine si valuta la capacità trasmessa in un sistema costituito da un canale DMT DSB che attraversa un nodo di rete HL4 completo, cioè costituito da un demultiplatore, il SOA ed un multiplatore, seguito da un filtraggio ottico SSB e l'aggiunta di canali adiacenti a 25 GHz, anch'essi modulati con un segnale DMT SSB. I tre canali sono fatti propagare per 100 km. In questo sistema si dimostra una capacità superiore ai 50 Gb/s per canale per polarizzazione.

Introduction

The more and more increasing number of applications which require a huge throughput in transmission are forcing telecommunication researchers to study new solutions for optical networks to cope with this growth. The quantity of devices accessing the Internet are becoming more widespread and cheap, so the traffic generated by users is going to saturate in few years the transmission capacity deployed at the present time. Their mobility induces to introduce flexible and fast solutions to route traffic. Moreover, the climate changes stress the importance of having networks which consume less energy and have a better footprint on the environment. This urgency is valid for both short-reach and long-reach networks. This thesis, which partially falls in the objectives of PASSION project ("Photonic technologies for progrAmmable transmission and switching modular systems based on Scalable Spectrum/space aggregation for future agIle high capacity metrO Networks", see `http://www.passion-project.eu/` for more details), aims at estimating the potentialities of the modular solution for Metropolitan Area Networks (MANs) proposed by PASSION. The main building blocks (transmitter, network nodes, and receiver) are designed to be scalable and flexible thanks to the Software Defined Network (SDN) protocol which controls the Sliceable Bandwidth/Bitrate Variable Transceivers (S-BVTs) constituting the network. This allows to select the wavelengths needed to support the request of resources. The optimization of the transmission bandwidth achieved with the adoption of advanced modulation formats, such as Discrete Multitone (DMT), along

with the employment of several Space Division Multiplexing (SDM) solutions, *e.g.*, MultiCore Fibers (MCFs) or bundles of single-core fibers, increase the available capacity. The geographical and functional hierarchy intrinsic in a metro network is taken into account by designing different network nodes, depending on the level of required traffic aggregation. The linear and nonlinear impairments introduced by the propagation along some hundreds of km of optical fiber, can be partially or totally compensated at the coherent receiver to recover the optical signal and apply proper Digital Signal Processing (DSP) algorithms.

The thesis work is articulated in 5 chapters as follows.

Chapter 1 presents some approaches to increase the transmitted capacity in future resource-hungry MANs.

In Chapter 2 the solution proposed by PASSION in order to increase the transmitted capacity in Metropolitan Area Network (MAN) networks is introduced. Some constituent parts are briefly investigated: the transmitter based on Vertical-Cavity Surface-Emitting Lasers (VCSELs), the network nodes, the multicore fiber, and the coherent receiver.

Chapter 3 gives an overview of the MATLAB® simulator employed in the thesis. Some of optical devices which have been partially introduced in the previous chapter are then studied in terms of algorithms and transfer functions: the optical source (in particular the VCSEL source), the fiber propagation, which takes into account both linear and nonlinear effects, the MAN nodes, and the receiver.

In Chapter 4 some significant simulation results are presented. The simulation tool is validated by comparing the simulated results with the ones

obtained with laboratory experiments. The interplay between the chirp of an optical source and the tight optical filtering introduced by some of the MAN network nodes is studied. The role of interchannel crosstalk on the transmitted capacity is investigated for 25-GHz channel spacing in presence of three adjacent channels generated by VCSELs which are directly modulated with a SSB DMT signal. The effect of nonlinear impairments is experimentally measured in terms of transmitted capacity for a hundred-km network and a solution to mitigate them is presented. The impact of two kinds of MAN nodes (at Hierarchical Level (HL)4 and HL3 levels) is deeply studied. The results obtained from the aforementioned evaluations are preparatory for the simulation of some MAN topologies.

Chapter 5 studies the impact of Semiconductor Optical Amplifiers (SOAs) on the system performance. A brief introduction on the physics of the component is proposed. The role of SOA gain saturation on the transmitted capacity is investigated for a Distributed FeedBack (DFB) laser and a VCSEL, for external and direct modulations and for Dual Sideband (DSB) and Single Sideband (SSB) Discrete Multitone (DMT) modulation format. At last, the SOA is used as Wavelength Blocker (WBL) in an HL4-like node to evaluate the transmitted capacity in a three-channel optical transmission system.

The Conclusions summarize the main results achieved in this thesis and present some proposals to further investigate the thesis topic.

Chapter 1

Future Metropolitan Area Networks

In metropolitan areas high-density population produces and requires huge quantities of data thanks to both fixed and mobile traffic. The traffic request is exponentially increasing, with a Compound Annual Growth Rate (CAGR) of 22% in the 5 previous years (2015-2020) [1] and by 2022 the data volume is foreseen to reach 300 EB per month [2]. In few years, the fiber optic networks will face a bottleneck in transmission and routing of such an amount of data. The combination of Space Division Multiplexing (SDM) and Wavelength Division Multiplexing (WDM) solutions is becoming mandatory to support such high traffic requests to be processed. Roughly speaking, an optical network is a hierarchical structure that can be mainly divided in three levels (see Figure 1.1): the *access networks*, the *metropolitan networks*, and the *long-haul* or *backbone networks* [3].

The *access networks* give connections to the users in close proximity to their service provider. They span some hundreds of meters to few kilometers. They are composed of two parts: the *feeder network*, which connects the *hub* to the *remote nodes*, and the *distribution network*, which links the *remote nodes* to the *Network Interface Units (NIUs)*. A NIU interfaces the networked

devices to the outside network, so it is the closest to the users. The cascade of remote nodes and NIUs allows the connection between the subscribers and the hub, which is for instance a Central Office (CO) and which interconnects the access network and the metropolitan networks [4]. Optical access networks are generally Passive Optical Networks (PONs) [5], where the Optical Network Terminal (ONT) located in the customer premises (CPE) connects first to the Local Connection Point (LCP) and then with the NIU, which, in turn, communicates with the Optical Line Termination (OLT) in the CO. They are "*passive*" since the splitters in the LCP are powerless. The *last mile* of the access network is the well known "*Fiber to the x*" (FFTX), where x can stand for *node*, *curb*, *building* or *home*, depending on the level of penetration of optical fiber technology (*i.e.*, where the optical fiber is interconnected to the copper cable). IEEE and International Telecommunication Union (ITU)-T are standardizing PON nominal line rates beyond 10 Gb/s. The work of IEEE 802.3ca 50G Ethernet Passive Optical Network (EPON) Task Force increased the line rate to 25 Gb/s; ITU-T is doubling this rate, with the objective in mind to reach at least 4 times the rate deployed nowadays, while 100 Gb/s seems a far objective at the moment [6] - [7].

The *metropolitan networks* collect user-generated traffic coming from access networks to route it to the backbone network. They lie within a large city or a region, so they span distances ranging between tens to some hundreds of kilometers. Access networks interface to metropolitan networks though Points of Presence (POPs), which are linked in a ring topology. On the other side, core routers connect the metro networks to backbone networks, and they support up to few Tb/s of switching/routing capabilities. In the core-metro segments, carriers place their COs or lease some portions of them from larger carriers [9]. So, metro networks can be divided in two parts. The first one is the metro access network, which collects the traffic coming from the carrier's customer locations into the carrier's network. The other part is the metro interoffice

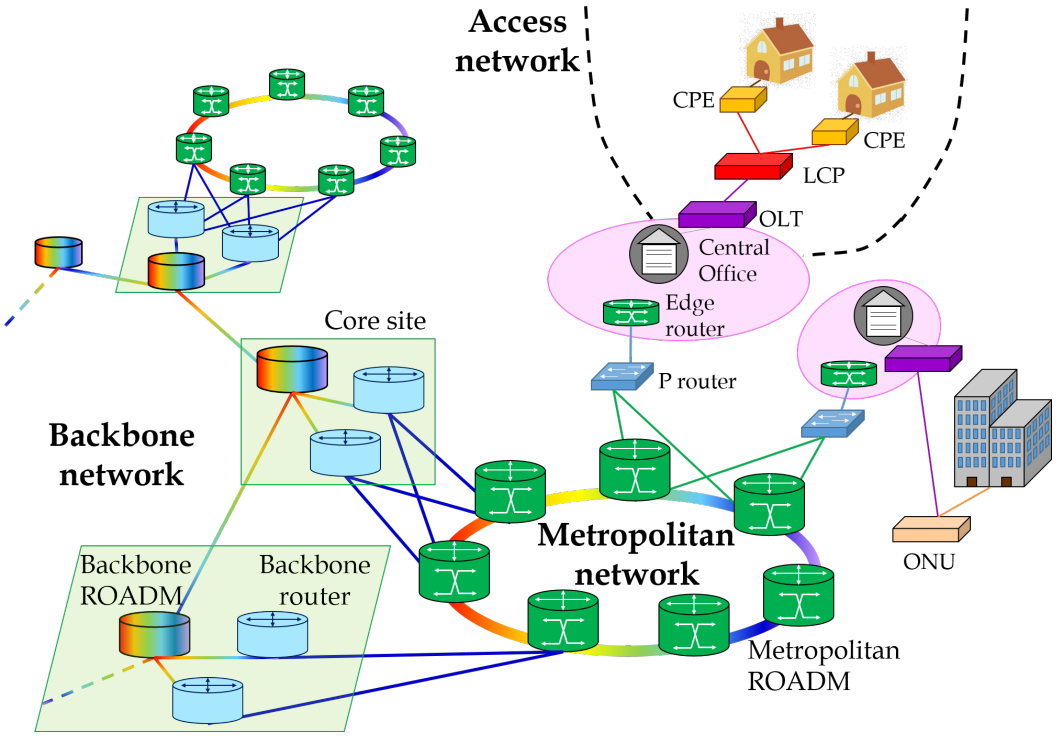

Figure 1.1: Graphical representation of access, metropolitan, and long-haul networks, inspired by the one depicted in [8].

network, which links the metro carrier central offices and then forward the traffic to the backbone network. Metropolitan networks are characterized by spans requiring optical amplification, since they have to recover power lost during propagation along significant transmission lengths: for protection purposes, network architectures are designed to foresee secondary paths, which could be longer than primary, in case of link or node failure of the working path. Moreover, power is dissipated due to lossy add/drop multiplexers and connectors [10].

Figure 1.2 shows the logical hierarchy of metropolitan networks. The logical connections at the IP/MPLS overlay are handled at the transport layer by the Optical Transport Network (OTN) protocol (ITU G.709), which in turn allocates the proper wavelengths through the employment of Reconfigurable Optical Add-Drop Multiplexers (ROADMs). The client signals are directly

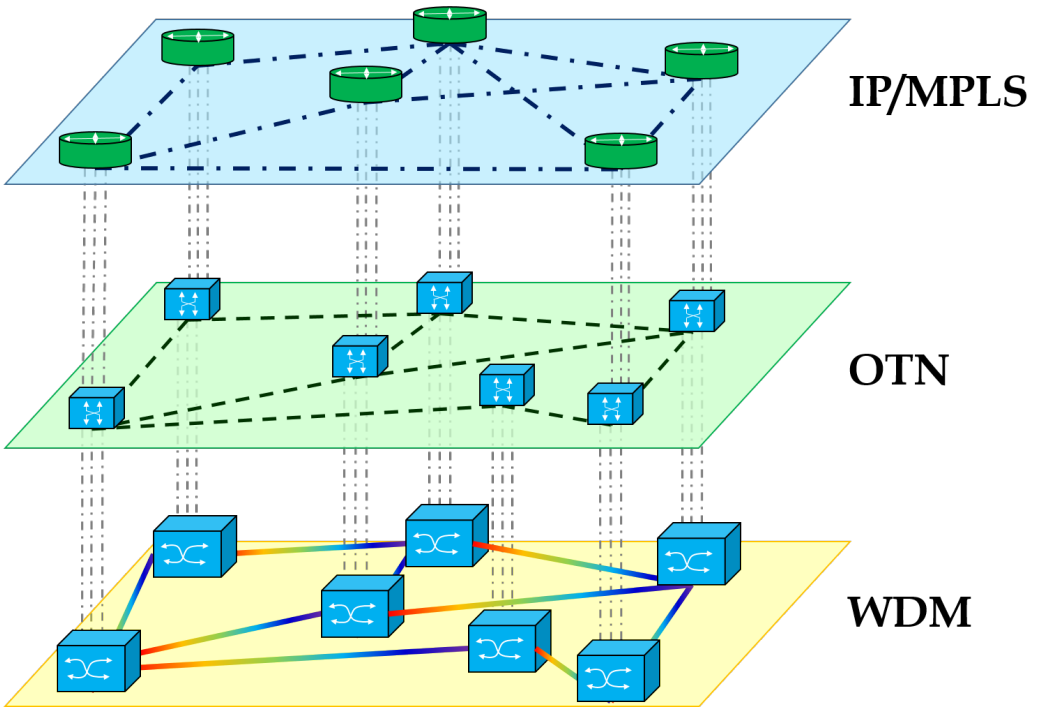

Figure 1.2: Schematic of the three-layer topology of MAN networks, similar to the one shown in [8].

transported over the wavelengths by OTN, which guarantees a digital monitoring as well [8]. The focus of this thesis will be put on the physical layer of MAN networks, so the overlay levels are not taken into account.

The *long-haul* or *backbone networks* span from several hundreds to thousands of kilometers, covering cities and countries around the world. Moreover, long-haul undersea networks perform intercontinental trans-oceanic links, which reach very long distances, and they are usually defined as ultra long-haul networks. For instance, the Asia-America Gateway (AAG) connects the West Coast of the USA to South East Asia and it spans 20,000 km [11]. At national level, intermetro segments connect several metro networks. Such long networks require the signal to be periodically restored. Dense Wavelength Division Multiplexing (DWDM) is widely deployed in long-haul networks to save money for the employment of regenerators. The maximum distance between two consecutive regenerators, namely the *optical reach*, is a fundamental parameter

in the evaluation of long-haul cost effectiveness. A longer optical reach implies the employment of a smaller number of regenerators, reducing the operational costs, but on the other side the equipment, which includes transponders and amplifiers, is more expensive. A trade-off between these two instances has been discussed and the optimal optical reach (between 2500 km and 3500 km) has been identified in [12], which studied four long-haul networks located in North America. Other solutions, such as the installation of rate-adaptable transponders [13], can lower the network costs. With rate-adaptability, the fiber capacity is optimized depending on the fiber route: shorter routes use higher modulation formats, so higher capacities, while longer routes employ lower modulation formats, thus lower capacities. Similarly to metropolitan networks, several logical layers constitute a long-haul network: IP/MPLS, OTN, DWDM just to cite a few [9]. In the first 2000s, it has been demonstrated the transmission of 80 channels in a 50-GHz grid with 10-Gb/s Return-to-Zero (RZ) modulation per channel in the C-band aided by Raman amplification and Forward Error Correction (FEC) for distances up to 3,600 km and amplification spans of 100 km [14] . However, it has been proved the efficiency of Chirped Return-to-Zero (CRZ) modulation formats over Non-Return to Zero (NRZ) and RZ formats; in CRZ formats an amount of phase modulation is added to make the system more resilient to fiber non-linear impairments. This allows to reach 9,000 km for 64 channels in a 0.4-nm grid with 12.3 Gb/s per channel [15]. Recent advances in the technologies has induced an increase of single-fiber capacity from 3.2 Tb/s to 40 Tb/s. With DWDM, up to 96 channels spaced in a 50-GHz grid can be exploited over the extended C-band with a single-channel capacity ranging between 40 Gb/s and 200 Gb/s. A tight control on the stability of the optical sources is required to prevent spectrum distortions due to the DEMUX and MUX filtering. At the moment an accuracy of ± 2.5 GHz is achieved. The exploitation of Four-Dimensional Modulation/Multiplexing, *i.e.*, the employment of in-phase and quadrature components of both X- and

Y-polarizations, increases the spectral efficiency of a factor 4 with respect to single-polarization one-dimensional modulation formats. Moreover, by extending the propagation in the C+L band (from 1528 nm to 1610 nm) the transmitted capacity can be doubled with respect to C-band propagation: for a transmission length of more than 600 km, 20 Tb/s fiber capacity can be achieved in case of Polarization Multiplexed (PM)-16QAM in C-band, while 40 Tb/s fiber capacity can be reached for C+L band and the same modulation format [16].

As already anticipated, the focus on this thesis will be put on MAN networks. In some years they will have to provide a large range of applications and types of connections to the users, such as 5G or UltraHigh Definition (UHD) television which require a huge total throughput in transmission and high routing capabilities. Moreover, they will be composed of elements which will provide flexibility and scalability along with sustainability in terms of reduction of energy consumption, footprint and costs. In fact the changes of traffic distribution in metro networks are faster than in long-haul networks. The WDM networks need to be reconfigurable to guarantee efficiency in the connections. Furthermore, the request of reliable interconnections among large enterprises data centers, which are generally placed in dense metropolitan areas, force to find fast routings in case of failure of a datacenter and/or of a link [10]. Traditional high-capacity approaches rely on ultra-high speed data rate per carrier [17] achieved thanks to Silicon-Photonics (SiPh) devices [18] and on the exploitation of an Ultra-Wideband (UWB) amplification (S-, C- and L-bands) to support hundreds of WDM channels [19].

The transmitted capacity of single-wavelength channels is increased when they are modulated with high-spectral efficiency modulation formats, such as QAM. In order to reduce the costs of production, SiPh is a good choice to guarantee large scale integration and cheaper devices [20]. A transmission capacity up to 321 Gb/s has been achieved for a single-channel generated with a

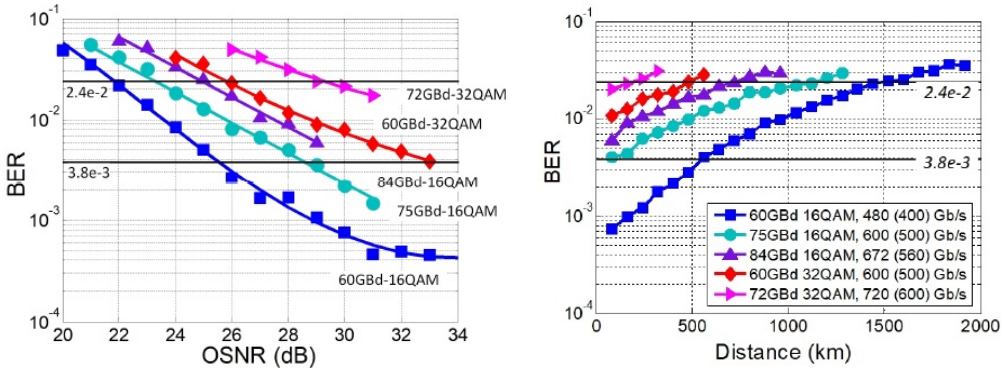

(a) BER dependence on measured OSNR

(b) BER dependence on transmission lengths

Figure 1.3: BER results for different modulation formats, as shown in [17].

tunable laser emitting at 1547.8 nm and externally modulated with a 16-QAM electrical signal by a Silicon In-phase and Quadrature (IQ) modulator [21]. In [22] a dual-carrier transponder module has been presented: it guarantees good performances for QPSK, 8-QAM and 16-QAM modulations, measured in terms of Bit Error Rate (BER) for several wavelengths, temperatures and propagation lengths (up to 3,000 km), with rates up to 400 Gb/s for 16-QAM. A transmitted capacity of 450 Gb/s has been demonstrated for a 1550-nm channel modulated with an Orthogonal Frequency Division Multiplexing (OFDM) signal for a propagation length of 480 km [23]. In [17] a single-channel transmission guarantees up to 720 Gb/s for a 32-QAM transmission. A 1530-nm transmitter with 100-kHz linewidth laser and a booster Erbium-Doped Fiber Amplifier (EDFA) emits a 23-dBm signal, which is externally modulated by an IQ-modulator. It propagates through a transmission loop consisting of a 80-km SSMF, an EDFA, and a Waveshaper, to equalize the gain and partially suppress the ASE noise. The signal power is then set to 6 dBm and the signal is coherently received with a 70-GHz coherent receiver. As shown in Figure 1.3, two modulation formats with different baud rates have been investigated: 16-QAM at 60 GBd, 75 GBd, and 84 GBd, and 32-QAM at

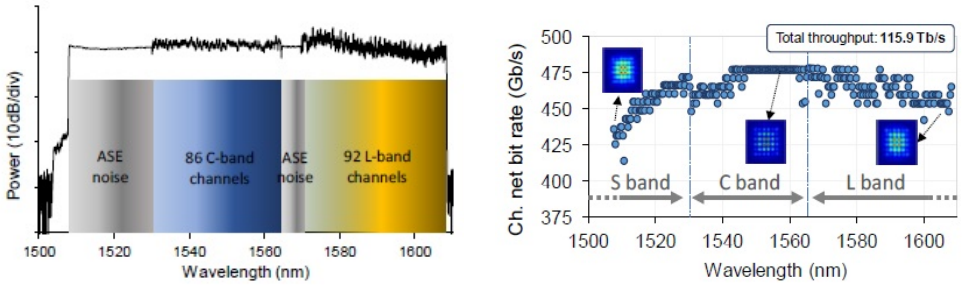

(a) Subcarrier distribution **(b)** Channel throughput

Figure 1.4: Channel distribution and throughput for 100-nm UWB channels, as shown in [25].

60 GBd and 72 GBd, which correspond to a bit rate ranging between 480 Gb/s and 720 Gb/s. Two Forward Error Correction (FEC) codes have been employed: a 7% FEC code with required BER of $3.8 \cdot 10^{-3}$, and a 20% FEC code with required BER of $2.4 \cdot 10^{-2}$. Depending on the employed modulation formats and on the FEC codes, different constraints on the OSNR are imposed to the transmission (Figure 1.3(a)); in this system the minimum acceptable OSNR is 22 dB achieved for 60-GBd 16-QAM and 20% FEC, and the maximum is 33 dB for 84-GBd 16-QAM and 7% FEC. The OSNRs correspond to a maximum reachable distance plotted in Figure 1.3(b). With 60-GBd 16-QAM and 20% FEC, the raw transmission capacity of 480 Gb/s (corresponding to a net capacity of 400 Gb/s, by excluding the overhead) can be achieved for transmission lengths up to 1,520 km, while the highest transmission rate of 720 Gb/s (600 Gb/s net) obtained by using 72-GBd 32-QAM spans up to 160 km. [24] has firstly demonstrated a single-carrier transmission of 600 Gb/s using 48-GBd Polarization Division Multiplexing (PDM)-256-QAM for a transmission length of 100 km.

Another solution to increase the transmitted capacity in a MAN network is to widen the optical communication bandwidth to the S-band (1460 nm - 1530 nm) and the L-band (1565 nm - 1625 nm). In [25] UWB amplification

has been achieved by Semiconductor Optical Amplifiers (SOAs) operating in the range between 1508 nm and 1611 nm (SOAs will be further discussed in Chapter 5 for their deployment as wavelength blockers in MAN nodes). Despite their worse performance in terms of Noise Figure (NF) and signal distortion induced by their nonlinearities with respect to EDFAs, SOAs have been preferred as amplification devices, since they can provide more than 100-nm amplification, while EDFAs are limited to a 5-THz frequency range. [26] demonstrates that SOAs are less impaired by nonlinearities when the power is spread on a high number of channels with respect to single-channel transmission. Moreover, by increasing the number of channels from 32 to 160, the optimal power per channel, in the order of -20 dBm, can be increased by 2.5 dB, leading to a better operation at high SOA input power [27]. These results justify the employment of SOAs in UWB transmissions. In [25] the employed UWB SOA shows a maximum gain of 19.8 dB at 1550 nm, which decreases up to 16.5 dB for lower and higher wavelengths. Output powers of more than 20 dBm can be achieved for injected powers above 0 dBm. As shown in Figure 1.4(a), 250 channels with 50-GHz granularity are transmitted by combining Amplified Spontaneous Emission (ASE) sources and laser channels modulated with Probabilistically-Shaped 64-QAM (PS64QAM) [28]. Figure 1.4(b) demonstrates a maximum throughput per channel of more than 475 Gb/s; a capacity of 115.9 Tb/s is achieved for a 100-km SOA-based propagation [19]. By optimizing the fiber input power, a capacity of 150.3 Tb/s for the transmission of 272 channels PDM-128QAM modulated and with 50-GHz granularity has been demonstrated for a 40-km propagation [29].

The use of silicon-photonics (SiPh) devices and the support of hundreds of WDM channels could be considered attractive solutions to increase the transmitted capacity, but these approaches seem too costly and power-hungry for the future MAN. The proposal of PASSION project, the potentialities of which are analyzed in this thesis, is to exploit a DWDM multichannel

transmission in the C-band characterized by 25-GHz spaced channels modulated with adaptive formats such as Discrete Multitone (DMT). The modularity of transmitters and receivers, along with node flexibility, provides adaptability to the traffic requests, and, thanks to the Software Defined Network (SDN) protocol, to the network conditions. WDM helps reducing the so-called "*opto-electric bottleneck*", *i.e.*, the gap between the optical bandwidth offered by current technologies and the available electrical techniques [8], [30]. Chapter 2 describes in detail the approach proposed by PASSION project and examined in this thesis.

Chapter 2

VCSEL-based S-BVT solution for Metropolitan Area Networks

This chapter describes the fundamental components constituting the MAN architecture developed in PASSION project and taken into account in this thesis. The Sliceable Bandwidth/Bitrate Variable Transceiver (S-BVT) is the main building block of the network, which provides the flexibility and scalability needed by future MAN networks supporting a huge throughput in transmission and high routing capabilities. The basic element of the transmitting part of the S-BVT is the Vertical-Cavity Surface-Emitting Laser (VCSEL), which is shortly illustrated in its main components. This source is supposed to be directly modulated with Discrete Multitone (DMT) signals, so a brief overview on this modulation format is presented. A MAN is organized in a hierarchical structure, which translates in a hierarchy of network nodes, labelled with their Hierarchical Level (HL). The architectures of two different network nodes (HL4 and HL3 nodes) are described. In order to increase the transmitted capacity, Space Division Multiplexing (SDM) techniques, such as the employment of bundle of fibers or of MultiCore Fibers (MCFs), can be implemented. In particular a concise description of MCFs in terms of physical structure, Intercore Crosstalk (ICXT) and multiplexing solutions is presented.

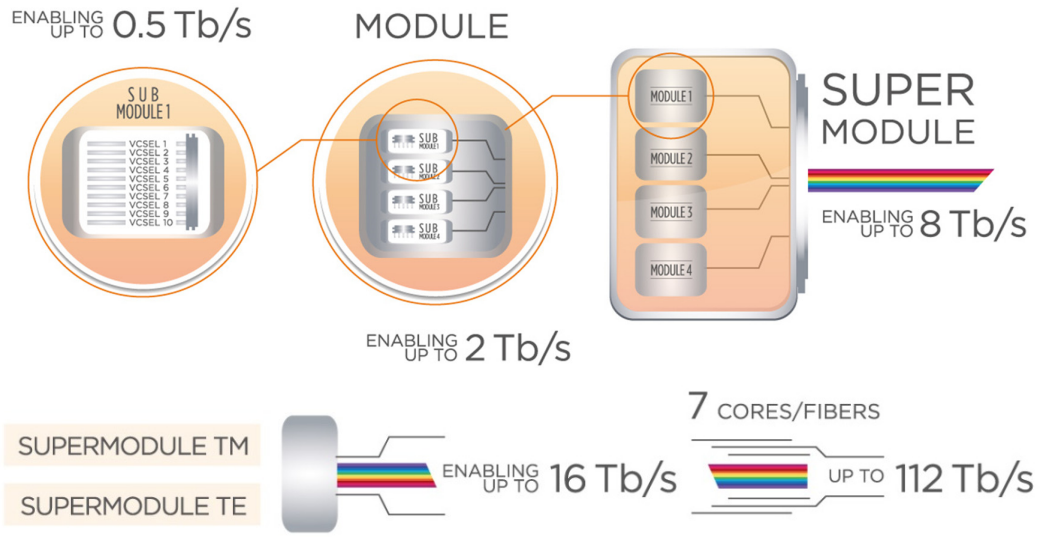

Figure 2.1: Structure of the analyzed S-BVTx as shown in [31].

The Coherent Detection (COH-D) is proposed as the receiving solution for its capability of recovering the signal field and mitigate some impairments such as Chromatic Dispersion (CD), which is significant for MAN distances (hundreds of kilometers). Some DSP algorithms which can be implemented in a digital Coherent Receiver (COH-RX) are introduced.

2.1 A modular network architecture: Sliceable Bandwidth/Bitrate Variable Tranceivers

The increasing request of traffic and routing capabilities makes it mandatory to adopt Sliceable Bandwidth/Bitrate Variable Tranceivers (S-BVTs) or other programmable adaptive transceivers. S-BVTs are sliceable, since they can allocate their capacity in several flows which can reach different destinations. They guarantee adaptability, flexibility, along with scalability, and cost-effectiveness to data center applications and access/metro networks. Multicarrier modulation formats, such as Orthogonal Frequency Division Multiplexing (OFDM) and Discrete Multitone (DMT), provide all these features thanks to DSP,

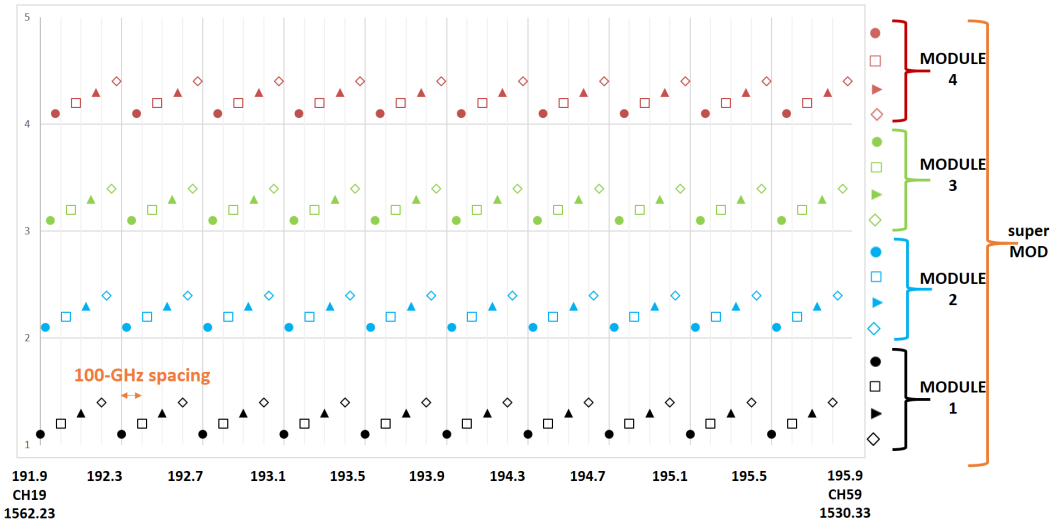

Figure 2.2: Representation of frequency distribution in a supermodule, as depicted in [32].

which enables optical transmissions with broad ranges of granularities, formats, reaches, and rates. Multicarrier formats allow the spectrum of the modulating signal to be manipulated at subcarrier level, and this optimizes the transmitted capacity given a specific demand of traffic, a particular channel condition, or a fixed bandwidth. More details will be provided in Sections 2.1.2, 2.4, and in Chapter 3. S-BVTs are remotely programmable, and they can be integrated in an SDN control plane. The mapping of the high-level operations from an SDN controller into hardware-dependent operations at low level is performed by an SDN agent. SDN implements advanced functionalities for the optimal management of the network resources, *e.g.*, it adapts the rate and the bandwidth of the data signals and it reroutes the traffic in case of network congestion or link failures, just to cite a few.

An S-BVT is composed of Sliceable Bandwidth Variable Transmitter (S-BVTx) and Sliceable Bandwidth Variable Receiver (S-BVRx) arrays [33]. In the reference MAN network at the basis of this thesis [31] the S-BVTx is implemented in a modular fashion. Three elements constitute the S-BVTx: the submodules, the modules, and the supermodules (see Figure 2.1). Each

submodule is composed of 10 VCSELs emitting in the C-band in the range [191.9 THz, 195.875 THz], each one operating up to 50 Gb/s, with a 400-GHz spacing. This leads to enable up to 0.5 THz per submodule. Each module contains 4 submodules in a Silicon-on-Insulator (SOI) chip, leading to 40 VCSELs to be equipped and activated. The generated optical carriers transport a data rate up to 2 Tb/s, when all the sources are licensed, with a channel spacing of 100 GHz. The activation of VCSELs in a Module depends on the supported data rates offered in a node. Within an HL4 node a Module can activate the sources of only 2 Submodules, 50-GHz spaced, leading to an aggregated capacity of up to 1 Tb/s. Four modules form a Supermodule, with 25-GHz granularity. This leads to accomplish up to 8 Tb/s when all the 160 VCSELs are activated, useful at locations demanding large transport capacities (*e.g.*, at HL2/1 nodes). The distribution of frequencies inside a supermodule is represented in Figure 2.2. The transported capacity can be further doubled when both the polarizations (Transverse Electric (TE) and Transverse Magnetic (TM)) are considered. The choice of putting SDM on the top of the system at the transmission medium level can again increase the data rate by a factor equal to the number of fibers in the considered bundle or the number of cores in a MultiCore Fiber (MCF). For instance, considering the activation of all the 160 VCSELs of both the TE and TM supermodules, a capacity of up to 112 Tb/s can be achieved when the signal propagates through a 7-core MCF.

The same modular approach of S-BVTx applies for S-BVRx as well. Each receiving submodule is constituted of a COH-RX equipped with a Local Oscillator (LO). The details about COH-D and its applications for the purposes of this thesis will be more deeply discussed in Sections 2.4 and 3.5.

2.1.1 Vertical Cavity Surface-Emitting Lasers

The mainly exploited source in this thesis is the Vertical-Cavity Surface-Emitting Laser (VCSEL). VCSEL is a kind of laser emitting in the direction

perpendicular to the chip surface. Its active region is composed of a given number of *quantum wells*. A quantum well is a structure in which a thin layer of a semiconductor is comprised between two layers of another semiconductor, differing from the first one in terms of energy gap and refractive index. In particular in the middle layer the electrons in the conduction band have lower energy than in the other two layers. This allows to confine the electrons in the middle layer [34]. The aforementioned gain structure is surrounded by stacks of electrically conductive materials (p-doped and n-doped semiconductors), which form the laser mirrors providing optical positive feedback. The mirrors of the so-generated optical cavity are commonly Distributed Bragg Reflectors (DBRs). A DBR is an alternating structure of two or more different materials. It is based on the principle of transmission and reflection at the interface between two materials with different refractive indexes n_1 and n_2 [35]. A signal propagating along the normal to the interfaces of the DBR encounters two phase shifts: one is due to the propagation through the medium constituting a layer of the mirror and the other is due to the change of refractive index at the interface between two layers. The first contribution $\Delta\phi_L$ depends on the physical thickness of the layer d and on its refractive index n_L:

$$\Delta\phi_L = \frac{2\pi}{\lambda} \cdot d \cdot n_L. \tag{2.1}$$

For instance, if an optical signal at wavelength λ has to encounter a phase shift $\Delta\phi_L = 2\pi$ propagating along a single layer, d has to be designed so that the *optical thickness* $d \cdot n_L = \lambda$. When the signal reaches the interface, a portion R of its power is reflected and the remaining portion $T = 1-R$ is transmitted. It is worth remembering that, for normal incidence, the *reflectance* R depends on the refractive indexes of the two layers n_1 and n_2 as:

$$R = \left|\frac{n_1 - n_2}{n_1 + n_2}\right|^2. \tag{2.2}$$

From Eq. (2.2) it results that a phase-shift $\Delta\phi_{int}$ of π is accumulated when $n_1 < n_2$ and of 2π otherwise. In the design phase, in order to have the desired

high reflectance, proper choices on $\Delta n = n_1 - n_2$, on the suitable number of layers and on their widths have to be performed. More sophisticated structures may contain several different materials or a complex pattern of DBR layers and they can be optimized by proper simulations [36].

The distance between the two mirrors constitute the cavity length L. For planar cavities the wavelengths which can lase have to fulfill the following relation with L in order to constructively interfere [37]:

$$L = \frac{\lambda}{2} \cdot m, \tag{2.3}$$

where m is an integer number. The shortest possible cavity length is $L = \lambda/2$ obtained for $m = 1$. This condition is easy to realize in VCSELs, since the length of the cavity is determined by the epitaxial growth of the cavity itself. $L = \lambda/2$ is an advantageous condition, because it reduces the possible lasing frequencies, and it allows to achieve higher modulation bandwidths and less energy consumption, along with compactness of the device.

While the longitudinal optical signal confinement is achieved through semiconductor mirrors, the transverse confinement has to be guaranteed as well. *Oxide-apertures* are an example of method to induce such a confinement, along with current confinement. Oxide-apertures are created by selectively oxidizing a portion of the DBR layers made by a given material (*e.g.*, oxidizing the $Al_xGa_{1-x}As$ layers in $Al_xGa_{1-x}As - GaAs$ DBRs [38]). In this way, the refractive index of a selectively oxidized portion of the layer differs from the non-oxidized one: the lateral refractive index profile introduces a lateral optical confinement, and the current can be conveyed to a specific active area, reducing the VCSEL threshold current [39]. Other approaches to optical and current confinements have been proposed, each with different advantages and drawbacks: mesa etching of the top mirror [40], ion implantation to create high resistive regions [41], and Buried Tunnel Junctions (BTJs), *i.e.*, junctions made of highly doped n and p semiconductors, at the top of the active region [42]. The electric current is injected from ohmic contacts (pins) placed in the top

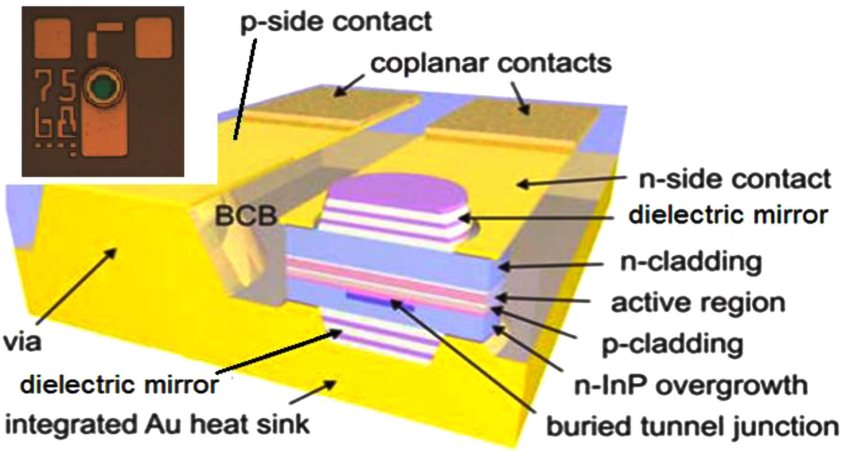

Figure 2.3: Schematic of a 1550-µm for a 18-GHz short-cavity VCSEL, as shown in [46].

epitaxial layer and the backside of the substrate at the bottom of the laser. A VCSEL can emit from either the top layer (through a ring contact [43]) or the bottom layer (thanks to a transparent substrate) [44]. The output power characteristics has a constant slope for currents above the threshold. When the bias current is increased above a given level and/or when the ambient temperature rises, a typical rollover is observed due to internal heating of the device, which causes for instance increased nonradiative recombinations, current and carrier leakages [45]. One advantage of the VCSELs is their compactness, which allows to build 2D arrays, such as the aforementioned S-BVTx.

This brief overview on the VCSELs had the aim of introducing this kind of laser. Depending on the desired emission wavelength, the source layout can adopt different solutions. The source employed in this thesis is shown in Figure 2.3 and it emits in the third fiber window, around 1.55 µm [46], but, since the aim of the work is not focused on the build-up of the component, the specific source employed to achieve the results in Chapter 4 will not be further analyzed in detail.

2.1.2 Discrete Multitone modulation: a solution to bandwidth optimization

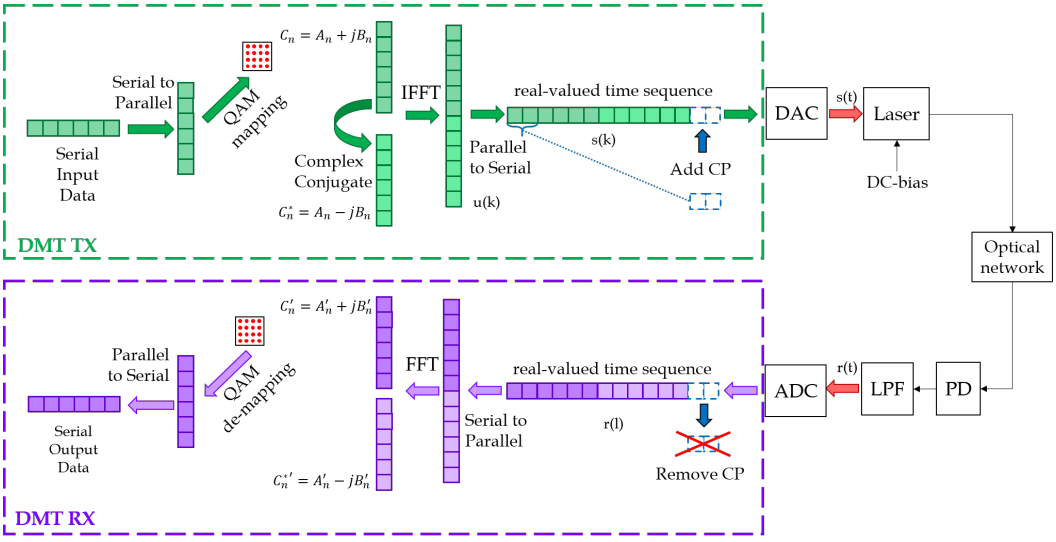

Figure 2.4: DMT scheme for an Intensity-Modulated (IM)/Direct Detection (DD) channel, similar to the one presented in [47]. Low-Pass Filter (LPF) is an anti-aliasing filter.

This is just a brief introduction on DMT. For more details, refer to [47].

DMT is the baseband version of OFDM. It is a multicarrier modulation technique, which, as shown in the block diagram in Figure 2.4, requires the high-speed serial data stream in input to be subdivided into N slower parallel binary streams, labelled with an index $n = 0, 1, .., N-1$, and mapped on an M-ary Quadrature Division Multiplexing (QAM) constellation (where M is the number of bits represented by a symbol $C_n = A_n + jB_n$ of the constellation). After that, the 2^M symbols C_n are modulated onto N subcarriers, each one centred around a specific frequency and orthogonal to each other, which then are simultaneously transmitted. The orthogonality between each couple of subcarriers (k, p) is guaranteed when the distance in frequency is an integer multiple of the inverse of the symbol time T_s [48], *i.e.*,

$$f_k - f_p = \frac{m}{T_s}, \qquad m \in \mathbb{Z}. \tag{2.4}$$

The difference between OFDM and DMT is that the latter's modulator outputs a real-valued signal, not an IQ one after the application of the Inverse Fast Fourier Transform (IFFT). This limits costs and complexity of the system, because DMT transceivers do not demand broadband, analog Radio Frequency (RF) components, as they do instead in OFDM case [49]. In order to generate/capture the DMT signal, only a single Digital to Analog Converter (DAC)/Analog to Digital Converter (ADC) is necessary, leading to a reduction of energy consumption as well. Fast Fourier Transform (FFT) and Inverse Fast Fourier Transform (IFFT) needed for DMT signals require a number of operations which are doubled with respect to OFDM. However, thanks to the real-valued nature of input and output signals of FFT and IFFT, half of these operations can be saved, and this leads the computational complexity to be comparable with the one in OFDM modulation case [50].

As previously stated, the transmission of a real-valued baseband sequence composed of N subcarriers needs a 2N-points IFFT: N inputs are devoted to C_n and the other N are assigned to C_n^*, where * indicates the complex conjugate. For the Hermitian symmetry

$$C_{2N-n} = C_n^*, \qquad n \in [1,\ N-1] \tag{2.5}$$

and the imaginary parts of C_0 and C_N are

$$\Im(C_0) = \Im(C_N) = 0. \tag{2.6}$$

To avoid a DC component, $C_0 = C_N = 0$.

The output $u(k)$ of the IFFT can be expressed as

$$u(k) = \frac{1}{\sqrt{2N}} \sum_{n=0}^{2N-1} C_n \exp\left(j2\pi n \frac{k}{2N}\right), \quad k \in [0,\ 2N-1]. \tag{2.7}$$

It can be demonstrated that it is always real-valued; in fact

$$\begin{aligned} u(k) &= \frac{1}{\sqrt{2N}} \sum_{n=0}^{N-1} \left(C_n \exp\left[j2\pi n \frac{k}{2N}\right] + C_n^* \exp\left[j2\pi\,(2N-n)\,\frac{k}{2N}\right]\right) \\ &= \frac{1}{\sqrt{2N}} \sum_{n=0}^{N-1} 2 \cdot \Re\left(C_n \exp\left[j2\pi n \frac{k}{2N}\right]\right) \quad k \in [0,\ 2N-1]. \end{aligned} \tag{2.8}$$

In order to reduce InterSymbol Interference (ISI), a Cyclic Prefix (CP), *i.e.*, a replica of the last N_{CP} bits of $u(k)$, is added before the DAC operation. The length N_{CP} of the cyclic prefix has to be properly chosen to trade-off the necessity to protect the symbols from ISI with the reduction of overheads which do not carry useful information. The sequence $s(k)$, which is $u(k)$ with the addition of CP, can be represented with the following equation:

$$\begin{aligned} s(k) &= \frac{1}{\sqrt{2N}} \sum_{n=0}^{2N-1} C_n \exp\left(j2\pi n \frac{k - N_{CP}}{2N}\right) = \\ &= \frac{1}{\sqrt{2N}} \sum_{n=0}^{2N-1} C_n \exp\left[j2\pi n \frac{(k - N_{CP})\,\Delta t_s}{T}\right],\ k = 0, 1, ..., 2N - 1 + N_{CP}, \end{aligned} \tag{2.9}$$

where Δt_s is the DAC sampling period, and $T = (2N + N_{CP}) \cdot \Delta t_s$ is the period of a DMT frame.

The received frame $r(t)$ before ADC is

$$r(t) = \sum_{k=0}^{2N-1+N_{CP}} s(k) p(t - k\Delta t_s), \tag{2.10}$$

where the pulse-shaping function $p(t)$ is represented as

$$p(t) = \delta(t) * h(t) = \int_{-\infty}^{+\infty} \delta(\tau) h(\tau - t) d\tau, \tag{2.11}$$

and $h(t) = h_{DAC}(t) * h_{ch}(t) * h_f(t)$ is the impulse response of the cascade of DAC ($h_{DAC}(t)$), channel ($h_{ch}(t)$), and low-pass, anti-aliasing filter ($h_f(t)$) before ADC operation.

To receive and demodulate properly the DMT frames, two requirements have to be fulfilled:

1. in order to avoid inter-frame interference, the length of the frame without CP should be at least equal to the time length of $h(t)$;

2. N_{CP} has to be set to a value guaranteeing that its time period is at least equal to the duration of $h(t)$.

Assuming that the sampling frequency of the ADC is the same as the acquisition frequency of the DAC (so no frequency offset is introduced), the DMT signal after the digital conversion can be expressed as

$$r\left(l\Delta t_s\right) = \sum_{k=0}^{2N-1+N_{CP}} s(k)p\left[\left(l-k\right)\Delta t_s\right]. \tag{2.12}$$

$r\left(l\Delta t_s\right)$ is composed of 2N points, since efficient demodulation is achieved with a 2N-point FFT. The FFT demodulation of $r(l\Delta t_s)$ and the removal of the CP lead to the estimation of the transmitted values C_n as

$$\hat{C}_n = \sum_{l=N_{CP}}^{2N-1+N_{CP}} r\left(l\Delta t_s\right)\exp\left[-j2\pi\left(l-N_{CP}\right)\frac{n}{2N}\right]. \tag{2.13}$$

By substituting Eq. (2.12) in Eq. (2.13) and naming H_n the 2N-point FFT of $h(t)$,

$$\hat{C}_n = H_n \cdot \sum_{k=0}^{2N-1} u(k)\exp\left(-j2\pi k\frac{n}{2N}\right) = \left|H_n\right|\cdot\exp\left(-j\phi_n\right)\cdot C_n. \tag{2.14}$$

In order to estimate H_n, composed of its amplitude $|H_n|$ and its phase shift $\exp\left(-j\phi_n\right)$, a preamble, with known values, is exploited, as it will be further discussed in Chapter 3. The transmitted symbols can then be recovered by multiplying $\hat{C}_n$ with $1/H_n$ with an operation named one-tap, zero-forcing, frequency-domain equalization.

2.2 Hierarchical topology and network nodes

In this thesis a layered MAN topology is taken into account [52]. A MAN network layout combines ring-star topologies; a *ring* is composed of nodes of the same layer, while a *star* aggregates in each node at level L traffic from nodes of the lower layer *L-1*. In Figure 2.5 the logical topology at the Internet Protocol (IP) layer of a MAN network is depicted. Four subnetworks can be identified:

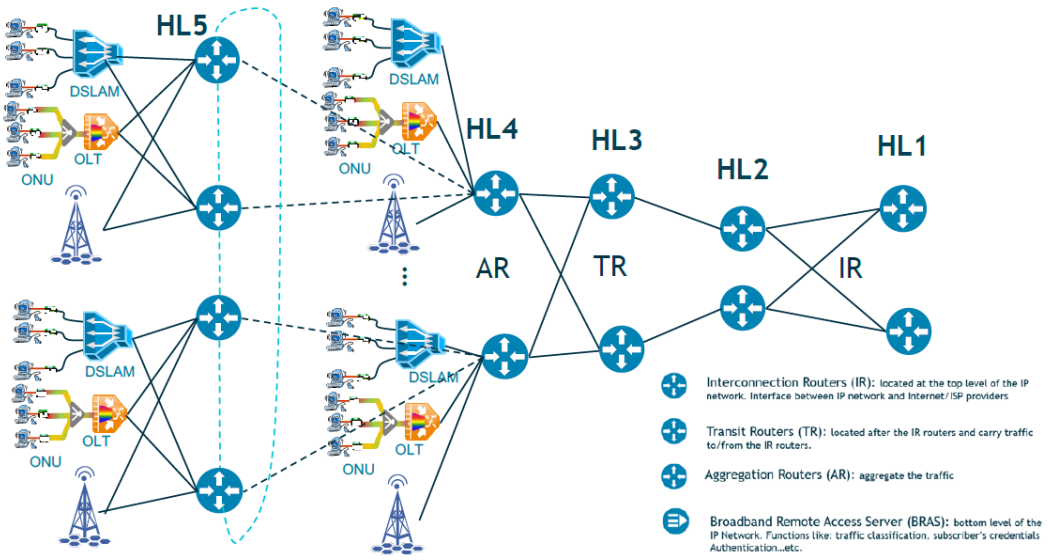

Figure 2.5: Schematic of the IP layer hierarchy, as shown in [51].

1. Access network;
2. First level of aggregation;
3. Second level of aggregation;
4. Core.

This diversification is reflected in the different Hierarchical Levels (HLs) which can be identified in an optical network:

1. HL5: it constitutes the access layer of the network. It is composed of routers, Optical Network Terminals (ONTs), Central Offices (COs), and Base Stations (BSs);
2. HL4: it is the bottom layer of the IP network. It classifies the traffic, it provides the authentication of the subscriber's credentials, it routes data to their destination, to cite some applications. Furthermore, it aggregates the traffic coming from different locations of the MAN, or from Optical Line Terminations (OLTs), and Digital Subscriber Line Access Multiplexers (DSLAMs);

3. HL3: at this level, the traffic coming from different geographical areas of the MAN, *i.e.*, from different HL4 nodes, is aggregated and distributed;

4. HL2/1: the traffic is no more aggregated, but it is just distributed. HL2 nodes forward the traffic to the correct HL2 or HL1 node. HL1 routers make up the top level of the IP network, and they constitute the interface between the IP network and the Internet Service Provider (ISP).

This terminology can be applied to both the IP and the optical layers. In fact, each optical node has at least one co-located router, which aggregates and/or distributes the IP traffic. There is an one-to-one correspondence between the aforementioned subnetworks and the HL. The hierarchy of the network nodes reflects a hierarchy in the geographical areas, from a user-centered zone to an entire nation. In this thesis the focus is put on the architecture of nodes at HL4 and HL3 levels. In the following discussion the HL5 nodes are neglected, while the presence of HL2/1 nodes is taken into account considering them as HL3 nodes, since they are supposed to have a similar physical structure.

As for the S-BVTs, the network nodes have to provide flexibility in the allocation of resources and they have to be scalable, *i.e.*, they have to increase their performance when required. This task is performed by the SDN paradigm, which works as a control to make the MAN network more intelligent. The objective of this thesis is not focused on the logical part of the network, so the presence of SDN and its implementation in the MAN network in analysis will not be further investigated.

2.2.1 HL4 node

The schematic of an HL4 node proposed by PASSION project is represented in Figure 2.6 [53]. An Arrayed Waveguide Grating (AWG) at the node input acts as a demultiplexer of the traffic at HL4 level. The portion of traffic which

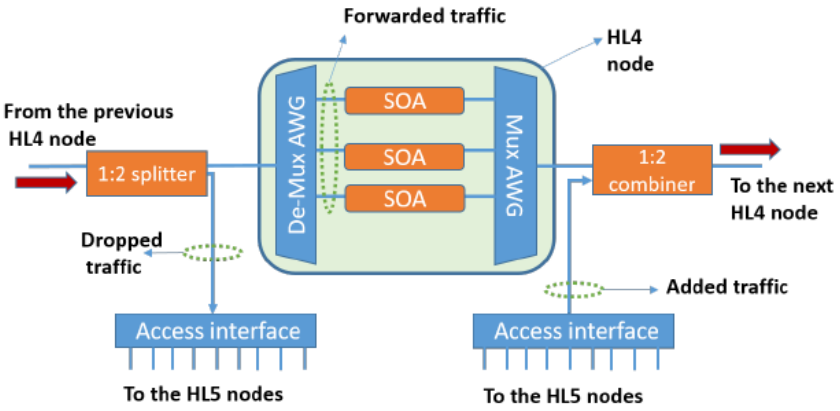

Figure 2.6: Schematic of a HL4 node [31].

has to reach the HL5 nodes is instead selected and dropped by a 1:2 splitter. The operation of add and drop of the channels, which are 50-GHz spaced, is performed by a gate of Semiconductor Optical Amplifiers (SOAs) working as Wavelength Blockers (WBLs). The wavelengths to forward to the following node (another HL4 node or a higher level node) cross the node by turning the amplifiers on; the traffic to be dropped is blocked by turning off the SOA gate switches. The SOA amplifier and its iteration with DMT modulation will be studied more in depth in Chapter 5.

2.2.2 HL3 node

Figure 2.7(a) shows the schematic of an HL3 node developed by PASSION project [54]. The interconnections between HL3 nodes or between an HL3 and an HL2/1 node are performed via MCFs, which are interfaced with SSMF thanks to a Fan-In or a Fan-Out structure. The Photonic Switch (PS) forwards the traffic either to be sent to the following HL3 or HL2/1 node or to be dropped (to the lower HL4 node or to the same HL3 node). The add and drop of the channels at HL3 level is performed with a symmetric structure represented in Figure 2.7(b). The 25-GHz channels are de-interleaved in two stages: the first stage de-interleaves the channels with 25-GHz spacing, and

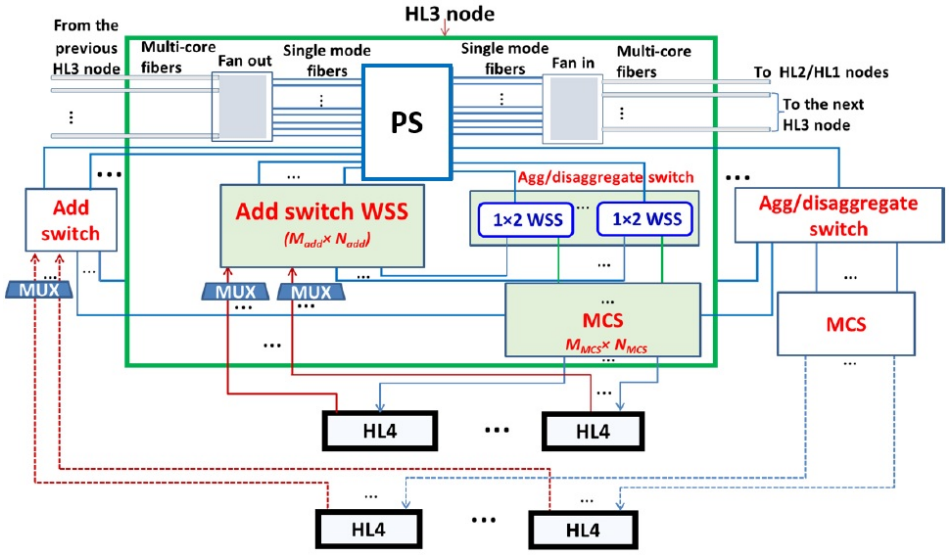

(a) Schematic of an HL3 node, as shown in [54].

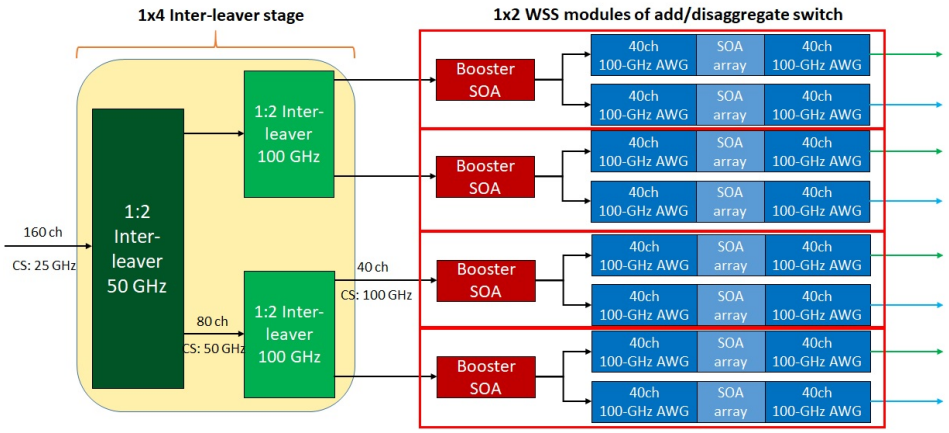

(b) Schematic of HL3 drop mechanism, where the green arrows indicate a polarization and the blue arrows stand for the other polarization.

Figure 2.7: Schematic of a HL3 node, along with the channel add/drop mechanisms [54].

it generates two multichannel signals with 50-GHz spacing, and the second de-interleavers output two signals each with 100-GHz channel spacing. A booster SOA amplifies the signals, before the filtering by a DEMUX AWG. The SOA array plays the same role of WBL as in HL4 nodes. The selected channels are then multiplexed and sent to the HL4 node to be aggregated or to stay in the HL3 node to be added again. In this last case, the signal is said to *recirculate*: a channel is selected by the PS to be dropped and then it is added again. So it crosses the add/drop structure twice. The effect of recirculation will be discussed more in depth in Chapter 4. The channels coming from a previous HL3 node which are destined to the following HL3 node or an HL2/1 node pass over the PS through the *express ports*. The add/drop functionality adds a filtering to the channels (which will be discussed in Section 3.4), while the channels in *express path* are not filtered, and in this thesis they are supposed to be forwarded to the next node unaffected by the presence of the HL3 node [54].

2.3 Space Division Multiplexing transmission solution: Multicore Fiber

A MultiCore Fiber (MCF) consists of a two-dimensional array of cores, commonly distributed in a hexagonal structure to maximize the core density given a cladding diameter. Figure 2.8 depicts the schematic of a 7-core Trench-Assisted Multicore Fiber (TA-MCF), with one central core and six outer cores. The central core suffers the highest level of crosstalk, because it has 6 neighbours, while the outer cores are adjacent to only three other cores. The central core diameter is equal to d and the outer cores diameters deviate from this value of the small amount δ. Λ is defined as the *core pitch*, *i.e.*, the distance between two neighbouring cores. The value of Λ is responsible for the amount of ICXT. In this image, each core is enclosed in a trench to reduce

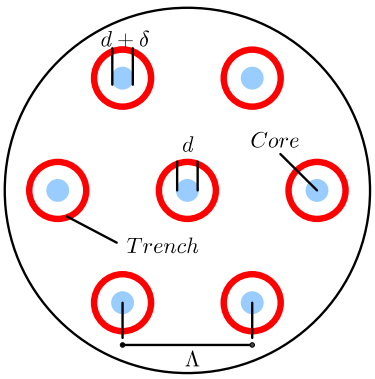

Figure 2.8: 7-core TA-MCF overall core.

ICXT, but this choice of surrounding is arbitrary. The limit on the maximum diameter of the MCF is imposed by the risk to face fractures; this physical boundary restrains the feasible number of cores. A transmission over a 32-core Single Mode Multicore Fiber (SM-MCF) has been demonstrated in [55]. An important characterization concerns the cores of the MCF [56]:

- *homogeneous* MCF: all cores are identical one the other; core-to-core distance determines the core density, which in turn guarantees acceptable values of crosstalk during propagation;

- *heterogeneous* MCF: the cores are not all equal one to the other in terms of propagation constants and refractive indexes. The power transferred among different kinds of cores significantly decreases; this is the reason why this kind of MCF is more efficiently packed than the homogeneous case: non-identical cores are packed in order to reduce the ICXT [57].

MCF cores can carry either one single mode or more modes (Few-Mode Multicore Fibers (FM-MCFs) or MultiMode Multicore Fibers (MM-MCFs)). There are disadvantages in increasing the number of modes propagating through each core:

1. the confinement factor of higher-order modes and the bending loss of the higher-order modes are larger than for the lower-order modes;

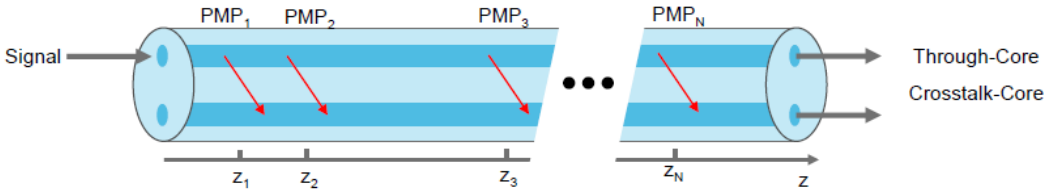

Figure 2.9: Pictorial description of ICXT in homogeneous MCF, which highlights the presence of PMP, as shown in [60].

2. multiplexing and demultiplexing introduce more losses.

MM-MCFs have been demonstrated to carry up to 45 modes [58]. This allows to reach capacities up to 10 Pb/s, considering a transmission in the C+L band [59].

ICXT in homogeneous fibers can be assumed to be concentrated in discrete points along the fibers, named Phase-Matching Points (PMP)s. The total ICXT can be estimated as the sum of the crosstalk contributions arising from the PMPs properly weighted by a random phase shift and their propagation delays (see Figure 2.9). For this reason, homogeneous MCF ICXT can be considered as a noise-like randomly distributed signal [61] - [62]. It shows a stochastic behaviour in time and modulation frequency for Continuous Wave (CW) and signals with a strong carrier [60]. Its average value M_{ICXT} can be approximately computed as [63]

$$M_{ICXT} = 2\kappa^2 \cdot R \cdot \frac{L}{\beta\Lambda}. \tag{2.15}$$

It depends on several fiber parameters, such as the core pitch Λ, the interchannel skew (*i.e.*, the spread of propagation time among channels), the Chromatic Dispersion (CD) variation, and the employed modulation formats. A CW signal can induce a variation in time of the crosstalk by tens of dB. The fluctuations show a different behaviour in period and magnitude when different core combinations are taken into analysis. This is due to differences in the propagation constants of the cores, in the coupling mode coefficients,

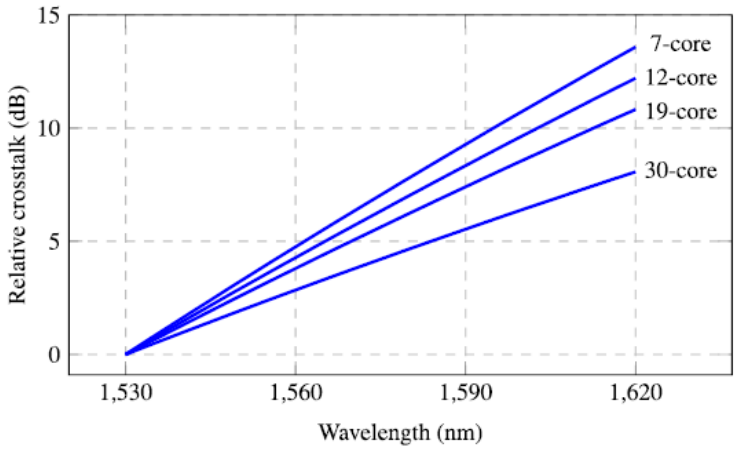

Figure 2.10: Dependence of relative ICXT on wavelength for 7-core, 12-core, 19-core and 30-core MCF, with Λ equal to 50 μm, 45 μm, 40 μm, and 30 μm respectively, as shown in [66].

and in the geometry of the fiber [64]. Modulation formats such as 4PAM or OOK produce ICXT with temporal behaviour similar to CW light [65]. In order to mitigate this effect, multicarrier formats, such as OFDM or DMT, can be employed [67]. The adaptivity of bit- and power-loading algorithms (see Section 3.1.2.1) compensates for the effect of ICXT by assigning higher modulation formats to less impaired subcarriers. The fiber geometry and the value of Λ impact on the average ICXT. By enlarging the core pitch, ICXT significantly decreases. A 15-dB reduction is demonstrated for a 22-core fiber [68] when the cores of the same ring have a core pitch $\Lambda_1 = 42$ μm and the core pitch among rings is $\Lambda_2 = 49$ μm. Another parameter impacting on the ICXT is the bending radius of the fiber, even if recent studies on a 2-km MCF spooled with 16-cm radius compared to a straightened one have demonstrated that the bending radius contribution is limited (<-53 dB) [69]. ICXT is conditioned by the signal wavelength, since both the mode-coupling and the propagation constants depend on it. The ICXT level intensifies by increasing the wavelength; as shown in Figure 2.10, the wavelength has a more significant impact for a MCF characterized by few cores, even if the core pitch

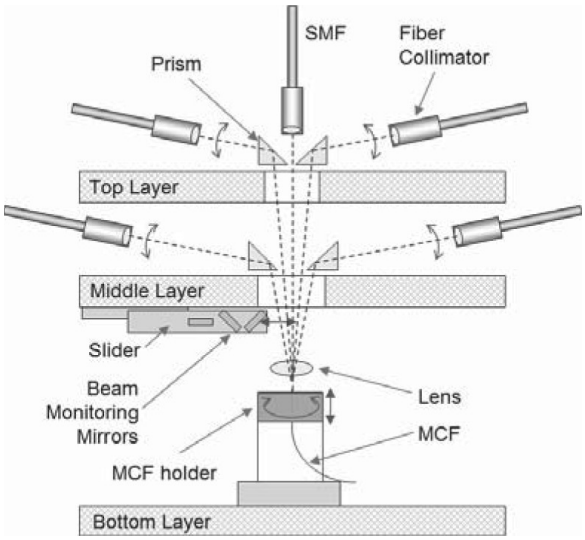

Figure 2.11: Cross-sectional view of the 19-channel coupling device for a 19-core MCF, as presented in [71].

is higher [66]. The lowest reported ICXT in literature for a homogeneous MCF is approximately 64.7 dB/100 km [70].

For SDM transceiver purposes, each core has to be separately addressed. MUX and DEMUX devices interface the MCF cores with SSMFs. Several technologies have been implemented to achieve this task, and some of them are here summarized. A free-space bulk optical device, which is based on prisms to couple light into each core of a 19-core MCF, is shown in Figure 2.11 [71]. It demonstrates an average Insertion Loss (IL) of 1.3 dB, with a variation of ± 0.2 dB across all 19 channels. It is a very flexible device, since it can be adapted to several MCF designs, but, due to its dimensions (more than 40 cm of height) it can be difficultly integrated in a telecommunication system.

Another solution is the fan-in/fan-out device. It is composed of a bunch of SSMFs stacked together, while the MCF placed in a v-groove is spliced to the SDM MUX. Figure 2.12 shows the schematic of a fan-in for a 12-core MCF [72]. The mismatch in the effective area A_{eff} between the MCF cores and the SSMF and the misalignment between them can cause losses at the splice between the fan-in/out and the MCF (*e.g.*, an IL of at most 2.9 dB has been

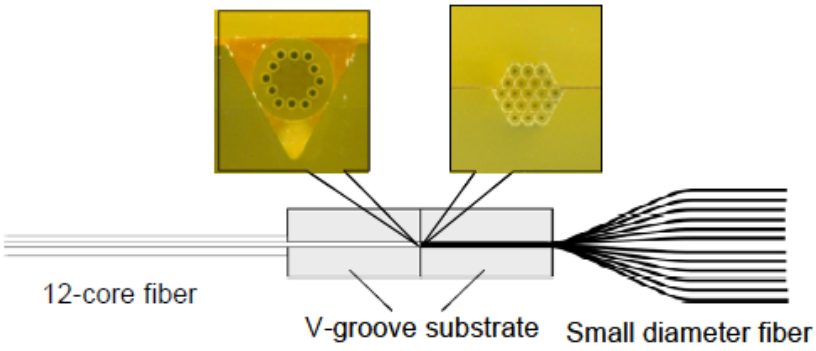

Figure 2.12: Fan-in device for a 12-core TA-MCF, as shown in [72].

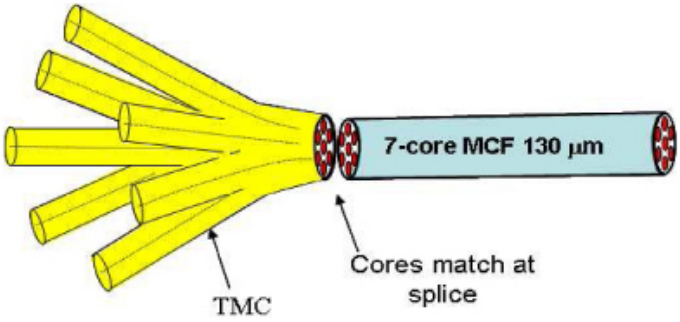

Figure 2.13: Fiber taper device for a 7-core MCF, as shown in [74].

demonstrated for a TA-MCF [72]). An IL of 1.2 dB has been demonstrated for a 7-core TA-MCF 8-m long [73]. Once designed and implemented, it is strictly specific to a given MCF geometry, so it is not an adjustable device.

Another SDM MUX device is the tapered fiber bundle method, which consists in tapering the SSMFs composing the device together to match the core distribution of the MCF. An example is shown in Figure 2.13 [74]. This device introduces an IL between 0.38 dB and 1.8 dB. As for the fan-in, this component is strictly related to the specific geometry, which has to be hexagonal, since the tapered fibers spontaneously distribute in a hexagonal pattern.

Ultrafast laser inscription is a method to create a 3D waveguide integrated fan-in/fan-out device to address single SSMF placed on a v-groove [75]. It is inscribed in a glass substrate by changing its refractive index with a femp-

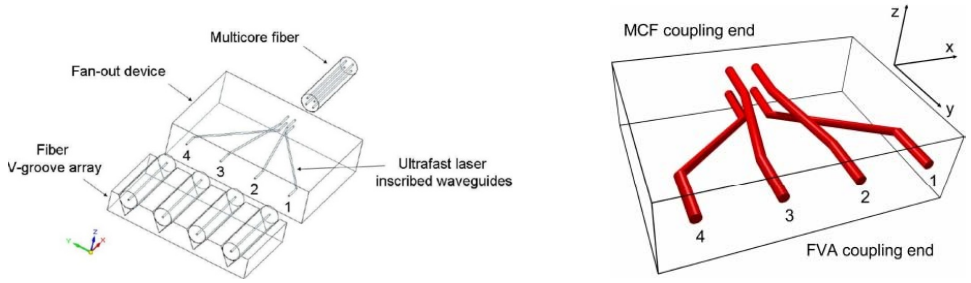

(a) Sketch of the device with MCF **(b)** Graphical representation of the device

Figure 2.14: Example of waveguide integrated MUX through ultrafast laser inscription, as shown in [75].

tosecond pulse laser to draw the optical waveguides (see Figure 2.14). Each waveguide is directly connected to a core of the MCF, so the position of the waveguides is designed to perfectly match the lattice of the cores. Moreover, this device is addressed for single-mode MCF. Both these characteristics, along with a high IL (5 dB), make this setup a solution of little flexibility which can be difficultly employed for practical applications.

2.4 Coherent detection and algorithms for signal recovery

As anticipated in Section 2.1, Coherent Detection (COH-D) has been chosen by PASSION project, and so in this thesis, as detection method for MAN networks [77]. Thanks to COH-D, the full electric field, containing both amplitude and phase information, is recovered. This allows, by using a digital coherent receiver, to apply several algorithm to retrieve the optical signal and compensate for time-varying impairments. On the other way round, with DD the loss of information on the signal phase due to the detection of the intensity of the signal prevents the compensation of Chromatic Dispersion (CD) (which will be discussed in Sections 3.1.1.2 and 4.2) and of Polarization Mode

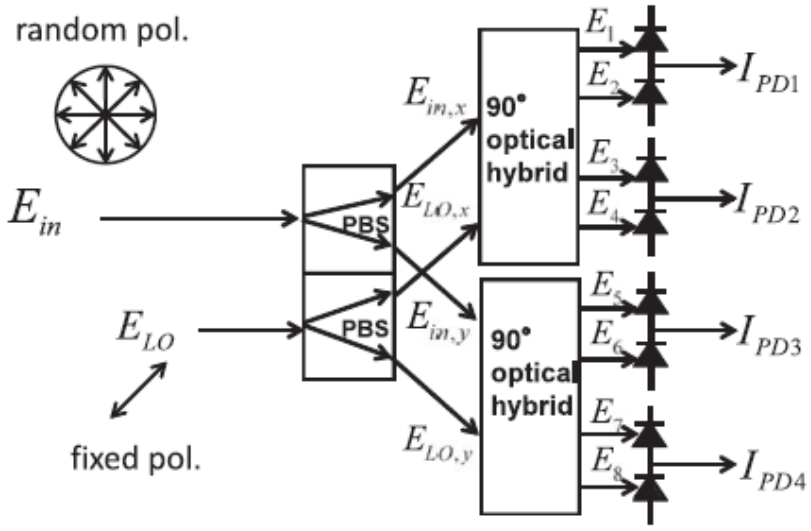

Figure 2.15: Block scheme of a homodyne receiver employing phase and polarization diversities, as shown in [76].

Dispersion (PMD), and it is unfeasible to use it for the propagation lengths of MAN networks.

In a Coherent Receiver (COH-RX), the signal interferes with a Local Oscillator (LO) to extract the phase information. The in-phase (I) and quadrature (Q) components of a carrier are restored [78]. Moreover, the State of Polarization (SOP) of the signal is recovered. In COH-D, the electric fields of the signal and the LO are multiplied. Supposing to have the signal and the LO aligned in polarization, the complex electric field $E_s(t)$ of the signal s can be expressed as the product of a complex amplitude $A_s(t)$ and a phase component depending of the frequency f_s

$$E_s(t) = A_s(t) \cdot \exp(j2\pi f_s). \tag{2.16}$$

Its real component is indicated as

$$\mathcal{E}_s(t) = \Re\{E_s(t)\}. \tag{2.17}$$

Analogous expressions can be obtained for the LO, so

$$E_l(t) = A_l(t) \cdot \exp(j2\pi f_l) \tag{2.18}$$

and

$$\mathcal{E}_l(t) = \Re\{E_l(t)\}, \tag{2.19}$$

where $E_{l(t)}$ and $\mathcal{E}_l(t)$ are the complex electric field of the LO signal and its real component respectively. The signal and LO powers P_s and P_l correspond to the amplitudes $A_s(t)$ and $A_l(t)$. Figure 2.15 depicts the scheme of a homodyne receiver employing phase and polarization diversities, which is the model of receiver employed in the simulation tool described in Chapter 3. The term *"homodyne"* refers to the case in which the LO frequency is the same of the signal, so the intermediate frequency is $f_{IF} = |f_s - f_l|$ is equal to zero. In order to suppress the CW component and mitigate the noise, a balanced COH-D is employed. In a balanced COH-D, each signal component (either I or Q) is detected with a couple of photodiodes after having provided a phase shift of 180° to either the signal or the LO [79]. The electric fields impinging on the couple of photodiodes recovering the in-phase component of the signal are respectively

$$E_1^I(t) = \frac{1}{2}\left(E_s(t) + E_l(t)\right) \tag{2.20}$$

and

$$E_2^I(t) = \frac{1}{2}\left(E_s(t) - E_l(t)\right), \tag{2.21}$$

where the apex "I" stands for "*in-phase*". The output photocurrents are then

$$\begin{aligned} I_1^I(t) &= R \cdot \left[P_s + P_l - 2\sqrt{P_s \cdot P_l} \cdot \cos\left(2\pi f_{IF} t + \vartheta_s(t) - \vartheta_l(t)\right)\right] \\ &= R \cdot \left[P_s + P_l - 2\sqrt{P_s \cdot P_l} \cdot \cos\left(\vartheta_s(t) - \vartheta_l(t)\right)\right] \end{aligned} \tag{2.22}$$

and

$$I_2^I(t) = R \cdot \left[P_s + P_l + 2\sqrt{P_s \cdot P_l} \cdot \cos\left(\vartheta_s(t) - \vartheta_l(t)\right)\right], \tag{2.23}$$

where R is the responsivity of the photodiode, and $\vartheta_s(t)$ and $\vartheta_l(t)$ are the phases of the transmitted and LO signals. The I signal component at the output of the balanced detector can be expressed as

$$I^I(t) = I_1^I(t) - I_2^I(t) = R\sqrt{P_s \cdot P_l} \cdot \cos\left(\vartheta_s(t) - \vartheta_l(t)\right). \tag{2.24}$$

The quadrature component can be obtained in the same way. The electric field of the LO is shifted in phase by $\pi/2$ by a 90° optical hybrid, which implements the phase diversity of the COH-RX [80]; so the output fields of the couple of photodetectors are

$$E^{Q}_{1/2}(t) = \frac{1}{2}\left(E_s(t) \pm jE_l(t)\right), \tag{2.25}$$

and the correspondent output of the balanced detector is

$$I^{Q}(t) = R\sqrt{P_s \cdot P_l} \cdot \sin\left(\vartheta_s(t) - \vartheta_l(t)\right). \tag{2.26}$$

The complex amplitude $I_c(t)$ can be restored as the sum of Eqs. (2.24) and (2.26):

$$I_c(t) = I^{I}(t) + I^{Q}(t) = R\sqrt{P_s \cdot P_l} \cdot \exp\left(\vartheta_s(t) - \vartheta_l(t)\right). \tag{2.27}$$

The effect of the homodyne receiver is a down-conversion of the recovered signal to the baseband. Moreover, this structure allows to compute simultaneous IQ measurements [76]. Since it is implausible that the polarizations of the signal and of the LO remain aligned, two phase-diversity receivers are combined, one per orthogonal linear polarization state. The polarization diversity configuration adds a Polarization Beam Splitter (PBS) to the phase-diversity receiver, so that the incoming signal is decomposed in the two polarization components, which are detected through the homodyne receiver with the same LO [81].

COH-D provides a great flexibility in the modulation formats, because the information is encoded in the in-phase (I) and quadrature (Q) components of the complex signal [82] - [83]. This fulfills the requirements asked to S-BVT solution already introduced in Section 2.1 [84]. Moreover, digital coherent receivers can mitigate static and dynamic impairments through DSP algorithms [85]-[86].

The perfect synchronicity of IQ measurements cannot be achieved without the compensation of the (slight) mismatch of the optical path lengths and/or of the possible misalignment of the 90° optical hybrid, which could not provide

a perfect 90° phase rotation of the LO. To compensate for the path length mismatches and so to synchronize the digital signals, algorithms of signal deskew are implemented [87]. The timing mismatch is estimated or measured, but usually it is not correspondent to an integer number of samples. Considering that each sample has a duration T_{ADC}, the time delay $\tau = sT_{ADC} + pT_{ADC}$ is composed of an integer number of samples $s = \lfloor \tau / T_{ADC} \rfloor$, which can be easily employed for the retiming, and a fraction of the time sample pT_{ADC}, for which interpolation is needed in order to be exploited in the deskew algorithms [88]. The orthonormalization algorithms are needed to recover the orthogonality between I and Q signal components in case of an imperfect 90° optical hybrid. Considering a phase between the components $\gamma = \pi/2 - 2\vartheta$, the algorithms consider the correlation matrix R between the received signals $r_I = t_I \cos(\vartheta) + t_Q \sin(\vartheta)$ and $r_Q = t_Q \cos(\vartheta) + t_I \sin(\vartheta)$ (t_I and t_Q are the I and Q components of the transmitted signal) as

$$R = \begin{bmatrix} 1 & \sin(2\vartheta) \\ \sin(2\vartheta) & 1 \end{bmatrix}. \tag{2.28}$$

In *Gram-Schmidt* algorithm a signal component is kept unchanged, while the other is rotated of 2ϑ to restore the orthonogality, and then they are normalized in power [89]. Another example is the *Löwdin* algorithm, which generates a set of vectors which are the least-mean squared closest to the original ones [90].

Thanks to DSP, some transmission impairments, such as CD and PMD, can be compensated. To recover the accumulated CD, two different approaches can be implemented:

1. by solving the equation modelling CD

$$\frac{\delta A(z,t)}{\delta z} = -j\frac{\delta^2}{A}(z,t)\delta t^2, \tag{2.29}$$

   the phase shift introduced by this linear impairment can be recovered and applied with the opposite sign (see Section 3.5);

2. by realizing Finite Impulse Response (FIR) or Infinite Impulse Response (IIR) filters [91].

In this thesis the first solution is adopted, thanks to its simplicity in the implementation, while the other solution is computationally heavier. A drawback is that it requires a complete knowledge of the propagation length, but for the purposes of the thesis it is not a problem, since the propagation length is under control of the user. Similarly, fiber nonlinear effects can be mitigated by applying a reverse channel model exploiting the same equations describing the nonlinear fiber propagation (see Section 3.2) [92], but its complexity can become significant in presence of a multichannel propagation and so it is out of the scope of this work. For some laboratory measurements, in presence of hundred-km SSMF propagation, the *Volterra equalization algorithm* is used to mitigate nonlinear impairments due to fiber propagation and optical filtering. The output of the Nth order Volterra algorithm with the truncation of the memory length to M_m for each order m ($m \in [1,\ N]$) applied to the kth sample of the discrete input signal x can be expressed as [93]

$$\begin{aligned} y(k) = \sum_{m=1}^{N} \sum_{n_1=0}^{M_m-1} \sum_{n_2=0}^{n_1} \dots \sum_{n_m=0}^{n_{m-1}} w_m\left(n_1, n_2, \dots n_m\right) \cdot \\ \cdot x\left(k-n_1\right) x\left(k-n_2\right) \dots x\left(k-n_m\right), \end{aligned} \tag{2.30}$$

where $w_m\left(n_1, n_2, \dots n_m\right)$ are the weights of the equalizer for the Nth order. The number of samples of the channel impulse response gives the lower bound to the memory length M_m [94]. In this thesis, a 3$^{\text{rd}}$ order Volterra algorithm is employed, so the kth sample of the received signal r is equalized as follows:

$$\begin{aligned} y(k) = \sum_{n_1=0}^{M_1-1} w_1(n_1) \cdot x(k-n_1) + \sum_{n_1=0}^{M_2-1} \sum_{n_2=0}^{n_1} w_2(n_1, n_2) x(k-n_1) x(k-n_2) + \\ + \sum_{n_1=0}^{M_3-1} \sum_{n_2=0}^{n_1} \sum_{n_3=0}^{n_2} w_3(n_1, n_2, n3) \cdot x(k-n_1) x(k-n_2) x(k-n_3). \end{aligned} \tag{2.31}$$

When the algorithm is applied to DMT-modulated optical signals, a proper choice of $w_1(n_1)$, $w_2(n_1, n_2)$, and $w_3(n_1, n_2, n_3)$ for every sample on the coherently received signal helps to compensate for the nonlinear impairments both in channel estimation and in bit-loading phases (see Section 3.1.2.1 for more details), leading the capacity to increase, as presented in Section 4.4.

FIR filters can be employed to recover PMD as well, by reverting the Jones matrix of the channel [95]

$$P = \begin{bmatrix} \cos(\vartheta) & e^{-j\phi}\sin(\vartheta) \\ -e^{-j\phi}\sin(\vartheta) & \cos(\vartheta) \end{bmatrix}, \tag{2.32}$$

where 2ϑ and ϕ are the azimuth and elevation angles to be found [96].

In order to correctly detect the received signal, timing recovery is mandatory [97]. Several algorithms can be implemented, either data-aided [98] or non-data-aided [99]. In this thesis, a non-data-aided algorithm is implemented, by exploiting particular symbols, as it is described more in depth in Section 3.5. Non-data-aided algorithms are based on the interpolation of the received signal $y(m_k, \mu_k)$ and the maximization of its squared modulus $|y(m_k, \mu_k)|^2$. The differentiation of $|y(m_k, \mu_k)|^2$ provides the error signal $e(m_k)$, which approaches to zero when the signal is synchronized. The error function is then used to update the estimate of $w_k = T_{symb}/T_{ADC}$ as

$$w_{k+1} = w_k + \sum_{i=0}^{N-1} c_i e(m_{k-i}). \tag{2.33}$$

c_i are the coefficients of the FIR filter of length N by which the error signal is filtered.

Frequency estimation is another feature provided by digital COH-RX. Generally the sample clock at the Transmitter (TX) and the one at the Receiver (RX) are not synchronous, since they are locally generated, so a frequency shift between them arises, and this induces a delay which increases in time. Considering the kth sample of the RX input signal

$$x_{in}[k] = x_{sym} \exp\left[j\left(\phi[k] + 2\pi\Delta f_{TX-RX} k T_{sym}\right)\right], \tag{2.34}$$

the value of Δf_{TX-RX} has to be estimated. Δf_{TX-RX} induces a rotation in the FFT samples, which has to be recovered. Several algorithms can be applied to face this problem, depending on the modulation format. For QPSK format, the probability density function of the cumulated phase is used to estimate Δf with the maximum likelihood technique [100]; otherwise these operations can be reverted and the frequency offset is estimated by iterations [101]. Another method, which can be applied for M-QAM modulation formats, is to detect the peak of $x_{in}^4[k]$ [102]. In DMT modulation, the timing error due to the different sampling e_m^n of the nth sample of the mth symbol is averaged on the symbol length

$$\hat{e}_m^n = \frac{1}{2N} \sum_{n=0}^{2N-1} e_m^n \tag{2.35}$$

and it can be exploited to correctly rotate the FFT symbols. This method has the disadvantage of considering the same delay for every sample of the symbol, and this introduces intercarrier interference. It can be corrected by interpolating the signal and filtering it with a FIR filter, as previously introduced [97].

The process of phase estimation is similar to the one applied for frequency estimation. In QPSK the symbols are elevated to the 4^{th} power ($s(k) = r(k)^4$) to eliminate the phase modulation. Then, $s(k)$ is averaged on a given number of symbols, depending on the noise level and its type (*e.g.*, ASE or phase noise) [103],

$$\sum_{i=k-N}^{k+N} a_i s_i. \tag{2.36}$$

a_i is a windowing function. The argument provides the value of $\vartheta(k)$, *i.e.*, the phase correction factor of the kth symbol [104].

In this thesis a simplified approach to COH-D has been implemented. The simulated COH-RX is supposed to be almost ideal, *i.e.*, it is not impaired by skew and loss of orthogonality between signal components, for instance, but the photodiodes introduce noise. After the recovery of I and Q components, the

CD is compensated, the square moduli of the two components are performed and then summed to recover the originally transmitted intensity signal. This technique allows to obviate to the use of phase and frequency recovery and lowers the complexity of the DSP at the receiver side. A weakness of this approach is that the advantages in terms of BER as a function of Signal to Noise Ratio (SNR) typical of COH-D are cancelled by this operation [105].

Chapter 3

Simulation tool for Metropolitan Area Networks emulation

In this chapter the MATLAB® simulator which has been developed for the system evaluations is presented. Some of the main blocks introduced in Chapter 2 are analyzed in terms of mathematical functions and algorithms needed to emulate their behaviour. The electro-optic bandwidth, the chirp parameters, and the lineshape of the VCSEL are the main investigated characteristics of the directly-modulated optical source. The bit- and power-loading algorithms optimize the spectral occupancy of the modulating DMT electrical signal. In the simulations presented in this thesis, the signal is supposed to propagate through Standard Single-Mode Fiber (SSMF) spans; the main nonlinear impairments due to the *Kerr effect* are described in terms of theoretic phase distortion and power affection. Furthermore, the algorithms to emulate such impairments are briefly described. The formula to emulate the Optical Signal-to-Noise Ratio (OSNR) introduced by the presence of in-line Erbium-Doped Fiber Amplifiers (EDFAs) is shown for both single and multi-span scenarios. The Transfer Functions (TFs) of the HL4 and HL3 nodes are shown in Figures 3.10 and 3.11. A particular focus is put on the Wavelength Selective Switch (WSS) and its application to the 25-GHz spacing grid required in the

HL3 nodes. At last, the CD compensation in COH-D and the algorithms to correctly recover the signal are presented.

3.1 VCSEL-based multichannel transmitter

In this section, some main points regarding the modelling of the transmitter are highlighted. During this section, a single source composing the S-BVT described in Chapter 2 will be discussed; anyway the simulations can be easily extended to the entire structure, provided the knowledge of the desired channel spacing to generate.

3.1.1 Directly-modulated VCSEL

As explained in Section 2.1.1, VCSELs are the sources mainly employed for this thesis, so the focus of this description will be put on this architecture of lasers. However, the simulator is not constrained to this choice, and, by properly setting the parameters, it can emulate several different sources. This section will describe the modelling of VCSELs in terms of their electro-optical bandwidth, chirp, and lineshape.

3.1.1.1 The electro-optical bandwidth of a VCSEL source

The transfer function $H_{VCSEL}(f)$ depends on both intrinsic and parasitic effects of the VCSEL [107]. Thanks to the cascaded two-port model [106] (see Figure 3.1), these two contributions can be discussed as two separate transfer functions H_{int} and H_p respectively:

$$H_{VCSEL}(f) = H_{int}(f) \cdot H_p(f). \tag{3.1}$$

The intrinsic modulation response, due to the lasering part itself (active layer and cavity),

$$H_{int} = \frac{f_r^2}{f_r^2 - f^2 + j\frac{\gamma}{2\pi}f}, \tag{3.2}$$

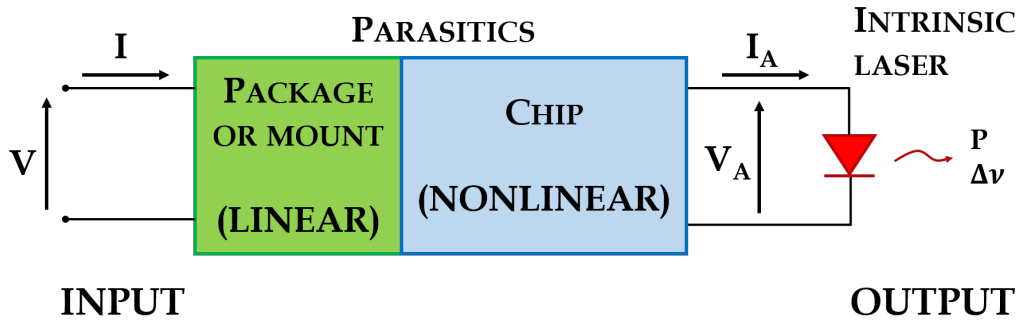

Figure 3.1: Schematic of the two-port model for the characterization of semiconductor lasers, similar to the one shown in [106]

is a two-pole transfer function (-40 dB/dec in the Bode diagram) depending on a relaxation frequency f_r and on the intrinsic damping factor γ.

The parasitic modulation response

$$H_p(f) = \frac{1}{1 + j\frac{f}{f_p}} \tag{3.3}$$

has one single pole at the parasitic cut-off frequency f_p. It arises from parasitic resistances and capacities due to the package, and to the semiconductor chip [108].

So, the overall transfer function

$$H_{VCSEL} = \frac{f_r^2}{f_r^2 - f^2 + j\frac{\gamma}{2\pi}f} \cdot \frac{1}{1 + j\frac{f}{f_p}} \tag{3.4}$$

depends on three parameters: f_r, γ, and f_p. They are dependent on some physical parameters of the device (*e.g.*, the photon density, the photon lifetime, and the threshold current, just to cite a few). For a single-mode VCSEL, the relaxation frequency f_r

$$f_r = \sqrt{\frac{v_g a N_p}{\tau_p}} = \sqrt{\frac{v_g a \nu_i}{qV}} \cdot \sqrt{I_{bias} - I_{th}} \tag{3.5}$$

depends on the group velocity v_g, the differential gain a, the photon density N_p and lifetime τ_p, the mode volume V, the bias current I_{bias}, and the threshold

current I_{th}. In order to increase the modulation bandwidth, f_R needs to be increased by operating on the physical parameters of the VCSEL to enhance the differential gain and lower the photon lifetime [109].

The damping factor γ has a quadratic dependence on f_R:

$$\gamma = K \cdot f_r^2 + \gamma_0. \tag{3.6}$$

γ_0 is the damping offset, which can be neglected for long-wavelength short-cavity VCSELs, as the one taken into account in this thesis. The K-factor K depends on τ_p and a as follows:

$$K = 4\pi^2 \left(\tau_p + \frac{\varepsilon\chi}{v_g a} \right). \tag{3.7}$$

The transport factor χ depends on the charge carrier escape and capture rates in the quantum wells, while ε accounts for the gain compression at higher injection levels. The reduction of τ_p and the increase of a, suggested as a way to increase the modulation bandwidth, lowers the value of K: this optimizes both f_R and γ, maximizing the intrinsic bandwidth [110].

However, the most feasible approach (also used for this thesis) is to evaluate the impact of this filtering on the SNR coming from a laboratory measurement and comparing it with the corresponding one obtained with the analogous simulation to find the best fitting. In Figure 3.2 an example of SNR fitting, along with the intrinsic, parasitic and overall VCSEL TFs, is shown for 16-GHz bandwidth.

3.1.1.2 Chirp parameters assessment for directly-modulated lasers

The chirp of an optical source is the variation in time of the instantaneous frequency of the generated optical pulse. In directly intensity-modulated semiconductor sources the modulation induces a variation in the carrier density, leading to a modification of the refractive index, which causes the frequency chirp. In Directly Modulated Lasers (DMLs), the time dependence of the

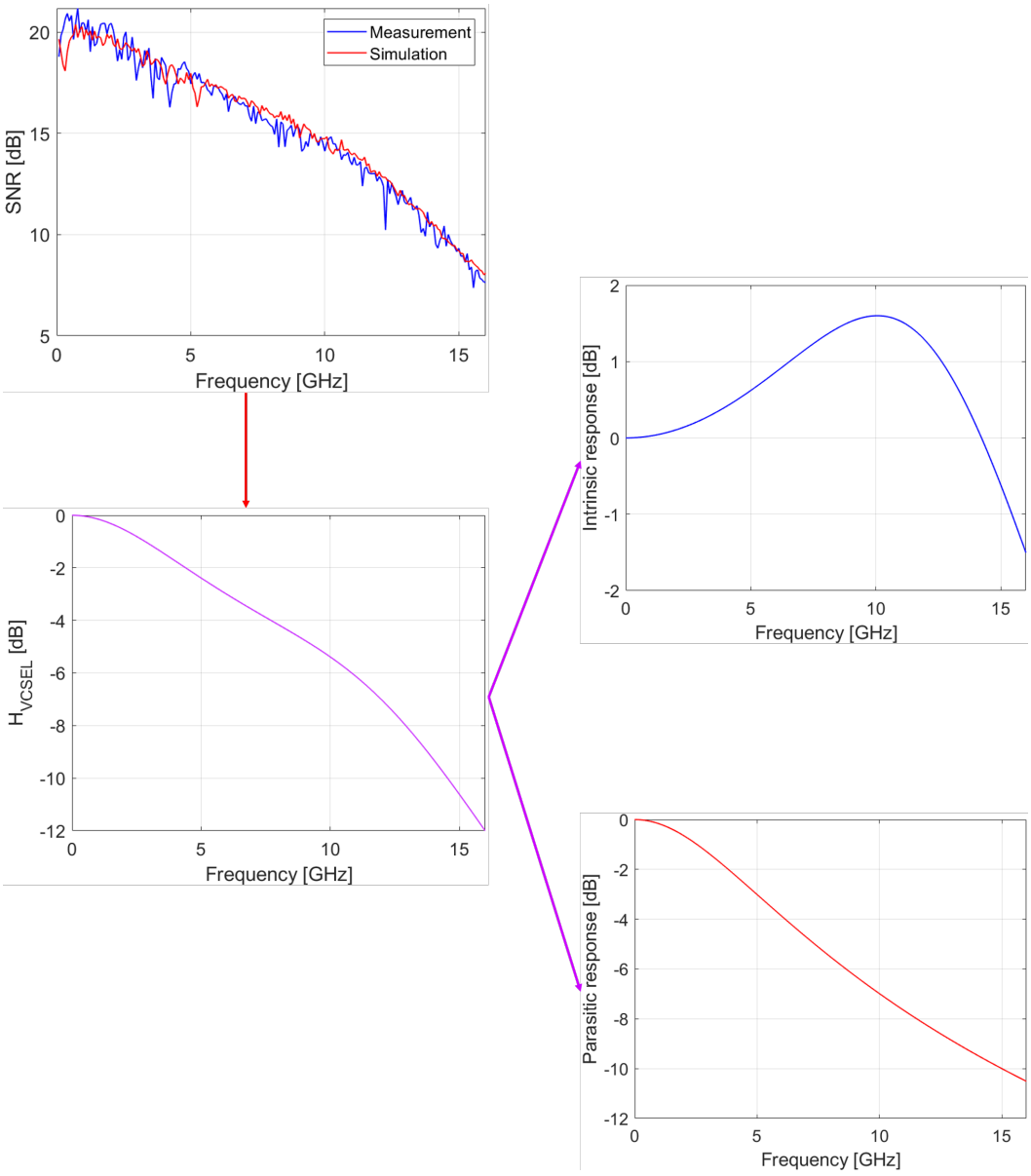

Figure 3.2: Example of fitting of the experimentally measured SNR (blue line of the upper left figure) with the one obtained by simulations in the same conditions to assess the best values of f_R, γ, and f_p. In the lower left part of the figure, the estimated VCSEL TF, which is composed of the intrinsic response (blue line in the right part of the figure) and the parasitic response (red line).

instantaneous frequency introduces a frequency modulation, which can be described from the relation between the instantaneous frequency deviation $\Delta\nu(t)$ and the optical modulated power $P(t)$ [111]:

$$\Delta\nu(t) = \frac{\alpha}{4\pi}\left[\frac{1}{P(t)}\frac{\delta P(t)}{\delta t} + \kappa P(t)\right]. \tag{3.8}$$

The *linewidth enhancement factor* α, also known as *Henry factor*, relates phase changes to variations of the gain ($\Delta\phi = \alpha/2 \cdot \Delta g$). The name *linewidth enhancement factor* arises from the fact that Henry demonstrated that the coupling of phase and amplitude fluctuations enhances the linewidth of the laser by a factor $1 + \alpha^2$ [112]. The first term of Eq. 3.8, namely the *transient* component of $\Delta\nu$, predominantly depends on α. The laser-specific adiabatic constant κ is a function of the gain compression parameter, of the photon lifetime, and of the confinement factor. The second term of Eq. 3.8 depends on κ, and it constitutes the *adiabatic* contribution of $\Delta\nu(t)$ [113].

A way to evaluate the chirp parameters is to exploit the CD introduced in fiber propagation. In fact, due to CD, the spectral components of the modulated optical signal accumulate a different phase during propagation. When the signal is received with coherent detection, offline DSP can completely compensate for CD. Instead, thanks to the distortion introduced in the directly-received electrical spectrum, the employed source can be evaluated in terms of its chirp parameters. The DSB spectrum achieved by direct modulation of the laser leads to destructive beating at specific frequencies after propagation and direct detection. The so generated frequency-selective channel produces fading dips, the position in frequency depending on the accumulated CD. On the top of it, laser chirp parameters modify the intensity and the position in frequency of the fading dips as well. This suggests a method to evaluate the chirp properties of an optical source: fitting the uncompensated transfer function of the channel, which for a DML can be expressed as [114]

$$H(\omega) = \left|\cos\vartheta - \sin\vartheta \cdot \alpha\left(1 - j\frac{\omega_c}{\omega}\right)\right|, \tag{3.9}$$

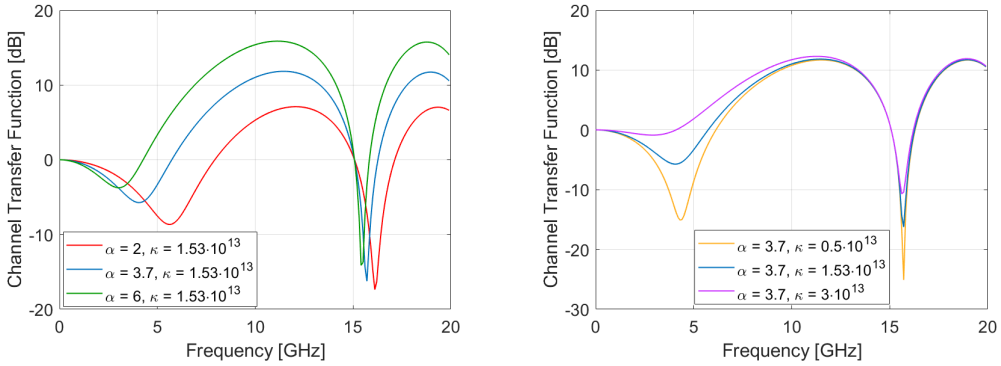

(a) Varying α **(b)** Varying κ

Figure 3.3: Dependence of the channel TF for a DML laser on (a) α and (b) κ.

where

$$\vartheta = \frac{LD\lambda_0^2\omega^2}{4\pi c}, \ \omega_c = \kappa P_0, \tag{3.10}$$

L is the fiber length, D is the dispersion coefficient, λ_0 is the nominal wavelength of the CW source, c is the speed of light, and P_0 is the mean optical power. The height of the secondary lobes and the position in frequency of the dips depend on an interplay of α and D (see Figure 3.3(a)), while the width of the dips mainly depends on ω_c, and as a consequence on κ (see Figure 3.3(b)) [115].

The interplay of chirp parameters with optical filtering is studied in depth in Section 4.2.

3.1.1.3 VCSEL lineshape

The frequency noise of a semiconductor laser, which is strictly related to the laser linewidth when it is spectrally flat [116], cannot be approximated as a white noise, since it contains 1/f components dominant at low frequencies; moreover semiconductor sources, such as VCSELs, are affected by carrier-induced noise as well [117]. The instantaneous frequency oscillations arising from the frequency noise can be modelled through their single-sided power

spectral density as follows [118]:

$$S_\nu(f) = \frac{10^9 \Delta\nu_{(1/f)}}{\pi f} + \frac{\Delta\nu_{int}}{\pi(1+\alpha^2)} \left(1 + \alpha^2 \frac{f_R^4}{(f_R^2 - f^2)^2 + \left(\frac{K f_R^2}{2\pi} f\right)^2} \right). \quad (3.11)$$

$\Delta\nu_{(1/f)}$ is the level of 1/f noise measured at 1 GHz, while $\Delta\nu_{int}$ represents the level of intrinsic low-frequency noise. The K-factor is a bias independent parameter indicating the relation between damping rate and relaxation frequency. f_R is the resonance frequency, while α is a measure of the magnitude of the carrier-induced noise. The first two parameters model the 1/f low-frequency components, while the other three emulate the carrier-induced noise.

The work discussed in [119] determines the linewidth of a laser starting from its power spectral density (which is not needed to be white), with a good confidence in the results. Before providing the expression of the linewidth, they separate the evolution in frequency of the power spectral density in two portions: the region in which the modulation index β, defined as the ratio between the frequency deviation and the modulation frequency, is higher than 1, and the other section, where $\beta < 1$. The first region, which is the central one contributing to the linewidth, has a Gaussian shape, while the latter, for which the modulation is too fast to contribute to the linewidth, impacts on the tails of the lineshape. Following from these considerations, the expression they provide for the Full Width Half Maximum (FWHM) of a laser source can be obtained knowing the area A of the first region

$$FWHM = \sqrt{8 \cdot \ln 2 \cdot A}. \quad (3.12)$$

The lineshape of VCSEL is approximated in the simulator with the so-called *Voigt* distribution (see Figure 3.4), which combines the Gaussian profile for low-frequency components and the Lorentian lineshape for high frequencies [120].

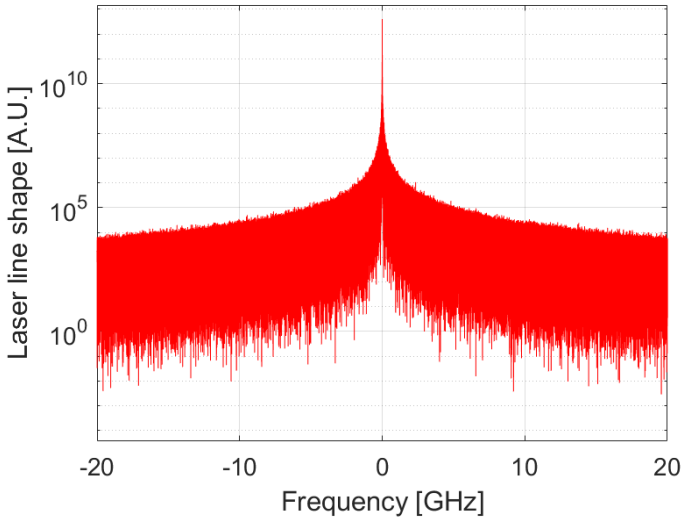

Figure 3.4: Voigt laser line shape of the simulated VCSEL.

A good approximation is [121]

$$f(\nu) = V_0 \Bigg\{ \left(1 - \frac{\gamma_L}{\gamma_V}\right) \exp\left[-2.772 \left(\frac{\nu - \nu_0}{\gamma_V}\right)^2\right] + \\ + \frac{\gamma_L}{\gamma_V} \frac{1}{1 + 4\left[\left(\nu - \nu_0\right)/\gamma_V\right]^2} \Bigg\} : \tag{3.13}$$

V_0 is the (Voigt profile) amplitude, γ_L and γ_V are the Lorentian and Voigt linewidths respectively. [120] presents an expression of the Voigt distribution as the sum of a Gaussian and a Lorentian profile which can be employed as well to match the results of the linewidth characterization of the VCSEL source:

$$f(\nu) = \frac{A}{1 + \left[\left(\nu - \nu_0\right)/\gamma\right]^2} + B \exp\left[-2\left(\frac{\nu - \nu_0}{\beta}\right)^2\right] + N(\nu), \tag{3.14}$$

where the parameters A, B, γ, and β are used to correctly fit the measured lineshape, while $N(\nu)$ is the detection noise.

3.1.2 DMT modulation for high-capacity applications

The VCSEL is directly modulated with an electrical DMT signal generated as described in Section 2.1.2. After being parallelized, the input Pseudo-

Random Binary Sequence (PRBS) symbols are mapped into the wanted modulation formats, either the same for all the subcarriers or different depending on whether the channel estimation has still to be performed or not (as it will be more diffusely shown in the following paragraph). In order to synchronize the signal at the receiver side and to estimate the channel, some training symbols are added. A CP is then appended by replicating a final portion of the symbol and copying it at the beginning of the same symbol. The length of the CP impacts on the overall system performance: its effect is to limit inter-symbol and inter-carrier interference, but on the other way round it reduces the useful data rate [122]. A trade-off between these two instances needs to be found. The DMT signal is then serialized and a symmetrical clipping is applied. Clipping is needed because in DMT signal generation high power peaks may occur or, in other words, by defining the Peak-to-Average Power Ratio (PAPR) as the ratio between the maximum signal power P_{max} and the average power P_{mean}

$$PAPR = \frac{P_{MAX}}{P_{mean}}, \tag{3.15}$$

the DMT signal before clipping $x_d(t)$ has a high PAPR. The clipping level C_L (in dB) is computed as

$$C_L = 10 \cdot \log_{10}\left(\frac{A_{MAX}^2}{\overline{x_d}^2}\right), \tag{3.16}$$

where A_{MAX} is the maximum allowed signal amplitude, and $\overline{x_d}^2$ is its average power [123]. Clipping adds a clipping noise which furthermore degrades the DMT signal, so C_L has to be optimized to limit the effect of the clipping noise on the system performance as much as possible [124]. For a systematic discussion about the performance of symmetrically clipped DMT signals and the impact of clipping noise on the SNR of the system see [125].

3.1.2.1 Bit-loading and power-loading algorithms

Whatever optical communication system has to be planned, it is important to maximize the transmitted capacity. An advantage of DMT modulation is

its capability to adapt to the impairments introduced by spectrally shaped channels in order to optimize the system transmission bandwidth. This is possible by exploiting bit-loading and power-loading algorithms, which adjust the modulation order and the power level per subcarrier observing the corresponding SNR. Subcarriers with a better SNR are assigned a higher number of bits per symbol with respect to subcarriers with a lower SNR. Higher modulation formats are less robust to noise: having fixed the signal energy, the symbols in the space of the signals are closer when the modulation format is higher, since the number of symbols is higher as well. The policy according to which this assignment is performed follows two different criteria:

- *rate-adaptive* algorithms: they maximize the bit rate keeping fixed a target BER and the constraint on power;
- *margin-adaptive* algorithms: they minimize the BER for a given bit rate.

Rate-adaptive algorithms are widespread in communication networks because they guarantee data transmission even in poor channel conditions (*i.e.*, characterized by low values of SNR). They aim at finding the best power combination for the subcarriers which maximizes the aggregate throughput over the used signal bandwidth [126].

In order to optimize the transported capacity the MATLAB® simulator implemented for this thesis exploits the Chow's bit-loading and power-loading algorithm [127]. This algorithm approaches the solution of the *water-filling* problem for bit-rate maximization:

$$P_n + \frac{\Gamma}{g_n} = constant, \tag{3.17}$$

where P_n is the power of the subcarrier n, g_n is the inverse of the noise introduced by the system at the nth subcarrier or, in other words, it is the SNR of the nth subcarrier when $P_n = 1$ ($SNR_n = P_n \cdot g_n$), Γ is the SNR gap, *i.e.*, the difference between the SNR required to achieve the maximum

capacity (based on Shannon theory) and the SNR required to achieve this same capacity at a predefined BER. Γ depends on the chosen modulation format and the wanted Symbol Error Rate (SER)[1]. For a M-QAM, Γ can be computed as follows [129]:

$$\Gamma = \frac{1}{3} \cdot \left[Q^{-1} \left(\frac{SER}{4} \right) \right]^2, \tag{3.18}$$

where Q^{-1} indicates the inverse Q-function.

Eq. (3.17) indicates that, in order to maximize the transported capacity, $P_n + \frac{\Gamma}{g_n}$ has to be constant: power distribution can be optimized by properly choosing this constant (since the system is power-limited), depending on the level of noise, and on the accepted BER.

The solution to *water-filling* problem leads to the optimal bit-loading maximization; however it is computationally heavy and, if implemented, it would require an infinite granularity from the constellation point of view, *i.e.*, it would require modulation formats with non-integer number of bits per symbol. Chow's algorithm [127] leads to a maximization of the transmitted capacity by fragmenting the problem in three steps:

1. it finds the optimal margin γ_{margin}, the additional amount of noise a system can tolerate to achieve a given capacity with a desired BER;

2. it converges to a sub-optimal solution;

3. for power-constrained systems, it adjusts the energy distribution subcarrier per subcarrier.

More in detail, the steps to follow to reach the suboptimal solution of bit-loading and power-loading problems are summarized in the flowchart of Figure 3.5 [127] and here briefly explained.

1. The SNR of the nth subcarrier, SNR_n, is measured. In order to evaluate the SNR, a DMT probe signal is sent. This signal is composed of

[1]With Gray mapping, $BER \approx SER/b_s$, where b_s is the number of bits per symbol [128]

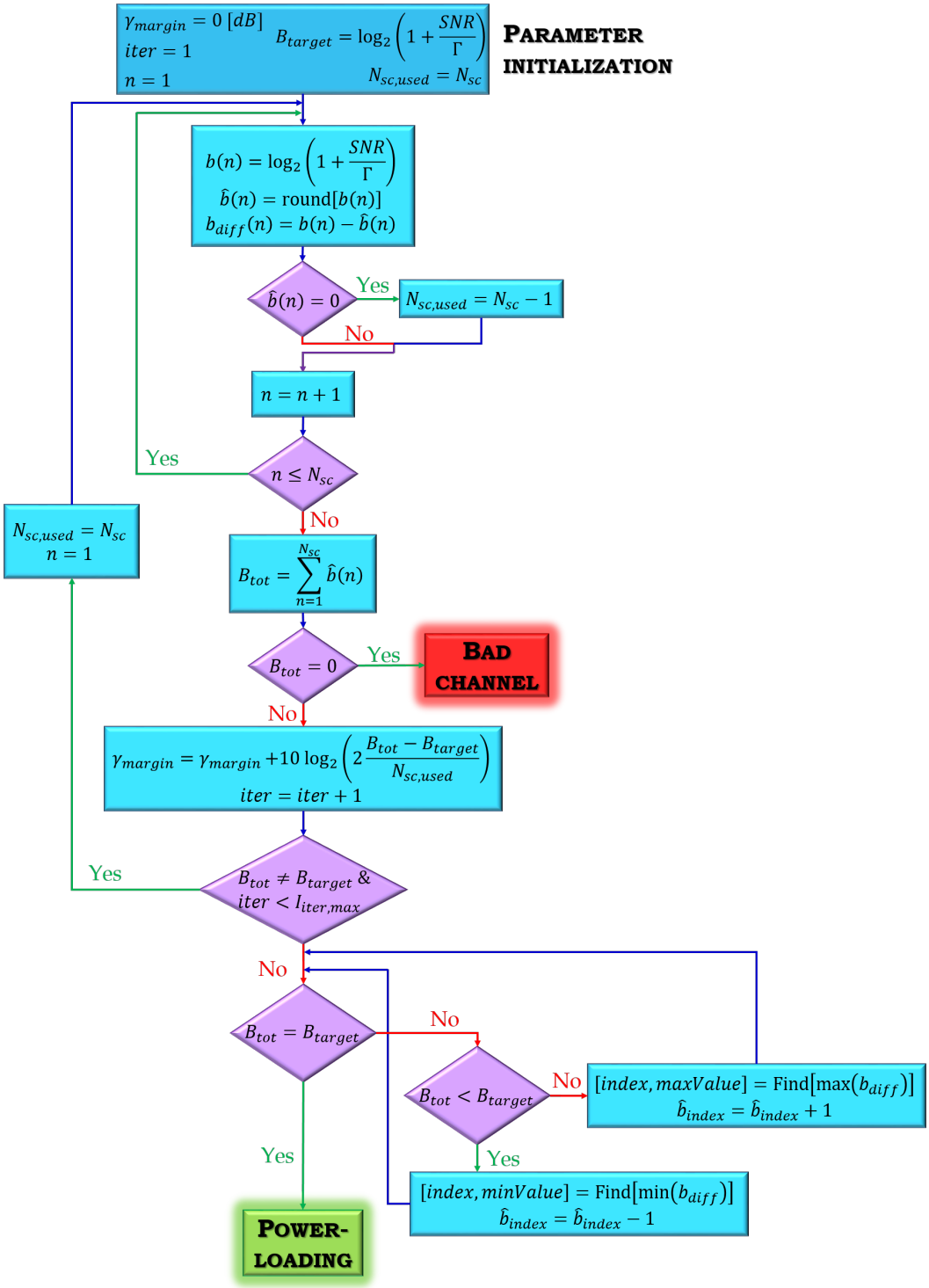

Figure 3.5: Flowchart of the Chow's bit- and power-loading algorithm [127], inspired by the one shown in [130].

equally-spaced subcarriers along the bandwidth of interest and modulated with the same modulation format, *e.g.*, Quadrature Phase Shift Keying (QPSK).

2. The algorithm parameters are initialized: the system performance margin $\gamma_{margin} = 0\ (dB)$, the number of iteration $iter = 0$, and the number of useful subcarriers to the total number of subcarriers ($N_{sc} = N_{TOT}$). In order to reduce the time consumption of the algorithm, a maximum number of iterations $I_{iter,max}$ has to be set.

3. For each subcarrier, the algorithm computes the number of bits $b(n)$, its approximation to the closest integer number $\hat{b}(n)$, the difference between these two parameters $b_{diff}(n)$, and the number of useful subcarriers:

$$b(n) = \log_2\left(1 + \frac{SNR_n}{\Gamma + \gamma_{margin}(linear)}\right), \tag{3.19}$$

$$\hat{b}(n) = round\left[b(n)\right], \tag{3.20}$$

$$b_{diff}(n) = b(n) - \hat{b}(n). \tag{3.21}$$

If $\hat{b}(n) = 0$, the nth subcarrier is useless, so the number of useful subcarriers is reduced by 1: $N_{sc} = N_{sc} - 1$.

4. The algorithm calculates the overall number of bits per symbol as $b_{total} = \sum_{n=1}^{N_{TOT}} \hat{b}(n)$. If $b_{total} = 0$, the channel is deemed bad, and so it is unusable.

5. The system margin γ_{margin} is updated depending on the wanted number of bits per DMT symbol B_{target}, the total number of bits per symbol B_{total}, and the number of useful subcarriers N_{sc}:

$$\gamma_{margin}(dB) = \gamma_{margin}(dB) + 10 \cdot \log_{10}\left(2^{\frac{B_{total} - B_{target}}{N_{sc}}}\right). \tag{3.22}$$

6. If $B_{target} = B_{total}$, the subcarrier power has to be adjusted (in case of power-limited systems).

7. If $iter < iter_{max}$ and $B_{target} \neq B_{total}$, the iteration number has to be incremented ($iter = iter + 1$), the number of useful subcarriers is again initialized to the total number of subcarriers ($N_{sc} = N_{TOT}$), and the algorithm is repeated from point 3 until $B_{target} = B_{total}$;

8. If $iter = I_{iter,max}$ and $B_{target} \neq B_{total}$ two different scenarios can arise:

   - if $B_{target} < B_{total}$, one bit has to be added to the $b(n)$ which has the largest $b_{diff}(n)$ and repeat until $B_{target} = B_{total}$;
   - if $B_{target} > B_{total}$, one bit has to be subtracted to the $b(n)$ which has the smallest $b_{diff}(n)$ and until $B_{target} = B_{total}$.

Since the training of step 1 has to be performed whenever the system conditions change, the algorithm has to be repeated when other perturbations in the systems occur in the meantime. The aforementioned passages fulfill the request in bit-loading, while the last step is to adapt the power of the individual subcarriers. Each subcarrier has been characterized by $\hat{b}(n)$ given the measured SNR_n, so the minimum SNR, SNR_{needed}, necessary to support the modulation format with $\hat{b}(n)$ bits per symbol with a target BER can be evaluated. Considering that before power-loading each subcarrier is characterized by the same power level P_{sub}, the power of the nth subcarrier after power-loading, P_n, can be computed as follows:

$$P_n = p(n) \cdot P_{sub}, \tag{3.23}$$

where

$$p(n) = 10^{\frac{SNR_{needed} - SNR_n}{10}} \tag{3.24}$$

is a coefficient which guarantees that every subcarrier with the same modulation format has the same SNR performance. From Eq. 3.24 it emerges that, if the measured SNR SNR_n is $SNR_n > SNR_{needed}$, the corresponding subcarrier power level is decreased by the quantity p_n to have an SNR after power loading $\widehat{SNR}_n \approx SNR_{needed}$. Viceversa, for $SNR_n < SNR_{needed}$, the power level is

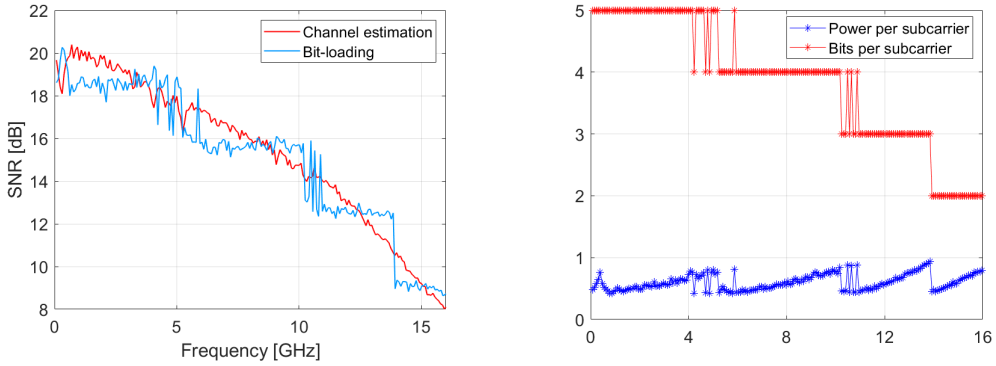

(a) SNR

(b) Bits per symbol and power per subcarrier

Figure 3.6: Effect of the application of Chow's algorithm on: (a) the SNR, (b) the achievable modulation format and the power-loading per subcarrier.

increased by p_n to reach $\widehat{SNR}_n \approx SNR_{needed}$. This leads to have a step-like SNR distribution after power-loading.

With a power constraint P_{TOT} to meet, it is mandatory that

$$\sum_{n=1}^{N_{sc}} P_n = P_{TOT}. \tag{3.25}$$

Figure 3.6(a) shows an example of comparison between the SNR measured for the channel estimation of a transmission system and the SNR after the application of Chow's algorithm for a target BER of $3.8{\cdot}10^{-3}$; Figure 3.6(b) depicts the correspondent bits per symbol and power-loading for each subcarrier. The SNR after the application of Chow's algorithm clearly presents four levels, corresponding to the values of SNR_{needed} necessary to achieve the modulation formats in Figure 3.6(b) and demonstrates a step-like distribution.

3.2 Standard Single-Mode Fiber emulation

In Section 2.3 the multicore fiber has been introduced as a valid solution to improve the transmitted capacity, but in the following paragraph and in the

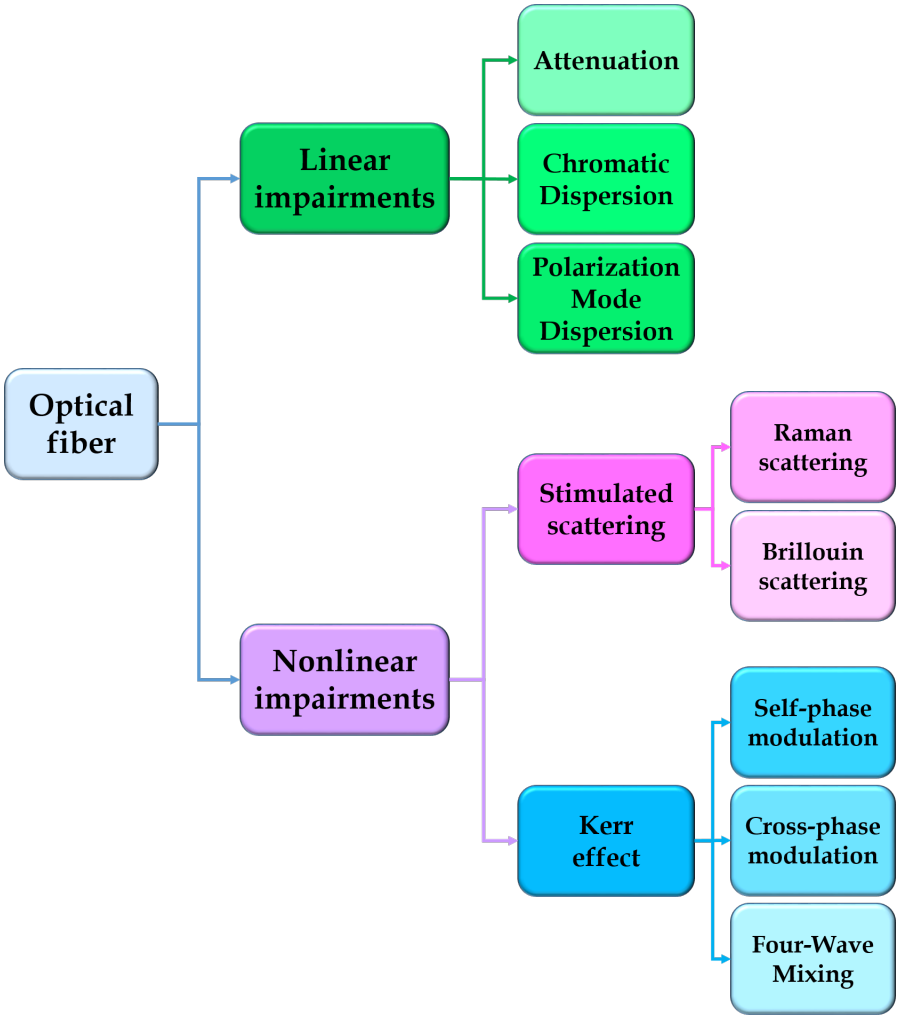

Figure 3.7: Schematic of the main optical fiber impairments.

simulation results presented in Chapter 4 the transmission medium is a SSMF. In the developed MATLAB® simulator it is possible to emulate the behaviour of the optical fiber in two different regimes, summarized in Figure 3.7:

- linear regime;
- nonlinear regime.

Linear regime takes into account only the linear effects introduced by the fiber, in particular fiber attenuation, CD, and PMD. Fiber nonlinear effects can be classified in two categories, depending on the effects they give rise to [131]:

- stimulated scattering (Raman and Brillouin), which causes loss (or gain) to be intensity-dependent;
- intensity-dependent phase shift of the optical field induced by nonlinear index of refraction $n(t)$.

In this thesis, the stimulated scattering is neglected in the simulation of the optical fiber. The focus is put on the phase-shift due to nonlinear $n(t)$. In order to introduce these impairments, the *Kerr effect* is needed to be briefly presented. In a transparent isotropic medium such as the optical fiber, this effect induces a variation in the refractive index $n(t)$ proportional to the intensity $I_{opt}(t) = P_{opt}(t)/A_{eff}$ of the signal propagating in the material:

$$\Delta n(t) = n_2 \cdot I_{opt}(t) = n_2 \cdot \frac{P_{opt}(t)}{A_{eff}}, \tag{3.26}$$

where $P_{opt}(t)$ is the time-dependent power of the signal, A_{eff} is the effective mode area, and n_2 is the *nonlinear index*, a proportionality factor depending on the material and on the wavelength λ of the signal. It can be related to the third-order susceptibility of the material $\chi^{(3)} = \chi_R^{(3)} + j\chi_R^{(3)}$ as [132]

$$n_2 = \frac{3}{4\varepsilon_0 c\,(n_0^2 + k_0^2)} \left[\chi_R^{(3)} + \frac{k_0}{n_0} \cdot \chi_I^{(3)}\right], \tag{3.27}$$

where $k_0 = \alpha_0 \cdot \lambda / 4\pi$, α_0 is the linear absorption coefficient, $\varepsilon_0 = 8.85 \cdot 10^{-12}$ F/m is the electric permittivity of free space, and n_0 is the linear refractive index of the material. The third-order nonlinearities can be experimentally computed with the *z-scan measurements*: a sample of the material to evaluate is moved through the focus of a laser beam, and, depending on the position of the sample, and so on the intensity of the signal collected at a detector, the nonlinear index can be measured [133], [134]. For silica glass, $n_2 \approx 2.6 \cdot 10^{-20}\text{m}^2/\text{W}$ [135].

Due to Kerr effect, the refractive index $n(t)$ can be expressed as the sum of the linear component n_0 and the nonlinear, time-dependent component $\Delta n(t)$

$$n(t) = n_0 + \Delta n(t) = n_0 + n_2 \cdot I_{opt}(t). \tag{3.28}$$

The Kerr effect induces several nonlinear effects. In this thesis Self-Phase Modulation (SPM), Cross-Phase Modulation (XPM), and Four-Wave Mixing (FWM) are taken into account. SPM causes an optical signal to encounter a phase delay depending on its intensity [136]. For a given fiber mode, the phase change due to SPM can be described as

$$\phi_{SPM}(t) = \frac{2\pi \cdot n_2}{\lambda} \cdot L_{eff} \cdot \frac{P_{opt}(t)}{A_{eff}} = \frac{2\pi \cdot n_2}{\lambda} \cdot L_{eff} \cdot I_{opt}(t), \tag{3.29}$$

where $L_{eff} = (1 - e^{-\alpha L})/\alpha$ is the effective nonlinear length of the fiber, and $I_{opt}(t)$ is the optical intensity of the signal. Eq. (3.29) shows that the Kerr effect causes a time-dependent phase shift according to the variation in time of the optical intensity $I_{opt}(t)$. By defining the *nonlinear coefficient* as

$$\gamma_{PM} = \frac{2\pi \cdot n_2}{\lambda \cdot A_{eff}}, \tag{3.30}$$

the phase shift due to SPM can be expressed as

$$\phi_{SPM}(t) = \gamma_{PM} \cdot L_{eff} \cdot P(t). \tag{3.31}$$

SPM is a source of chirp of the propagating optical pulse, leading, for $n_2 > 0$, to a spectral broadening if the initial pulse is un-chirped or up-chirped (*i.e.*, the instantaneous frequency increases in time) or to a spectral compression, if the initial pulse is down-chirped. Given the pulse phase $\phi(t) = \phi_0(t) - \phi_{SPM}(t)$ (where $\phi_0(t)$ is the phase variation of the pulse considering the propagation along a medium with linear refractive index n_0) and reminding that the angular frequency $\omega(t)$ is $\omega(t) = 2\pi f(t) = \partial\phi(t)/\partial t$, the frequency shift $f_{SPM}(t)$ due to SPM is

$$\begin{aligned} f_{SPM}(t) &= -\frac{1}{2\pi}\frac{\partial\phi_{SPM}(t)}{\partial t} = -\frac{n_2}{\lambda} \cdot L_{eff} \cdot \frac{\partial I(t)}{\partial t}, \\ f_{SPM}(t) &= -\frac{\gamma_{PM}}{2\pi} \cdot L_{eff} \cdot \frac{\partial P(t)}{\partial t}. \end{aligned} \tag{3.32}$$

For instance, considering a Gaussian pulse with peak intensity I_0, and pulse duration 2τ

$$I_{opt}(t) = I_0 \cdot e^{-\frac{t^2}{\tau^2}}, \tag{3.33}$$

the variation due to SPM $\phi_{SPM}(t)$ of the pulse phase $\phi(t)$ is

$$\phi_{SPM}(t) = \frac{2\pi \cdot n_2}{\lambda} \cdot L_{eff} \cdot I_0(t) \cdot e^{-\frac{t^2}{\tau^2}} \tag{3.34}$$

and the corresponding variation of $f(t)$ due to SPM is

$$f_{SPM}(t) = \frac{2n_2}{\lambda} \cdot I_0 \cdot L_{eff} \cdot \frac{t}{\tau^2} e^{-\frac{t^2}{\tau^2}}. \tag{3.35}$$

Due to XPM, given two signals propagating along the fiber at different wavelengths, the intensity of one signal introduces a nonlinear phase change on the other signal. The phase shift $\phi^{(b)}_{XPM}(t)$ of a signal b depends on the intensity of the signal a (and viceversa) as

$$\Delta n^{(b)} = 2p \cdot n_2 \cdot I^{(a)}_{opt}(t), \tag{3.36}$$

so

$$\phi^{(b)}_{XPM}(t) = 2p \cdot \gamma_{PM} \cdot L_{eff} \cdot P^{(a)}_{opt}(t). \tag{3.37}$$

$1/3 < p < 1$ is a parameter indicating the polarization mismatch between the two signals: if the SOPs of the two signals are orthogonal, $p = 1/3$, while $p = 1$ if the SOPs are parallel. XPM leads to different frequency shifts of the two signals depending on the powers $P^{(a)}_{opt}(t)$ and $P^{(b)}_{opt}(t)$ carried by the signals

$$f^{(b)}_{XPM}(t) = 2p \cdot \frac{\gamma_{PM}}{2\pi} \cdot L_{eff} \cdot \frac{\partial P^{(a)}_{opt}(t)}{\partial t}. \tag{3.38}$$

The impact of SPM and XPM on the frequency shift is then the sum of the two contributions:

$$\phi^{(b)}_{PM}(t) = \phi^{(b)}_{SPM}(t) + \phi^{(b)}_{XPM}(t) = \gamma_{PM} \cdot L_{eff} \cdot \left[P^{(b)}_{opt}(t) + 2p \cdot P^{(a)}_{opt}(t) \right], \tag{3.39}$$

so it is easy to infer that the effect of the two nonlinearities on the frequency shift is the sum of the two contributions f_{SPM} and f_{XPM} [137].

As for XPM, FWM arises in presence of two or more signals at different wavelengths propagating in fiber. Given two wavelengths at frequencies f_1 and f_2 their beating modulates the fiber refractive index through Kerr effect at a

frequency $f_{mod} = f_1 - f_2$ (for $f_1 > f_2$). This phenomenon generates two other frequency components

$$\begin{aligned} f_3 &= 2f_1 - f_2 \\ f_4 &= 2f_2 - f_1; \end{aligned} \tag{3.40}$$

if a wave at f_3 or f_4 preexists, then it is amplified through *parametric amplification* which amplifies a signal using optical nonlinearities such as χ^3 and a signal employed as a pump [138]. When three waves at frequencies f_i, f_j, and f_k interact, new waves are generated at frequencies

$$f_{ijk} = f_i + f_j - f_k. \tag{3.41}$$

There are 27 possible combinations of the three frequencies, but at most only 9 of them are new frequencies. In fact, if $f_k = f_i$ the resulting frequency is f_j, which is not a new frequency component (and viceversa if $f_k = f_j$), *i.e.*, they are *degenerate* frequency components. Moreover, by changing place to the first two frequencies, no new frequency is generated: for instance, if $i = 1$, $j = 3$, and $k = 2$, $f_1 + f_3 - f_2 = f_3 + f_1 - f_2$ [139]. The case $i = j$ is the same as Eq. (3.40). 6 of the 9 possible different frequencies arise from the cases $i = j \neq k$, and the other 3, for $i \neq j \neq k$ are the components at frequencies $f_i + f_j - f_k$, $f_i + f_k - f_j$, and $f_j + f_k - f_i$.

FWM is a phase-sensitive component, because the interaction among wavelengths (*i.e.*, WDM channels) depend on their relative phases, and its effect accumulates for long-distances propagation. The power of the component at frequency f_{ijk} can be computed from the powers at frequencies f_i, f_j, f_k as [140]

$$P_{ijk} = 4\gamma_{FWM}^2 \cdot P_i P_j P_k \cdot L_{eff}^2 \eta e^{-\alpha L}, \tag{3.42}$$

where

$$\gamma_{FWM} = \frac{2\pi \cdot n_2}{\overline{\lambda} \cdot A_{eff}} \tag{3.43}$$

is the nonlinear coefficient at the average wavelength $\overline{\lambda}$,

$$\eta = \frac{\alpha^2}{\alpha^2 + \Delta\beta^2}\left[1 + \frac{4e^{-\alpha L}\sin^2\left(\frac{\Delta\beta L}{2}\right)}{\left(1 - e^{-\alpha L}\right)^2}\right], \tag{3.44}$$

supposing the same attenuation coefficient α for all the frequency components, and

$$\Delta\beta = \beta(\omega_i) + \beta(\omega_j) - \beta(\omega_k) - \beta(\omega_{ijk}). \tag{3.45}$$

From Eq. 3.44 the maximum effect of FWM takes place when $\Delta\beta = 0$. Considering equispaced WDM channels, $\Delta\beta$ can be related with the dispersion coefficient D as

$$\Delta\beta = -\frac{4\pi D\overline{\lambda}^2}{c} \cdot (\Delta f)^2, \tag{3.46}$$

where Δf is the channel spacing. So the condition $\Delta\beta = 0$ is satified for $D = 0$. Dispersion shifted fibers with zero dispersion cause the highest FWM, which leads to crosstalk among the various channels.

Even if they have been treated as different effects, SPM, XPM, and FWM arise from the same nonlinear effect (the Kerr effect), and they differ in terms of degeneracy of the involved wavelengths.

3.2.1 Schrödinger Nonlinear Equations for simulation of nonlinear fiber impairments

In the simulation tool, by imposing the presence of nonlinear effects, the three previously described effects (SPM, XPM and FWM) are set to impair the propagating signal. For a single-channel propagation, the only nonlinear contribution arises from SPM, while also the other two effects are detrimental for multichannel propagation, which is already worsened by interchannel crosstalk, as it will be further analyzed in Section 4.3. The fiber algorithm is applied span per span, and at the end of each span the optical field is multiplied by $\sqrt{\alpha \cdot l_{span}}$, ($\alpha$ is the linear attenuation and l_{span} is the length of the span) to recover the original launch power, and then it crosses the next MAN node.

Interaction with linear and nonlinear effects can cause temporal and spectral properties of the optical pulse to significantly change.

The idea is to divide each fiber span in steps. The length of each step has to be optimized: it has to be short enough to approximate the propagation in the best way, but preventing a high computational time. The length of the step is a measure of the accuracy in the solution of the wave equation. The step has to be set adaptively with power. The nonlinear impairments, which have a more significant impact at the beginning of the propagation where the power is higher, cause a phase rotation which requires a short step to be estimated. Due to the exponential reduction of the power caused by fiber attenuation, a longer propagation causes the power to approach the one obtained in linear regime, since the impact of nonlinearities decreases with power. This allows to set a longer step to emulate the power profile.

Two kinds of equations are employed to generate the step adaptation: Non-Linear Schrödinger Equations (NLSEs) and Coupled Non-Linear Schrödinger Equations (CNLSEs). NLSE is employed in absence of fiber birefringence. It is a mathematical model commonly used to describe the slowly-varying envelope of the optical field. This condition arises when the amplitude variation on a transmission length comparable to the wavelength is almost negligible [141]. It is solved by a split-step Fourier algorithm with a variable step to obtain a maximum phase rotation on each step equal to a given value. Alternatively, this step can be adaptively determined considering a target truncation error. Its general form can be expressed as [142]

$$\frac{\partial A}{\partial z} = -\frac{1}{2}\alpha A - \beta_1 \frac{\partial A}{\partial t} + \frac{j}{2}\beta_2 \frac{\partial^2 A}{\partial^2 t} + \frac{1}{6}\beta_3 \frac{\partial^3 A}{\partial^3 t} - j\gamma_{PM}|A|^2 A, \tag{3.47}$$

where $A = A(z,t)$ is the complex envelope of the optical signal at time t and position z along the fiber, α is the fiber attenuation loss, γ_{PM} is the nonlinear coefficient of the fiber, and β, the phase constant of wave propagation constant,

can be expressed as

$$\beta_k = \left[\frac{\partial^k \beta}{\partial^k \omega}\right]_{\omega=\omega_0}. \tag{3.48}$$

The first order derivative $\beta_1 = 1/v_g$ is the inverse of the group velocity, and in presence of this only component

$$A(z,t) = A\left(0, t - \frac{z}{v_g}\right).$$

The second-order β_2 and third order β_3 of β provide the Group Velocity Dispersion (GVD) parameters: the fiber dispersion D and the fiber dispersion slope D', respectively, where

$$\beta_2 = -\frac{\lambda^2}{2\pi c} D \tag{3.49}$$

and

$$\beta_3 = \left(\frac{\lambda}{2\pi c}\right)^2 (2\lambda D + \lambda^2 D'). \tag{3.50}$$

For small values of the fiber step, the interplay between dispersion and nonlinearities can be neglected, and so the two effects can be assumed statistically independent. This leads to the definition of two operators, $\hat{D}$ and $\hat{N}$, taking into account the fiber attenuation and dispersion ($\hat{D}$) and the fiber nonlinearities ($\hat{N}$) respectively [143]. The linear operator $\hat{D}$ is formulated as

$$\hat{D} = -j\frac{\beta}{2}\frac{\partial^2}{\partial\tau^2} + \frac{\beta_3}{6}\frac{\partial^3}{\partial\tau^3} - \frac{\alpha}{2}, \tag{3.51}$$

while the nonlinear operator $\hat{N}$ is described by the following equation:

$$\hat{N} = j\gamma_{PM}|A|^2. \tag{3.52}$$

$\tau = t - \frac{z}{v_g}$ is the reference time frame moving at the group velocity; Eq. (3.47) can be expressed as

$$\frac{\partial A}{\partial z} = \left(\hat{D} + \hat{N}\right) A. \tag{3.53}$$

So, the variation of the complex envelope in the propagation from z to $z + \Delta z$ can be approximated as

$$A\left(z + \Delta z, \tau\right) \approx e^{\Delta z \hat{D}} \cdot e^{\Delta z \hat{N}} A\left(z, \tau\right). \tag{3.54}$$

NLSE neglects the presence of polarization effects. CNLSE takes into account them: $\mathbf{A} = \mathbf{A(z,t)}$ is no more a scalar function, but it is the Jones vector representation of the complex envelope of the optical signal (so the representation in bold letters) for each time instant and for each propagation distance. The general expression neglecting the fiber slope is [144]

$$\begin{aligned}\frac{\partial \mathbf{A}}{\partial z} = -\frac{1}{2}\alpha\mathbf{A} - j\frac{\Delta\beta_0}{2}(l(z)\cdot\overrightarrow{\sigma})\mathbf{A} - \frac{\Delta\beta_1}{2}(l(z)\cdot\overrightarrow{\sigma})\frac{\partial \mathbf{A}}{\partial \tau} + \\ + \frac{j}{2}\beta_2\frac{\partial^2\mathbf{A}}{\partial\tau^2} - j\gamma\left[|\mathbf{A}|^2\mathbf{A} - \frac{1}{3}\left(\mathbf{A}^T\sigma_3\mathbf{A}\right)\sigma_3\mathbf{A}\right].\end{aligned} \tag{3.55}$$

Due to fiber imperfections, at each point along the fiber there exists a preferred direction perpendicular to its axis. A light field polarized orthogonal to this direction has the smallest phase and group velocity. $\Delta\beta_0 = \beta_f - \beta_s$ is the difference between the propagation constant of the wave polarized in the preferred direction (β_f) and the propagation constant of the orthogonally-polarized wave (β_s) [144]. $\Delta\beta_0$ is the birefringence parameter, while $\Delta\beta_1 = \partial\beta_f/\partial\omega - \partial\beta_s/\partial\omega$ is the specific group delay per unit length.

By comparing CNLSE with the scalar NLSE, two further terms appear in the linear part due the birefringence, $j\frac{\Delta\beta_0}{2}\cdot(l(z)\cdot\overrightarrow{\sigma})\mathbf{A}$ and $\frac{\Delta\beta_1}{2}(l(z)\cdot\overrightarrow{\sigma})\frac{\partial\mathbf{A}}{\partial\tau}$: the propagation of a polarized optical field through a birefringent fiber causes the propagation constant to be dependent on the field polarization. Birefringence varies both in time (slowly, compared to the symbol period, so that it can be assumed constant in the period τ) and along fiber length, according to the geometrical and physical characteristics of the fiber and to the ambient conditions, such as temperature. At each position z, the fiber is characterized by an eigenmode $l(z)$ [145], corresponding to the field polarization with the slowest propagation constant $\beta_s(\omega)$; on the other hand, the orthogonal eigenmode $l_0(z)$ is the field polarization with the fastest propagation constant $\beta_f(\omega)$ [146]. In Eq. (3.55), the Stokes vector $W(z,\omega) = (\Delta\beta_o + \Delta\beta_1\omega)l(z)$, which has a linear frequency dependence, models the birefringence; the variations in z of its orientation cause "*random mode coupling*", *i.e.*, the energy exchange

between the field components parallel or perpendicular to $l(z)$: this can lead to PMD [147]. When the frequency dependent term $\Delta\beta_1$ is set to zero, the pulse is not distorted, and the birefringence causes only a rotation of the signal SOP.

$\overrightarrow{\sigma}$ is the *spin-vector*, an intrinsic form of angular momentum carried by elementary particles whose elements are the three Pauli matrices; the scalar product $l(z) \cdot \overrightarrow{\sigma}$ generates a unitary Jones matrix, *i.e.*, a 2×2 complex matrix with unit determinant, that acts on the elements of the field vector $\mathbf{A}$ and produces mode-coupling [148]. A third new term appears in CNLSE with respect to NLSE, which is responsible for the nonlinear part: it is due to the circular component of the signal polarization and it is related to the third of the three Pauli matrices σ_3.

The CNLSE can be simplified averaging the impact of signal polarization over the nonlinear term and in this case it is known as the Manakov-PMD equation [149]. In this formulation, the nonlinear term introduces phase rotations that do not alter the signal SOP; moreover, nonlinear distortions only depend on the signal intensity and not on its polarization, although there is an interplay between the nonlinear distortions and the polarization distortions due to the linear term. The CNLSE uses the same rules of NLSE except that at each step a new Polarization Maintaining Fiber (PMF) is generated; indeed in the general case with two polarizations, the fiber is the concatenation of randomly-oriented PMFs.

3.2.1.1 Validation of the simulation of nonlinear effects

This approach for the simulation of nonlinear effects has been validated by comparing the SNR obtained with the implemented simulator and with a commercial simulator (OptSim™ by Synopsys® [150]). This comparison has been performed for both a single-channel and three-channel transmission, considering the 25-GHz channel spacing; each channel has been generated with

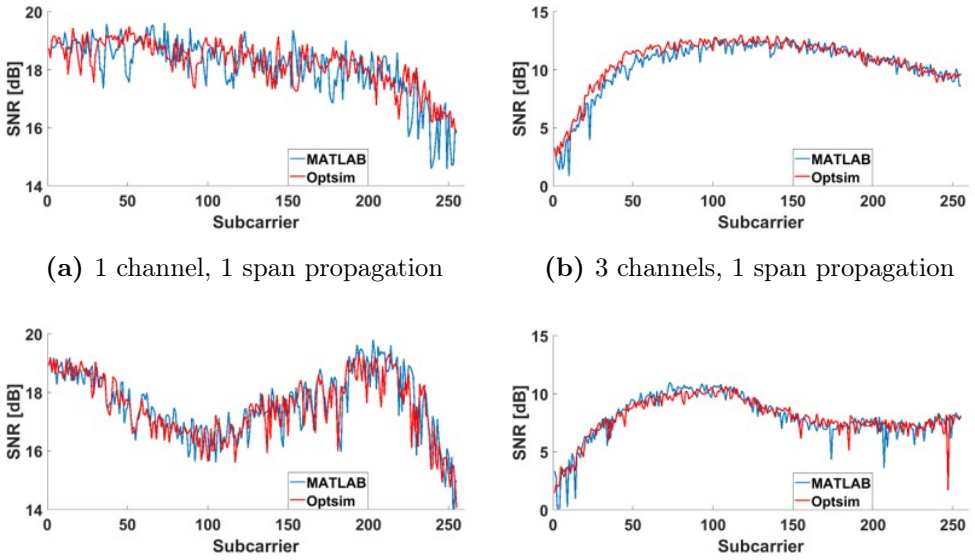

(a) 1 channel, 1 span propagation

(b) 3 channels, 1 span propagation

(c) 1 channel, 3 spans propagation

(d) 3 channels, 3 spans propagation

Figure 3.8: Comparison between SNRs obtained with MATLAB® simulator and commercial simulation tool.

a VCSEL which is directly modulated with a 10-GHz DSB DMT electrical signal. The optical power of the transmitted channels is set to be 10 dBm. Such a high power has been chosen since the nonlinear effects have a strong impact for high signal powers, so the comparison between the results is more significant. The signal propagates for a given number of SSMF spans of 35 km, up to three spans. After each span, the power is recovered to 10 dBm with an EDFA with a NF of 6 dB. The signal is then coherently detected with a coherent receiver exploiting 13 dBm per polarization LO. In case of the simulations performed in OptSim™, the optical signal is generated and detected with the implemented MATLAB® simulator, and then imported in and exported from the commercial tool respectively.

Four simulation scenarios have been analyzed: a single channel transmission with a single span propagation; a single channel transmission with a three-span propagation; a three-channel transmission with a single span propagation; a three-channel transmission with a three-span propagation. Figure 3.8 shows the

comparison between the SNRs for the four simulated scenarios. There is a good matching between the results obtained with the MATLAB® simulator and with the commercial tool. This verifies the accuracy of the results obtained with the MATLAB® simulator in terms of impairments due to fiber propagation when nonlinear effects are taken into account. By increasing the number of spans, the nonlinear effects have a more significant impact with respect to a single-span propagation, and they introduce a distortion in the measured SNR. The interchannel crosstalk induced in presence of three WDM 25-GHz channels causes the first 50 subcarriers to be heavily impaired, while XPM and the SPM of the other two channels reduce the SNR of more than 40% on average with respect to the single-channel system.

3.3 OSNR assessment in EDFA-based multispan networks

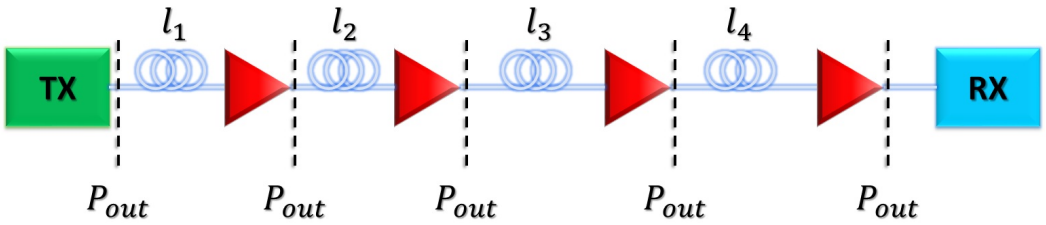

Figure 3.9: Schematic of a multispan propagation with spans of different lengths.

As previously introduced, after each span of fiber propagation, the signal power has to be recovered before being filtered by the network nodes; in this thesis EDFAs are the amplifiers employed to restore the signal power. EDFAs are fiber optical amplifiers, widely used in long-range optical communications thanks to an efficient amplification of light at 1550 nm. In the simulation tool the EDFAs are emulated as a constant gain G and an additive optical noise worsening the OSNR of the system. This subsection is focused on the effect of the presence of one or more in-line EDFAs on the OSNR.

For a single span the OSNR at the output of an amplifier is defined as the ratio between the output power of the amplifier P_{out} and the power of the ASE P_{ASE} it introduces:

$$OSNR = \frac{P_{out}}{P_{ASE}}. \tag{3.56}$$

The power of the introduced ASE at the optical frequency ν can be computed as

$$P_{ASE} = 2n_{sp} \cdot h\nu \cdot \Delta\nu \cdot (G-1), \tag{3.57}$$

where n_{sp} is the spontaneous emission factor, h is the Planck's constant, and $\Delta\nu$ is the optical bandwidth. By hypothesis, the EDFA has to completely recover the power of the signal, so its gain has to be set equal to the power losses introduced during fiber propagation:

$$G_{dB} = \alpha_{f_{(dB/km)}} \cdot l_{span} = L_{span_{(dB)}},$$

where G_{dB} is the gain of the EDFA in logarithmic units, $\alpha_{f_{(dB/km)}}$ is the fiber attenuation coefficient, l_{span} is the length of the span, and L_{span} is the overall accumulated loss during propagation in the given span. For high values of G ($G \gg 1$), $G - 1 \approx G$, and $NF \approx 2n_{sp}$, where NF is the noise figure of the amplifier. The NF is the degradation of the SNR after the signal amplification expressed in logarithmic units. In linear units this phenomenon is evaluated with the Noise Factor F, so

$$\begin{aligned} F &= \frac{SNR_{in}}{SNR_{out}}, \\ NF &= 10 \cdot \log_{10}(F). \end{aligned} \tag{3.58}$$

So Eq. (3.57) can be rewritten as follows:

$$P_{ASE} \approx NF \cdot h\nu \cdot \Delta\nu \cdot 10^{L_{span_{dB}}/10}. \tag{3.59}$$

By expressing Eq. (3.59) in logarithmic units

$$P_{ASE_{dBm}} = 10 \cdot \log_{10}(h\nu \cdot \Delta\nu) + NF + L_{span_{dB}}, \tag{3.60}$$

Eq. (3.56) can be expressed in logarithmic units as

$$\begin{aligned} OSNR_{dB} &= P_{out(dBm)} - P_{ASE(dBm)} = \\ &= P_{out(dBm)} - 10 \cdot \log_{10}(h\nu \cdot \Delta\nu) - NF - L_{span_{dB}}. \end{aligned} \tag{3.61}$$

The OSNR is computed on a given bandwidth. A typical OSNR bandwidth, which is also used in this thesis, is the 0.1 nm bandwidth, corresponding to $\Delta\nu = 12.5$ GHz for a wavelength of 1550 nm. So $10 \cdot \log_{10}(h\nu \cdot \Delta\nu) = -58$ dBm and $OSNR_{dB} = P_{out_{dBm}} - NF - L_{span_{dB}} + 58_{dBm}$.

Eq. (3.61) expresses the OSNR for a single span propagation. From Eq. (3.60) and Eq. (3.61) the OSNR computation can be extended to a several span propagation [151]. Supposing to have N spans, each one of different length $l_{span}(i)$ (so accumulating a different loss $L_{span}(i)$) as in Figure 3.9, the overall ASE power is the sum of the noise contributions $P_{ASE_{span}}(i)$ of the N amplifiers:

$$P_{ASE} = \sum_{i=1}^{N} P_{ASE_{span}}(i) = NF \cdot h\nu \cdot \Delta\nu \cdot \sum_{i=1}^{N} 10^{L_{span_{dB}}(i)/10} \tag{3.62}$$

For the sake of simplicity, the NF of all the amplifiers is the same, and each one of them has to recover the signal power to the wanted value P_{out}. The OSNR is then computed from the OSNRs of the separate spans $OSNR_{span}(i)$ as follows:

$$\frac{1}{OSNR} = \frac{\sum_{i=1}^{N} P_{ASE_{span}}(i)}{P_{out}} = \sum_{i=1}^{N}, \frac{1}{OSNR_{span}(i)}. \tag{3.63}$$

$$OSNR = \frac{1}{\sum_{i=1}^{N} \frac{1}{OSNR_{span}(i)}} \tag{3.64}$$

If all the spans have equal lengths, $P_{ASE_{span}}(i) = P_{ASE_{span}}, \forall i = 1...N$, so the overall ASE power is

$$P_{ASE} = N \cdot P_{ASE_{span}}, \tag{3.65}$$

and the OSNR in logarithmic unit can be obtained from Eq. (3.61) as

$$OSNR_{dB} = P_{out_{(dBm)}} - 10 \cdot \log_{10}(h\nu \cdot \Delta\nu) - NF - L_{span_{dB}} - N. \quad (3.66)$$

The noise level introduced by the EDFAs of the network can be calculated from the overall OSNR computed in Eqs. (3.63)-(3.64) and then it is added to the useful signal as an Additive White Gaussian Noise (AWGN) before the detection.

3.4 Two-level hierarchy of MAN network nodes

The network nodes (HL4 and HL3) are simulated with the TFs of the filters composing the nodes (in Chapter 5 the effect of Semiconductor Optical Amplifers (SOAs) on the system performance will be taken into account as well).

The HL4 nodes are emulated with the cascade of two 50-GHz spacing filters, which are flat-top AWGs with bandwidth of 40 GHz, as depicted in Figure 3.10. As it will be further described in Section 4.5, this kind of nodes has a much lower impact on the system performance than HL3 nodes. HL3 nodes are composed of a couple of MUX/DEMUX, designed for 100-GHz spacing, and a 25-GHz spacing filter, as depicted in the simplified structure of the HL3 node in Figure 3.11. The latter has to select the 25-GHz spacing channel, so it has to be designed as steeper as possible. The solution implemented in this thesis is the employment of a Wavelength Selective Switch (WSS).

3.4.1 Wavelength Selective Switch

A Wavelength Selective Switch (WSS) is a photonic device which allows the switching of several wavelengths among multiple fibers. The structure of the WSS considered in this thesis uses a Liquid Crystal on Silicon (LCoS) switching element, as introduced in [153]. LCoS is a technology which combines liquid

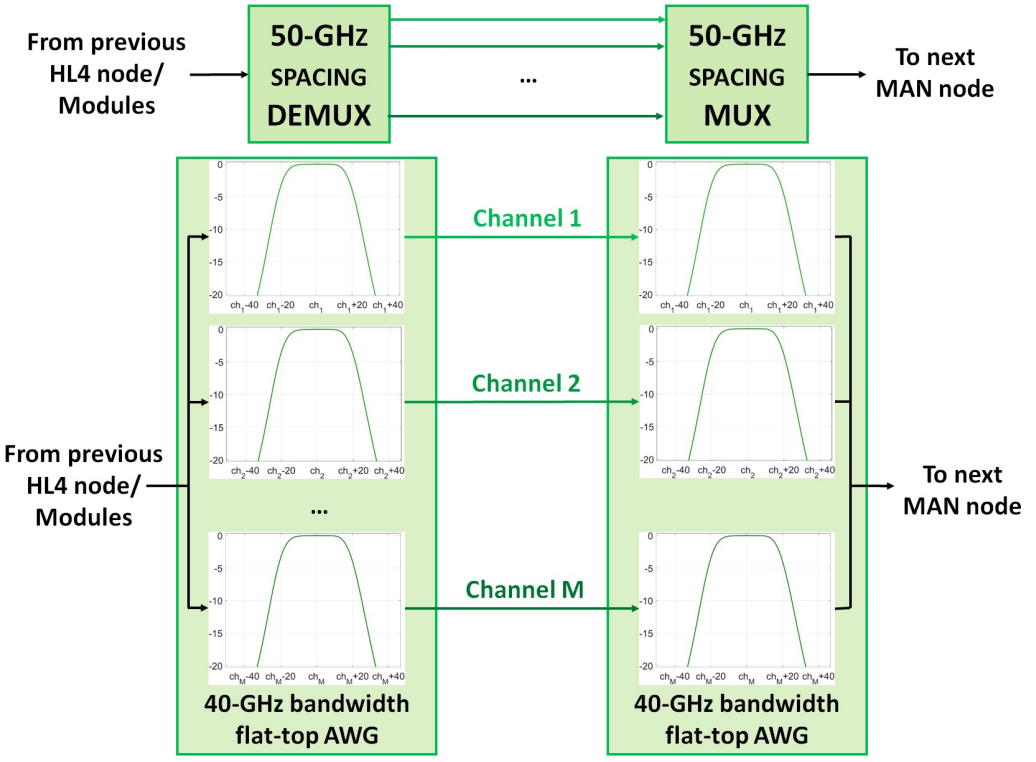

Figure 3.10: Schematic of the HL4 node as implemented in the MATLAB® simulator.

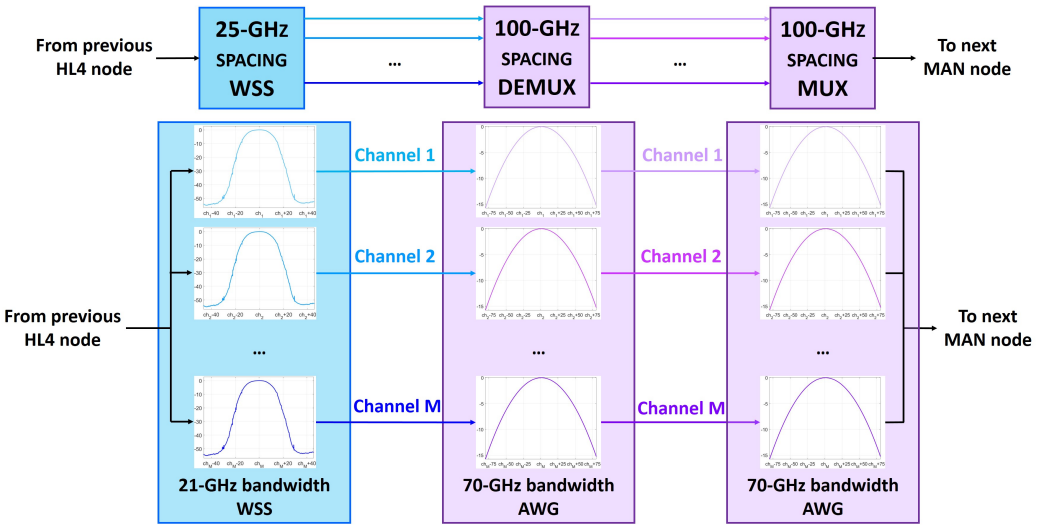

Figure 3.11: Schematic of the HL3 node as implemented in the MATLAB® simulator.

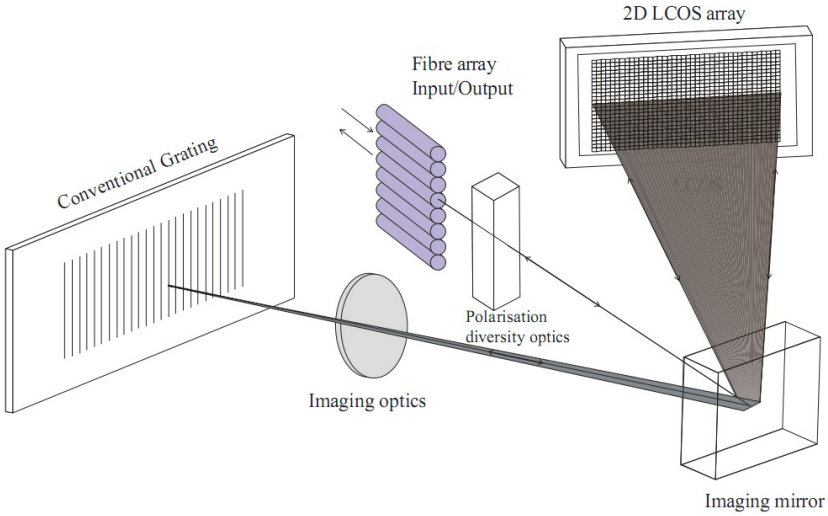

Figure 3.12: Schematic of functioning of a LCoS-based WSS as shown in [152].

crystals with semiconductor technologies. As shown in Figure 3.12, the input optical signal passes through polarization diversity optics before impinging on a diffraction grating. The diffracted light is then focused onto a 2D array of LCoS pixels, where each pixel is individually addressed and induces a phase retardation from 0 to 2π. In one axis, a phase ramp is created to convey the beam to a desired output fiber [154]. The focus of this thesis is not to go into detail of the physical structure of the device, but, following the work presented in [152], to exploit it to infer a model of the channel shape of a WSS.

The output optical amplitude spectrum of a WSS is modelled to be the convolution of a rectangular function, emulating an aperture formed at the image plane of spatially diffracted light, with the Optical Transfer Function (OTF) of the device. The rectangular function is given by

$$R(f) = \begin{cases} 1, & \text{if } -\frac{B}{2} \leq f \leq \frac{B}{2} \\ 0, & \text{otherwise} \end{cases}, \tag{3.67}$$

where B is the width of the rectangular aperture in frequency, which coincides with the desired channel spacing. The OTF is assumed to be Gaussian, and

its normalized frequency response can be expressed as

$$L(f) = \exp\left[-\frac{f^2}{2\sigma_{OTF}^2}\right]. \tag{3.68}$$

The standard deviation σ_{OTF} is related to the -3 dB bandwidth of the OTF BW_{OTF} as

$$\sigma_{OTF} = \frac{BW_{OTF}}{2\sqrt{2\ln 2}}. \tag{3.69}$$

BW_{OTF} is supposed to be constant over the frequency range of the device, and it represents the focus of the beam in the aperture plane.

The convolution $S(f)$ between $R(f)$ and $L(f)$ leads to the expression of the optical field spectrum of the bandpass filter of a WSS

$$S(f) = \frac{1}{2}\sigma_{OTF}\sqrt{2\pi}\left[\mathrm{erf}\left(\frac{\frac{B}{2}-f}{\sqrt{2}\sigma_{OTF}}\right) - \mathrm{erf}\left(\frac{-\frac{B}{2}-f}{\sqrt{2}\sigma_{OTF}}\right)\right], \tag{3.70}$$

where $\mathrm{erf}(x)$ is the error function. $S(f)$ is the amplitude spectrum of the device, so it takes into account the phase behaviour of WSS channels as well.

The channel shape of the WSS can be modified by properly varying the value of OTF bandwidth: a lower value of B_{OTF} induces a steeper transfer function, the value of bandwidth B being fixed, since B_{OTF} gives an indication on the spot size (a small spot size implies a reduced value of B_{OTF}) [155], as demonstrated in Figure 3.13(b).

When several WSS filters are cascaded, it results a bandwidth narrowing which has to be considered in the design of optical networks (see Figure 3.13(b)). The cascade of N WSS devices, supposed to be identical and ideal in terms of filter response, induces a multiplication of the bandpass filter spectra [156]. The p-dB bandwidth of the overall transfer function can be estimated as

$$BW_{casc}(p, N) = BW_{p/NdB}, \tag{3.71}$$

i.e., the p-dB bandwidth of the cascaded filters is equal to the p/N bandwidth of a single unit (*e.g.*, supposing to have the cascade of 3 equal WSS, the -3 dB bandwidth of the cascade is equal to the -1 dB bandwidth of a single WSS).

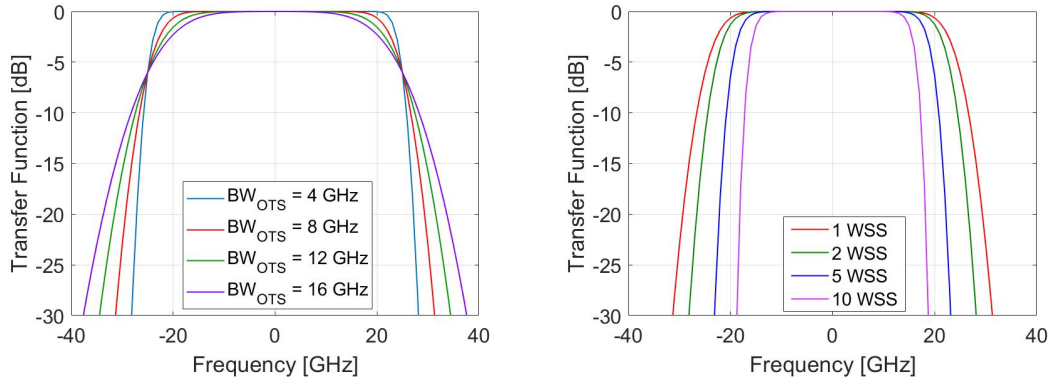

(a) TF of a 50-GHz WSS for several values of BW_{OTF}.

(b) TF of the cascade of several 50-GHz WSS for $BW_{OTF} = 8\ GHz$.

Figure 3.13: TFs of 50-GHz WSS.

The m-dB bandwidth of a passband WSS, defined as the spectral width at the left and right points which are m dB lower than the central peak power, can be computed as follows:

$$BW_{m-dB} = B - 2\sqrt{2}\sigma_{OTF} \cdot E_m, \tag{3.72}$$

where E_m is

$$E_m = \text{erfinv}\left[2\sqrt{10^{m/10}} \cdot \text{erf}\left(\frac{B}{2\sqrt{2}\sigma_{OTF}}\right) - 1\right], \tag{3.73}$$

where $\text{erfinv}(x)$ is the inverse error function.

In order to implement the HL3 node WSS in the simulator and obtain a realistic behaviour of the WSS, the 25-GHz WSS TF has been emulated with a Waveshaper. Figure 3.14 shows the comparison between the theoretical and the emulated TFs. The Waveshaper is not able to follow the steepness of the filter; this results in a reduction of the bandwidth of approximately 2 GHz and a less efficient filtering of high frequencies, leading to a more significant crosstalk arising from adjacent channels in a 25-GHz frequency comb.

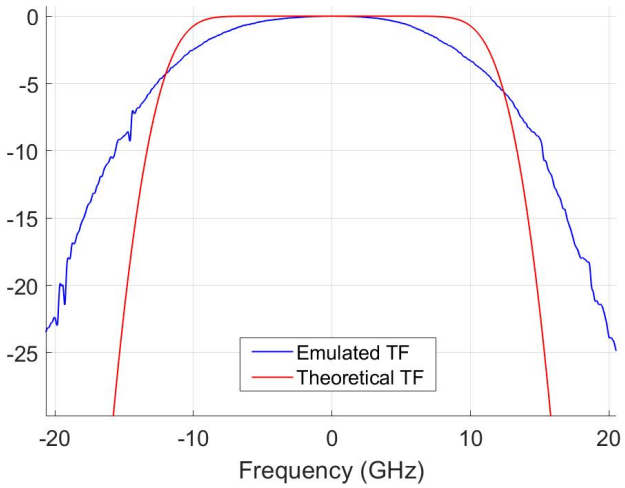

Figure 3.14: Comparison between theoretical TF and emulated TF for 25-GHz channel spacing WSS.

3.5 Simplified coherent detection of DMT signals

At the receiver side, the steps to create the DMT signal are reversely performed to receive it. In case of coherent detection, the signal electric field $E_s(t)$ is reconstructed as introduced in Section 2.4 and the CD is compensated. If the overall accumulated CD is

$$D(f) = \exp\left[j \cdot (2\pi f)^2 \cdot \frac{\beta}{2} \cdot L\right], \tag{3.74}$$

at the receiver side the phase contribution

$$\overline{D}(f) = \exp\left[-j \cdot (2\pi f)^2 \cdot \frac{\beta}{2} \cdot L\right] \tag{3.75}$$

is multiplied to $E_s(f)$ to avoid the distortions induced by CD. Considering a simplified version of the coherent receiver, on the field $\overline{E_s}(f) = E_s(f) \cdot \overline{D}(f)$ the squared modulus is applied, and the DSP is computed on the intensity of $\overline{E_s}(f)$, as in the case of direct detection.

In order to correctly detect the received signal, finding the beginning of the symbol and the start of the frame are mandatory. To achieve this objective, a

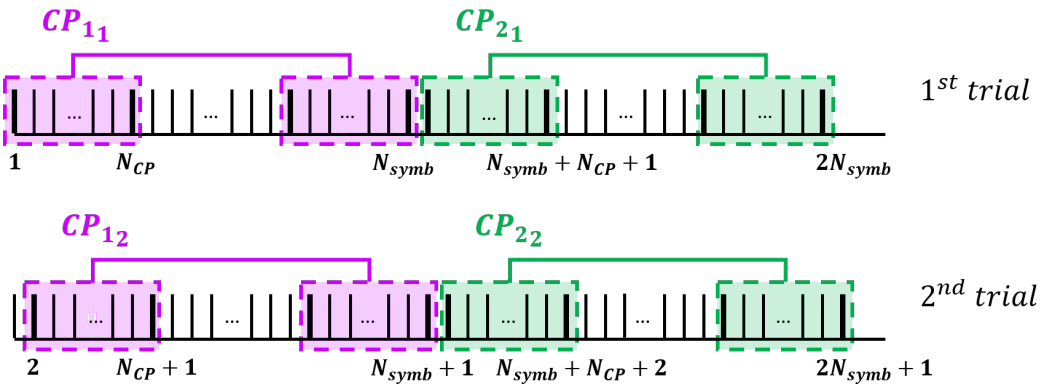

Figure 3.15: Schematic of the cyclic prefix functioning.

synchronization is performed in two steps [97]. A first step is aimed at locating the first sample of the symbol. CP has the purpose of both protecting from dispersion (as already introduced in 3.1.2) and identifying the symbol, and it is the replication of the last N_{CP} samples of the symbol, where N_{CP} is the length of the cyclic prefix. Since both the lengths of the CP N_{CP} and of the symbol N_{symb} are known in advance, for each symbol a portion of the stream of samples corresponding to a candidate CP is multiplied to the portion of N_{CP} samples which starts after $N_{symb} - N_{CP}$ samples. The following candidate CP is the one starting one sample after the previous one, and so on (Figure 3.15). This operation is repeated for all the N_{symb}. The correlation on the N symbols composing the signal is computed: the sample for which the correlation has its peak is the first one of the actual CP. This allows to locate the starting of the symbol (since it is N_{CP} samples apart). The symbols are then parallelized and the CP is then removed. The second phase of the synchronization involves the frame. In transmission a two-symbol training sequence from Schmidl and Cox's theory [157] is placed at the start of the frame as a header. The first symbol, modulated with a 64-QAM, is needed to evaluate the frame timing. The two halves of these alignment symbols are made identical in time order. At the receiver each symbol is split in two halves, and the correlation between them is computed. The maximum of the correlation coincides with the first

training symbol. The second one is used to evaluate the subchannel frequency offset by evaluating the phase offset between the two halves due to channel propagation.

This alignment is useful to understand the position of the training symbols needed to estimate the channel. Since they are symbols known in advance, they can be compared with symbols effectively detected, and so the correlation function can be applied to estimate the channel effect. The channel estimate is used to equalize the received symbols. In order to evaluate the SNR, the received symbols are then compared to the ideal ones. The Error Vector Magnitude (EVM) measures the distance between the positions of the points in the normalized received constellation S_{rx} and the ideal normalized symbols S_{id} [158]. For N symbols,

$$EVM = \sqrt{\frac{\frac{1}{N} \cdot \sum_{n=1}^{N} |S_{rx}(n) - S_{id}(n)|^2}{\frac{1}{N} \cdot \sum_{n=1}^{N} |S_{id}(n)|^2}}. \tag{3.76}$$

.

Assuming a Gaussian noise model, the EVM can be defined as

$$EVM = \sqrt{\frac{\frac{1}{N} \cdot \sum_{n=1}^{N} \left[|n_{I,t}|^2 + |n_{Q,t}|^2\right]}{P_0}} \tag{3.77}$$

where N is the number of symbols in a stream of data, $n_{I,t}$ and $n_{Q,t}$ are respectively the in-phase and quadrature noise components (*i.e.*, the distances from the ideal symbol), and P_0 is the power of the normalized transmitted constellation. The numerator of Eq. 3.77 sets up the normalized noise power. For a large number of symbols, the ratio between the normalized noise power and the normalized power of the ideal constellation can be approximated to their unnormalized values N_0 and E_s, leading to a different form of Eq. (3.77)

$$EVM \approx \sqrt{\frac{N_0}{E_s}} = \sqrt{\frac{1}{SNR}}. \tag{3.78}$$

By inverting Eq. (3.78), the SNR is approximated as the inverse of the squared EVM

$$SNR \approx \frac{1}{EVM^2}. \tag{3.79}$$

Moreover, reminding that for a M-ary modulation the BER is

$$BER = \frac{2\left(1-\frac{1}{\sqrt{M}}\right)}{\log_2 M} \cdot Q\left[\sqrt{\left[\frac{3\log_2 L}{2\left(M-1\right)}\right]\left[\frac{E_s}{N_0 \log_2 M}\right]}\right], \tag{3.80}$$

the relation between EVM and BER can be easily derived as

$$BER_{EVM} = \frac{2\left(1-\frac{1}{\sqrt{M}}\right)}{\log_2 M} \cdot Q\left[\sqrt{\left[\frac{3\log_2 M}{2\left(M-1\right)}\right]\left[\frac{1}{EVM^2 \cdot \log_2 M}\right]}\right]. \tag{3.81}$$

The BER computed from the EVM is an estimation of the real BER. The symbols are then demapped, and the signal is serialized again. At last, by comparing the transmitted stream of bits and the received one the real BER is computed.

Chapter 4

Simulative and experimental analyses of MAN networks

In this chapter some interesting results are introduced. First, a comparison between the experimental results and the ones obtained with the simulation tool discussed in Chapter 3 validates the accuracy of the tool itself. The maximum reach for given OSNRs and span lengths is presented. Then, the interplay between optical filtering and chirp parameters is studied, highlighting a different performance depending on the chirp and modulation of the source (DSB or SSB DMT signals) and on the number of optical filters. The effect of interchannel crosstalk is evaluated for three 25-GHz spaced WDM channels directly modulated with SSB DMT signal with 16-GHz and 20-GHz bandwidth, and the results are compared to the single-channel transmission. Via experimental evaluation, single-channel and three-channel transmissions are studied in terms of per-channel transmitted capacity in hundred-km multi-span propagation scenario, characterized by a span of MCF as well. The nonlinear impairments arising from the fiber propagation are mitigated by employing the 3rd order Volterra equalizer. The effect on node crossing is evaluated for an increasing number of HL4 and HL3 nodes up to 11 nodes for linear propagation in terms of minimum OSNR needed to achieve a target transmitted capacity

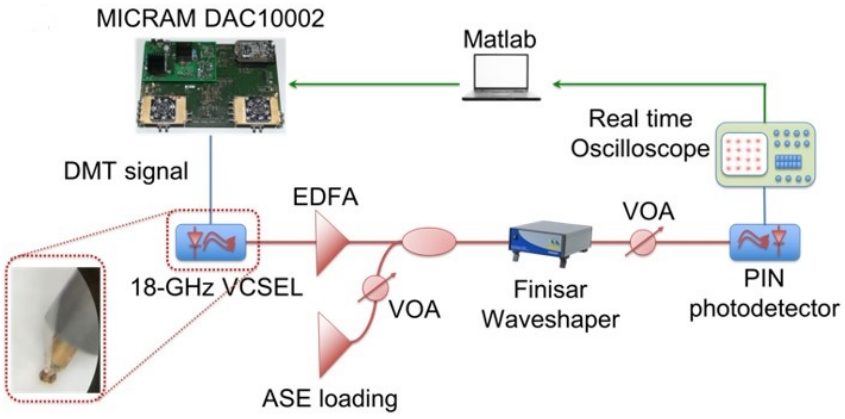

Figure 4.1: Experimental setup for the validation of the simulation tool.

(50 Gb/s, 40 Gb/s, and 25 Gb/s). At last, two case studies are analyzed, differing by the transmission lengths. The nonlinear impairments are taken into account in the evaluation of the transmitted capacity. The launch power is optimized for the cases in analysis, and a different distribution of EDFAs demonstrates a trade-off between the noise introduced by the amplifiers and the accumulated nonlinear impairments.

4.1 Transmission performance in presence of optical filtering: validation of the simulator

In Chapter 3 the MATLAB® simulator developed for this thesis has been presented. The results obtained with the setup shown in Figure 4.1 are aimed at validating this tool. A 18-GHz VCSEL is directly modulated by a DMT signal composed of 256 subcarriers in 20-GHz range, leading to a subcarrier spacing of 78.125 MHz. A Cyclic Prefix (CP) of about 2.1% of the symbol length is added. The VCSEL bias current is fixed at 9 mA, and the modulation depth is adjusted at 550 mV. These parameters are set to limit the insurgence of frequency chirp and to reduce the penalty due to SSB filtering. The DMT signal is generated by a MICRAM 100 GS/s digital-to-

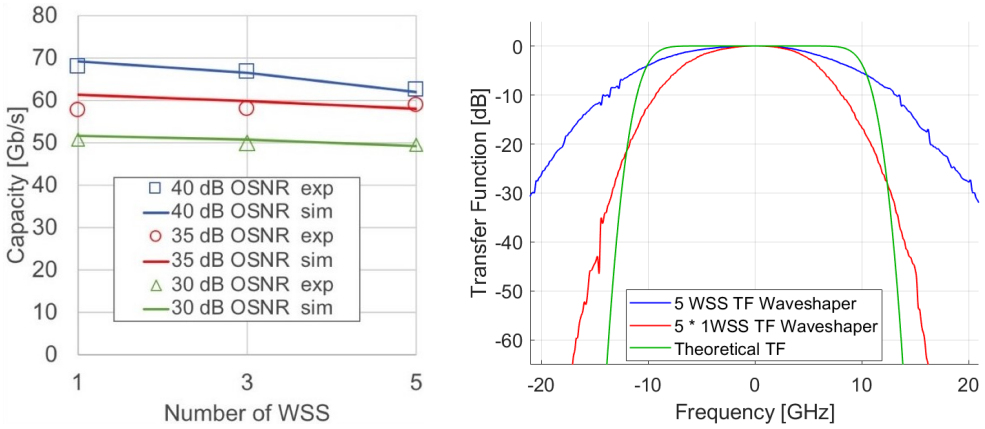

(a) Capacity **(b)** 5 WSS TFs

Figure 4.2: (a) Capacity dependence on the number of filters and OSNR; (b) Example of comparison among theoretical TF, cascaded Waveshaper TFs, and TF of the cascade of 5 WSS obtained with a Waveshaper.

analog converter (DAC10002) with 40-GHz electrical bandwidth and 6-bit vertical resolution. An EDFA amplifies the optical DMT signal and then it has its OSNR varied in the range between 30 dB and 40 dB by a noise source controlled by a Variable Optical Attenuator (VOA). A 25-GHz WSS [152], the Transfer Function (TF) of which is mimicked by a Finisar Waveshaper, is detuned of 9 GHz with respect to the VCSEL modulated spectrum to perform SSB filtering of the transmitted signal. In some simulation scenarios, two or four more WSS filters are crossed. The signal is then directly detected by a 28-GHz PIN photodiode at 0-dBm power. The received signal is at last acquired by a Tektronix real-time oscilloscope with 8-bit vertical resolution, 50 GS/s and 33-GHz electrical bandwidth, and the DSP described in Section 3.5 is performed. The target BER for the computation of the transmitted capacity (see Chapter 3.1.2.1 and [127]) is $3.8 \cdot 10^{-3}$, in order to exploit an advanced hard-decision FEC code with 7% overhead [159].

Figure 4.2(a) shows the capacity dependence on the number of crossed WSS filters and on the OSNR (open symbols). Lower OSNRs cause a reduction of

Span length	40 dB	35 dB	30 dB
35-km span	70 km	210 km	735 km
65-km span	–	65 km	260 km

Table 4.1: Reach for given values of OSNR.

the capacity. The increasing number of WSS filters slightly affects the capacity. This is due to the capability of the Waveshaper to reproduce the steepness of the WSS TF, as mentioned in Section 3.4. Figure 4.2(b) compares for 5 WSSs the TFs of the theoretical cascade, of the cascade of 5 filters each one characterized by the TF of a single WSS emulated by the Waveshaper, and the emulation by the Waveshaper of the theoretical cascade of 5 WSSs. The presented results have been obtained with the last filter configuration, which does not alter the carrier and the SSB spectrum even when several filters are crossed, but in case of multichannel propagation it would not perform an efficient filtering. This is the reason why the results discussed in the following sections have been achieved either with the theoretical WSS (in Section 4.2) or by cascading several single WSSs emulated by the Waveshaper (in all the other scenarios). In Figure 4.3 the dependence of the maximum reach for span lengths between adjacent filters/nodes of 35 km and 65 km are shown. The graphs have been obtained by plotting Eq. (3.66) for EDFAs with 6-dB NF, 0.25 dB/km fiber losses, and 0-dBm power per channel. In Table 4.1 the reaches for the analyzed OSNRs are summarized. The target capacity of 50 Gb/s is reached for an OSNR of 30 dB and up to 5 WSS filters, leading to more than 700 km of SSMF propagation in case of 35-km span length and 250 km for 65-km spans.

In Figure 4.2(a) the experimental results (open symbols) are compared with the ones obtained by simulations (continuous line) emulating all experimental conditions (such as VCSEL chirp, modulation depth, optical and electrical bandwidths of the devices, bit resolution of DAC and ADC, WSS

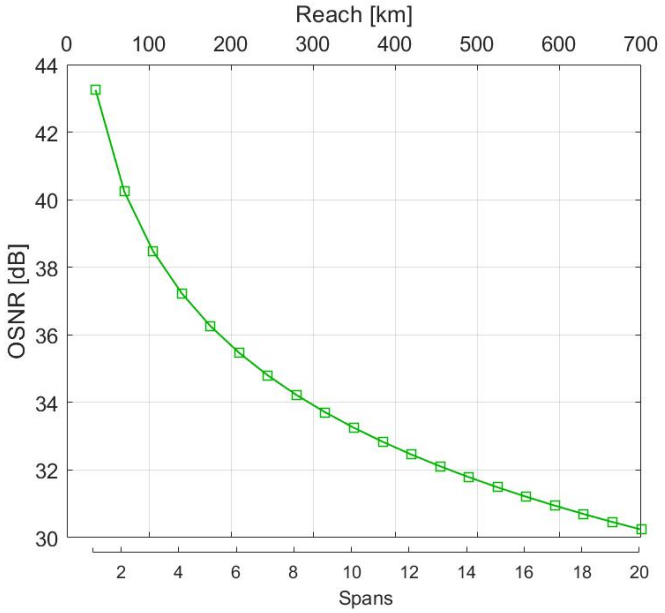

(a) 35 km

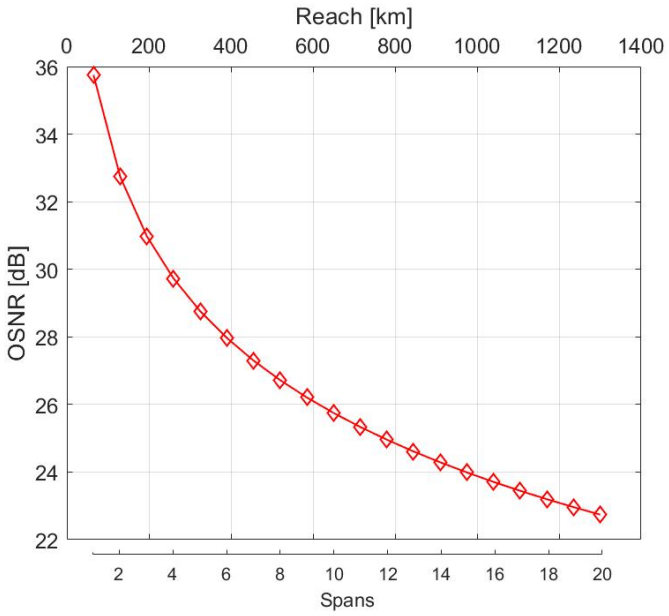

(b) 65 km

Figure 4.3: OSNR dependence on the span length.

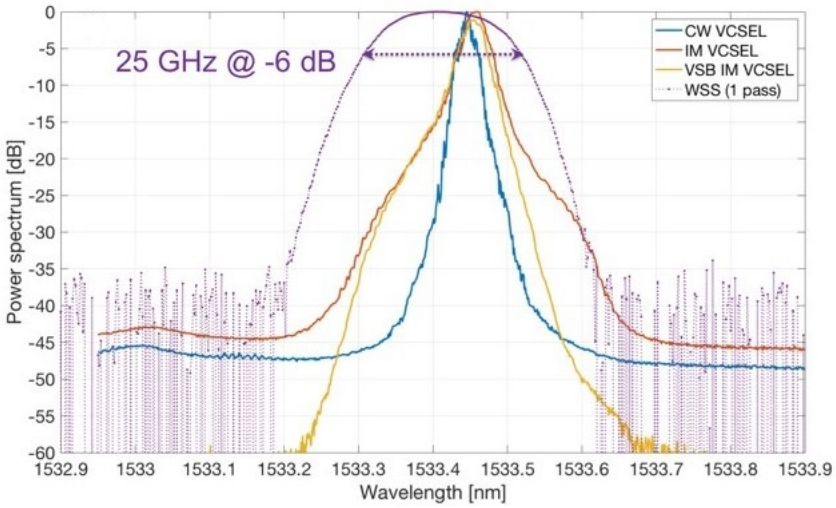

Figure 4.4: Comparison among power spectra of the CW VCSEL (in blue), of the IM VCSEL with a DSB DMT signal (in red), of the IM VCSEL with a VSB DMT signal (in yellow), and of the 25-GHz WSS (in violet).

TF, Photodiode (PD) Noise Equivalent Current (NEC) and received powers). The good agreement between them guarantees the accuracy of the simulation tool.

Figure 4.4 depicts the spectrum of the SSB signal (in yellow) obtained by detuning the WSS filter (the spectrum of which is represented in violet) of a proper frequency to select only the left-sideband of the 20-GHz DMT DSB spectrum (in red), taking care to preserve the optical carrier. The emulated WSS TF has limited extinction, with maximum out-of-band attenuation of 40 dB. The right sideband of the optical spectrum is correctly filtered out; on the other hand, by comparing the yellow and the red curves, the last subcarriers on the left (around 1533.3 nm) face a slight reduction due to the tight filtering [160].

4.2 Estimation of VCSEL chirp parameters and their interplay with optical filtering

In Subsection 3.1.1 the characterization of an optical source in terms of its chirp parameters from the uncompensated channel TF has been presented. This technique of analysis has been exploited to measure the chirp parameters of two different optical sources [161]:

1. a 20-GHz long-wavelength VCSEL emitting at 1533.4nm [46], which is based on a short-cavity design;

2. an 8-GHz VCSEL emitting in the third fiber window and tunable over about 70 nm thanks to a Micro Electro-Mechanical Systems (MEMS) top-mirror [162].

Due to their specific technology, the two devices show different chirp performances. The evaluation of the dependence of the transmitted capacity on the interplay between source chirp parameters and optical filtering envisages two separate phases: an experimental chirp parameter estimation and the simulation of a single-channel optical network characterized by DMT Direct Modulation (DM) of the VCSEL source, WSS filtering and COH-D.

4.2.1 Chirp parameters estimation

Figure 4.5 shows the schematic of the experimental setup exploited for VCSEL chirp parameter estimation. A 40-GHz bandwidth Vector Network Analyzer (VNA) directly modulates the long-wavelength VCSEL, by generating an RF signal for the small-signal modulation analysis. The laser bias current is 9 mA, and the source emits around 2.5 mW. On the other side, the tunable VCSEL bias current is 16 mA, the emitted power is approximately 0.9 mW, and the MEMS bias current is set to 20 mA, for a temperature of 25°C kept constant by a standard temperature controller. The optical signal then propagates in

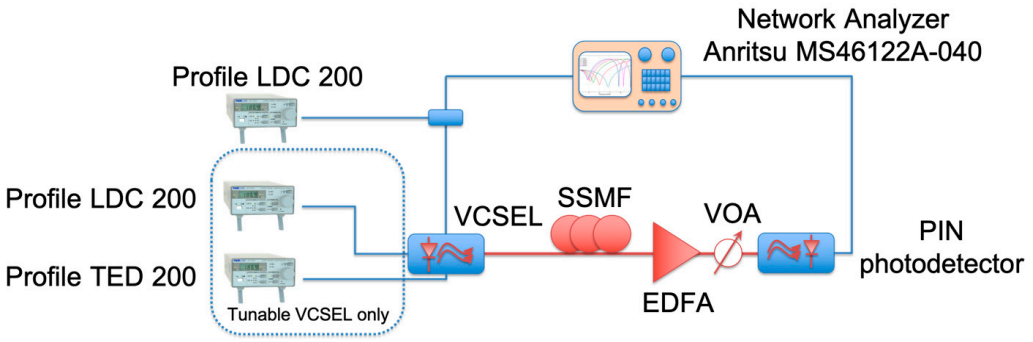

Figure 4.5: Schematic of the experimental setup to evaluate the chirp parameters.

an SSMF coil, the length of which ranges from 10 km to 34 km in order to accumulate different amounts of CD. At last it is directly detected by a Positive-Intrinsic-Negative (PIN) photodiode with 25-GHz electrical bandwidth preceded by an EDFA.

At first, in order to solely measure the fiber power TF, all the other contributions have to be excluded, so the spectral distortions due to both the Electro-optic (E/O) and Opto-electronic (O/E) processes in optical Back-to-Back (BTB), along with the VCSEL and receiver TFs, are measured and removed. In order to determine the source chirp parameters, the uncompensated TF of the channel in presence of a DML laser modelled by Eq. (3.9) [114]

$$H(\omega) = \left|\cos\vartheta - \sin\vartheta \cdot \alpha \left(1 - j\frac{\omega_c}{\omega}\right)\right| \tag{4.1}$$

is compared with the measured fiber TF curves to find α and κ which best fit the real curves. Figure 4.6 compares the theoretical (dashed curves) and the measured (continuous lines) frequency responses for the tunable and short-cavity VCSEL sources on 10-GHz and 25-GHz ranges, respectively. The different frequency ranges reflect the dissimilar E/O bandwidths. The frequency dips move towards lower frequencies when the accumulated dispersion increases; this reduces the undistorted region of the electrical spectrum. The different positions and depths of the first frequency dip of the two lasers confirm the dissimilar chirp regime of the two sources. The tunable VCSEL is mainly

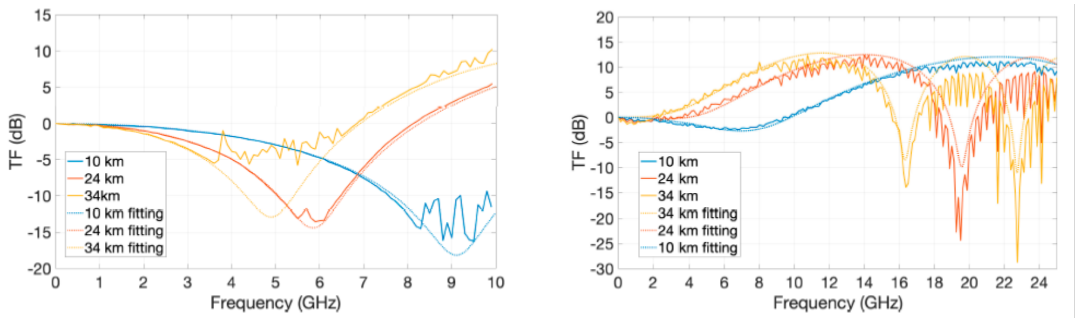

(a) 8-GHz tunable VCSEL **(b)** 20-GHz short-cavity VCSEL

Figure 4.6: Channel TF after 10-km (in blue), 24-km (in red), and 34-km (in yellow) SSMF propagation.

Optical source	α	κ
Tunable VCSEL	2.75	$8.3 \cdot 10^{12}$
Short-cavity VCSEL	3.7	$1.75 \cdot 10^{13}$

Table 4.2: Chirp parameters for a tunable VCSEL and a short-cavity VCSEL.

limited by κ, the transient chirp; the short-cavity device is impaired by a significant adiabatic chirp α as well, as evident by the limited intensity of the first frequency dip, almost disappearing for 24-km and 34-km SSMF channel TF. The good agreement of the theoretical curves with the experimental measurements guarantees a reliable estimation of VCSEL chirp parameters (reported in Table 4.2) for both the sources. The device design, based on a short-cavity technology, causes higher α and κ factors in short-cavity VCSEL. This laser is capable of achieving wide modulation bandwidths, but during DM a strong frequency chirp is induced, which limits its effectiveness in presence of network nodes with narrow channel bandwidth, as shown in the following paragraph.

4.2.2 Chirp interplay with tight optical filtering

When the transmission performance of DM-VCSELs is analyzed, the chirp plays a crucial role especially in presence of tight filtering of wavelength MUX and DEMUX inside WDM MANs. When COH-D is exploited, the chirp interplay with CD can be neglected, thanks to the CD DSP compensation. In the simulations, three different chirp conditions are analyzed, corresponding to the following three cases:

1. a DM VCSEL with chirp parameters as the short-cavity device;
2. a DM VCSEL with chirp parameters as the tunable device;
3. CW 500-kHz laser followed by an Electro-Absorption Modulator (EAM) with $\alpha = 0.4$.

For all the three sources, the modulation frequency bandwidth is fixed to 18 GHz, although only actual short-cavity VCSELs can achieve such a bandwidth. The VCSEL linewidth is 5 MHz, a reasonable value for both the lasers. The bias currents are set to 8 mA and 16 mA for case 1 and 2, respectively, while their modulation amplitudes are 8.5 mA and 26 mA respectively. The higher modulation depth can be exploited in the tunable VCSEL case thanks to a reduced amount of chirp, and this allows higher SNRs. The bias current and the modulation depth for case 3 are optimized to achieve an equivalent Extinction Ratio (ER) of 15 dB. The impact of optical filtering is evaluated again by using the TF of a 25-GHz channel spacing WSS [152]. The optical signal propagates through SSMF spans of either 35 km and or 65 km, with 0.25 dB/km attenuation and 17 ps/nm$\cdot$ km dispersion at 1550 nm. After each span EDFAs with 6-dB NF are exploited to compensate for the accumulated transmission losses.

The performance is evaluated by measuring the transmitted capacity in the case of DMT-modulated signals, considering both DSB and SSB DMT

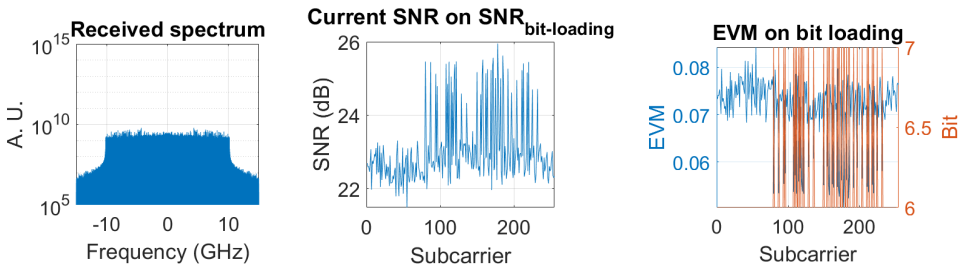

(a) Received spectrum **(b)** SNR after bit- and power-loading **(c)** Bit-loading and EVM

Figure 4.7: Tunable VCSEL results for DSB DMT 10-GHz modulation.

transmissions. The generated optical spectra have to occupy less than 25 GHz in order to be transmitted through cascaded WSSs, guaranteeing 25-GHz WDM spacing. For this reason, the DSB DMT signal, composed of 256 subcarriers, has 10 GHz bandwidth (corresponding to an optical bandwidth of around 20 GHz), leading to a subcarrier spacing of 39.062 MHz. On the other hand, the SSB transmission is performed by detuning the WSS of 9.5 GHz with respect to the carrier of a DMT signal, which is again composed of 256 subcarriers, but in a 20-GHz range, *i.e.*, the subcarrier spacing is doubled with respect to DSB modulation. In both cases a CP of about 2.1% of the symbol length is added.

The receiver DSP provides digital symbol synchronization, CP removal, subcarriers phase recovery, demodulation, and error count, together with CD compensation, as already discussed in Section 3.5. The transmitted capacity is evaluated performing Chow's bit loading algorithm [127] with a target BER of $3.8 \cdot 10^{-3}$ for single-channel, single-polarization transmission.

By comparing the received spectra in Figures 4.7(a) - 4.8(a), SSB has a higher spectral efficiency, because it exploits all the available VCSEL bandwidth and it occupies the entire 25-GHz channel bandwidth; on the other side it is more impaired by Signal-Signal Beating Interference (SSBI) [163] and by VCSEL and WSS bandwidth limitations. SSB modulation presents lower SNRs

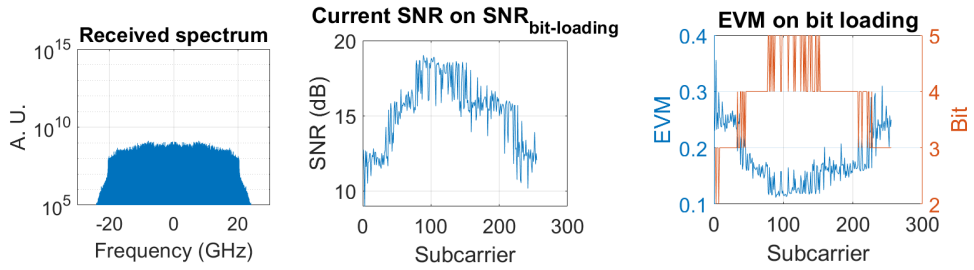

(a) Received spectrum **(b)** SNR after bit- and power-loading **(c)** Bit-loading and EVM

Figure 4.8: Tunable VCSEL results for SSB DMT 20-GHz modulation.

at low and high frequencies than at the central frequencies (Figure 4.8(b)): the first and last subcarriers can support modulation formats with lower bit/symbol (see Figure 4.8(c)). Contrarily, the estimated SNR in DSB modulation is flat over all the subcarriers (Figure 4.7(b)), supporting 64- and 128-QAM (see Figure 4.7(c)). On the other hand, the DSB signal occupies only half of the available E/O spectrum due to the 25-GHz optical spectrum constraint, and this limits the maximum achievable capacity.

Figure 4.9 depicts the capacities achieved for values of OSNR ranging between 30 dB and 40 dB in function of the number of crossed WSS in case of DSB DMT (Figure 4.9(a)) and SSB DMT (Figure 4.9(b)) of both the lasers for which the chirp conditions have been evaluated in Section 4.2.1. The transmission capacities have been measured in case of chirp typical of Electro-absorption Modulated Laser (EML) as well, *i.e.*, $\alpha = 0.4$, for DSB and SSB DMT modulations and they are represented in Figure 4.9(c) and (d) respectively, to analyze a case where the chirp parameters are much smaller than in DM sources. The tunable VCSEL (dashed curves) outperforms the short-cavity VCSEL (continuous curves), thanks to lower chirp parameters. This is blatant for DSB modulation, and it is corroborated by Figure 4.9(c), where the chirp of the EML is even lower. Conversely, this is less visible for SSB modulation, where only for a higher number of crossed WSSs the

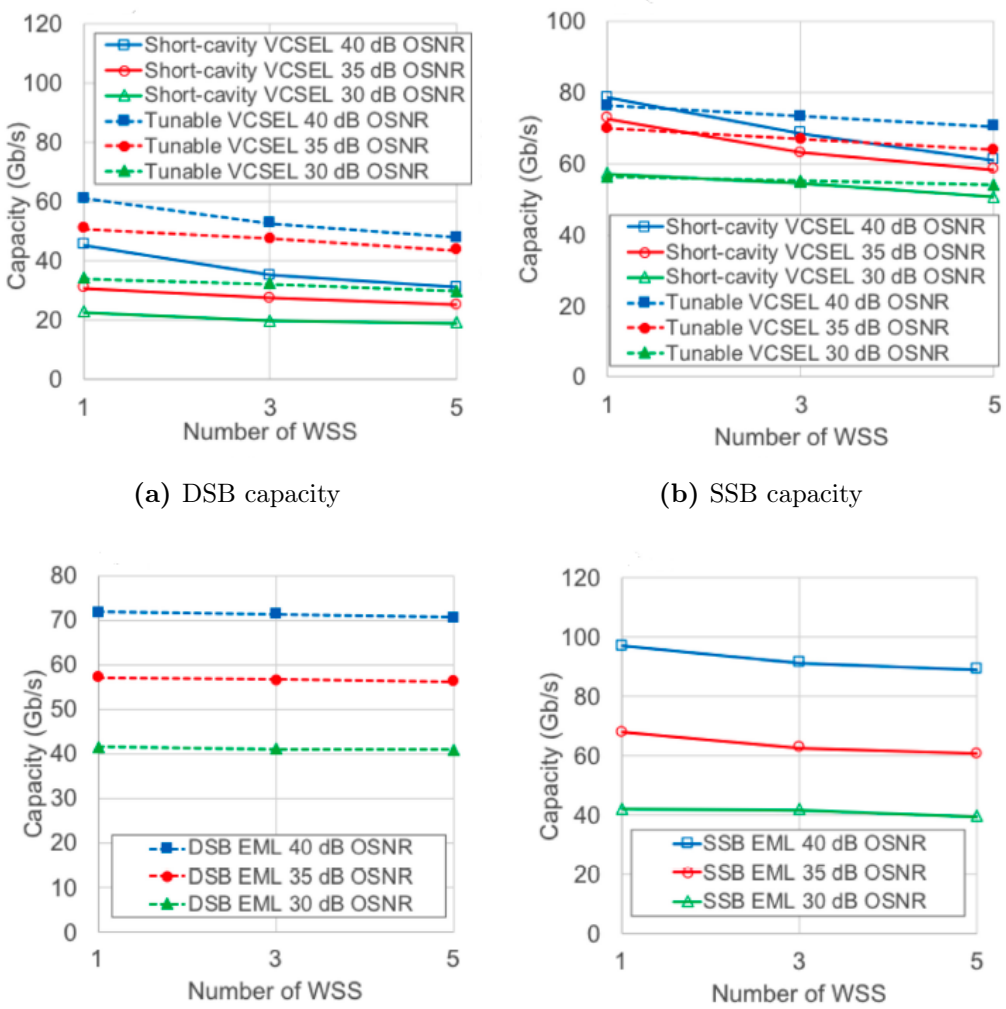

(a) DSB capacity

(b) SSB capacity

(c) DSB capacity

(d) SSB capacity

Figure 4.9: Capacities for OSNR ranging from 30 dB to 40 dB for two DM VCSELs ((a) and (b)) and a CW laser followed by an EML ((c) and (d)).

OSNR		40 dB	35 dB	30 dB
Short-cavity VCSEL	1 WSS (capacity)	45.5 Gb/s	30.9 Gb/s	22.8 Gb/s
	3 WSSs (capacity)	35.3 Gb/s	27.5 Gb/s	19.9 Gb/s
	5 WSSs (capacity)	31.1 Gb/s	25.2 Gb/s	19.2 Gb/s
Tunable VCSEL	1 WSS (capacity)	61.2 Gb/s	51 Gb/s	34 Gb/s
	3 WSSs (capacity)	52.6 Gb/s	47.8 Gb/s	32.4 Gb/s
	5 WSSs (capacity)	48 Gb/s	43.75 Gb/s	30 Gb/s

Table 4.3: SSMF reach and capacity for DSB modulation as a function of span length, VCSEL source, and number of crossed WSS.

OSNR		40 dB	35 dB	30 dB
Short-cavity VCSEL	1 WSS (capacity)	78.6 Gb/s	72.6 Gb/s	57.3 Gb/s
	3 WSSs (capacity)	68.6 Gb/s	63.1 Gb/s	54.5 Gb/s
	5 WSSs (capacity)	61 Gb/s	58.4 Gb/s	50.5 Gb/s
Tunable VCSEL	1 WSS (capacity)	76.2 Gb/s	70 Gb/s	56.2 Gb/s
	3 WSSs (capacity)	73.3 Gb/s	67 Gb/s	55 Gb/s
	5 WSSs (capacity)	70.4 Gb/s	63.8 Gb/s	54 Gb/s

Table 4.4: SSMF reach and capacity for SSB modulation as a function of span length, VCSEL source, and number of crossed WSS.

capacities transported in the short-cavity VCSEL case are significantly lower than in the tunable VCSEL scenario, *i.e.*, when the interaction between chirp and filtering is more detrimental. Furthermore, by comparing Figures 4.9(a) with (c) (and (b) with (d)) it can be noted that, for lower OSNR levels, the performance of the EML is worse than the capacities of both the VCSELs: a limited amount of chirp could be useful in noisier systems. A hypothesis to explain this phenomenon is that the aforementioned effect could be caused by the decrease of the Carrier to Signal Power Ratio (CSPR) in presence of chirp. CSPR has a strong impact on the capacity of DMT-modulated signals [164]; hence, its reduction due to chirp could mitigate the capacity decrease in the SSB condition.

Finally, Tables 4.3 and 4.4 recapitulate the transmitted capacities as a function of the span length and of the number of crossed WSS respectively for DSB and SSB DMT modulations for the VCSEL-based transmitters. The results are promising for the exploitation of VCSELs in S-BVTxs targeting around 50 Gb/s capacity per channel per polarization in presence of COH-D. In fact, especially for SSB DMT modulation also in presence of 5 WSS consecutive filterings, more than 50 Gb/s data rates can be targeted for OSNRs above 30 dB [165]. By looking at Table 4.1, this OSNR translates into bridging more than 250 km SSMF when using EDFAs with NF of 6 dB and span length of 65 km; with shorter span length, even longer transmission distances (up to 700 km for 35-km span length) can be supported, and this allows to cover wider MANs. However, DMT DSB performance is heavily impaired by chirp and its interplay with filtering, limiting the achievable capacities to below 50 Gb/s also for 100-km transmission ranges. It is worth noticing that the case of single WSS filtering is just for the purpose of evaluating the interplay between chirp and optical filtering, but it will not be further investigated in future except in case of a single HL3 node in Section 4.5, since it is analogous to neglecting the presence of a WSS filter performing SSB modulation at the

transmitter [161].

4.3 Multichannel transmission in 25-GHz grid

During propagation in the layered MAN introduced in Chapter 2.2, the WDM channels generated by the multi-Tb/s VCSEL-based S-BVT discussed in Chapter 2.1.1 are aggregated node by node filling up a 25-GHz WDM grid. In this section the impact of interchannel crosstalk on the system performance is discussed. The impairments introduced by interchannel crosstalk are evaluated in terms of transported capacity in presence of a channel under test at 1540 nm, and two adjacent channels at 1539.8 nm and 1540.2 nm, respectively. The optical channels are modulated with SSB DMT signals. It is mandatory to modulate the optical channels with SSB DMT signals, both for the fine granularity of the WDM channels and for the robustness of SSB to chirp demonstrated in Section 4.2. Two modulation bandwidths are taken into analysis: 16 GHz and 20 GHz.

The VCSEL bias current and the modulation amplitude are set to the optimal values of 8 mA and 8.5 mA respectively. When the DMT signal electrical occupation is limited to 16 GHz, the subcarrier spacing is 62.5 MHz, since the signal is composed of 256 subcarriers; on the other side a DMT signal occupation of 20 GHz corresponds to 78.125 MHz. In these conditions the performance of the transmitted channels is evaluated as a function of the number of WSS filters crossed along the MAN and for OSNRs ranging between 30 dB and 40 dB, in presence of coherent detection. The employed filter TF in the simulations is the one measured at the output of a programmable optical filter (Finisar WaveShaper 4000s) encoding the WSS theoretical transfer function of [152]. As previously stated, at least two WSSs are required, since one implements the SSB modulation at the transmitter side and one demodulates the channel under test at the receiver side. The propagation medium taken

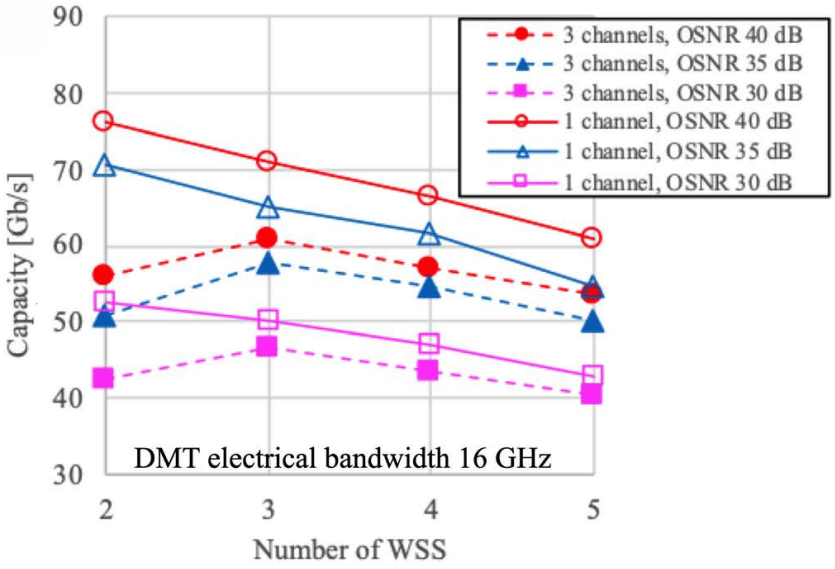

Figure 4.10: Transmitted capacity vs number of crossed Wavelength Selective Switch (WSS) for single-channel (continuous lines) and 3-channel propagation (dashed lines) 16-GHz SSB DMT signal for OSNR values of 40 dB, 35 dB, and 30 dB.

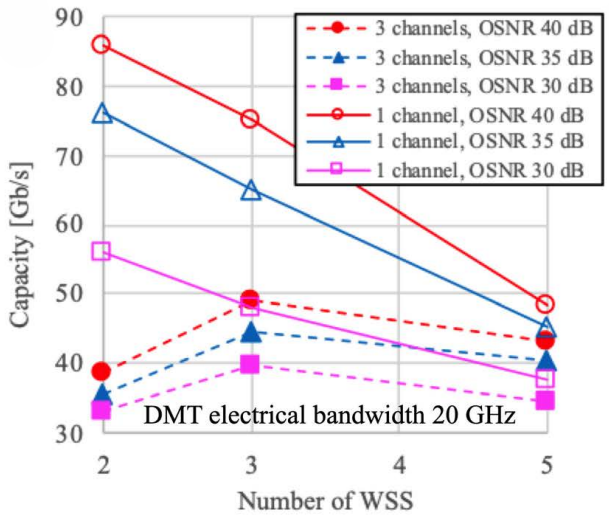

Figure 4.11: Transmitted capacity vs number of crossed WSS for single-channel (continuous lines) and 3-channel propagation (dashed lines) 20-GHz SSB DMT signal for OSNR values of 40 dB, 35 dB, and 30 dB.

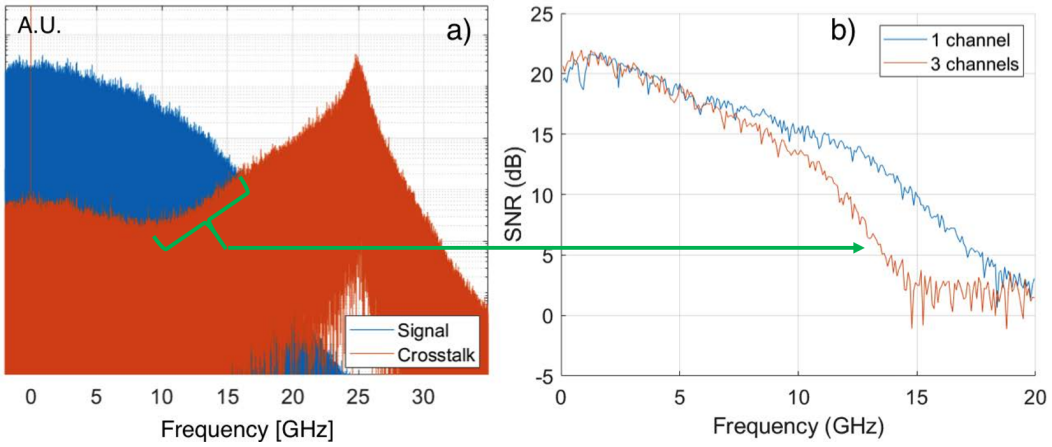

Figure 4.12: a) Crosstalk contrbution (in red) in the signal bandwidth (blue) and b) its effect of the measured SNR for 20-GHz SSB modulation.

into account is an SSMF, attenuating 0.25 dB per km and characterized by 17 ps/nm·km chromatic dispersion at 1550 nm. The transmission losses are compensated with EDFAs characterized by 6-dB NF.

Figures 4.10 - 4.11 show the dependence of the transmitted capacity on the number of crossed WSSs for OSNRs of 30 dB, 35 dB, and 40 dB for both 16-GHz and 20-GHz SSB DMT signal. In case of 16-GHz electrical occupation, already for single-channel propagation with an OSNR of 30 dB, 50-Gb/s capacity can be supported only for a single node crossing. With respect to the results for the short-cavity VCSEL in Table 4.4 for a single-channel transmission, the capacity is reduced because of the tighter signal bandwidth needed to limit the crosstalk. The presence of the interchannel crosstalk reduces the capacity in case of 2 WSS filtering of nearly 30% with respect to single channel propagation, whereas for a higher number of filters the reduction is less consistent: in fact, the impairment is caused by the presence of a residual component of the adjacent channel located on the higher frequency subcarriers, as it will be discussed more in detail in Section 4.5. It can be noticed that up to 5 WSS can be supported with capacities higher than 50-Gb/s per VCSEL with 25-GHz WDM adjacent channels for OSNR higher

than 35 dB, whereas the capacities are higher than 40 Gb/s for 30 dB OSNR. Indeed, in Section 4.2 it has been demonstrated that OSNR range needed to reach 50 Gb/s can guarantee more than 200-km reach with 35-km spans in the envisaged MAN topology [161].

On the other side, for 20-GHz operation the transported capacity in single-channel transmission is higher of a 10% up to 3 WSS filters with respect to the 16-GHz case for OSNR greater than 30 dB, but the trend more rapidly decreases when the number of crossed WSS increases. For 5 crossed WSS, the capacities are lower than the ones achievable for a 16-GHz DMT signal. This is due to the tight filtering introduced by the cascade of WSS filters, which lowers the SNR of the last subcarriers, and it causes them to be loaded with lower modulation formats. When the adjacent channels are added, their presence causes a reduction of the transmitted capacity of more than 40% for 2 crossed WSS. By comparing the capacity obtained for the two electrical signal bandwidths, the 20-GHz case sees its capacities reduced of 20% with respect to the 16-GHz modulation. This is due to a more significant crosstalk, which is pictorially represented with the red spectrum of Figure 4.12. Up to 7 GHz, the impact of interchannel crosstalk is negligible, but comparing the measured SNR for the single-channel propagation and the three-channel propagation a reduction is evident for 10 GHz on, and the reason is that the signal power (blue spectrum) decreases while the crosstalk due to the channel at 1540.2 nm increases. For more than 15 GHz, the crosstalk overcomes the signal, and so the SNR approaches to 0. In this region the subcarriers cannot provide any useful information, since they are too much impaired by crosstalk, and this reduces the transported capacity.

16-GHz electrical signal bandwidth has been proved to be the optimal trade-off between traffic carried by each channel and interchannel crosstalk: a further reduction on the signal bandwidth reduces the interchannel crosstalk, but the transported capacity per channel decreases in more significant terms,

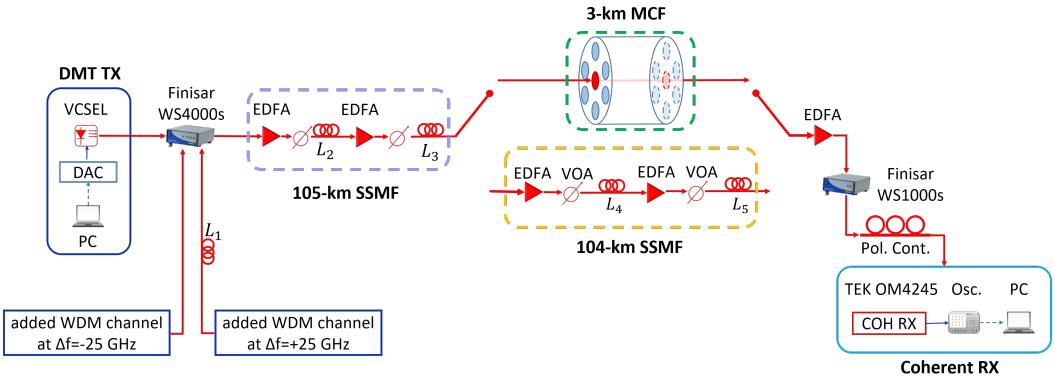

Figure 4.13: Setup for the evaluation of the transmitted capacity in presence of SSMF propagation.

leading to an overall worsening of the performance [166].

4.4 Impact of nonlinear propagation in multichannel transmission systems

The presence of three 25-GHz spaced high-capacity channels, which are DM with SSB DMT signals, along with multi-span transmission consisting of SSMF hundred-reach propagation and two HL3 filters for 25-GHz granularity is quantified in terms of transmitted capacity with the experimental setup shown in Figure 4.13. A VCSEL emitting at 1535 nm is DM with a DSB DMT signal composed of 256 subcarriers in 20-GHz bandwidth, with a CP of 2.1%. At the output of the first EDFA the power is set to +5 dBm. Two other channels at 25-GHz spacing are externally modulated with a DMT signal equivalent to the one modulating the central under-test channel, and generated by an independent DAC. In order to decorrelate the adjacent channels, an SSMF coil of $L_1 = 3$ km is employed. The two channels are aggregated with a Waveshaper emulating the TF of a 25-GHz WSS [152], which performs the SSB filtering of all the channels as well. The channels propagate along several SSMF spans. Three propagation lengths are taken into account: 104.5 km, 158 km,

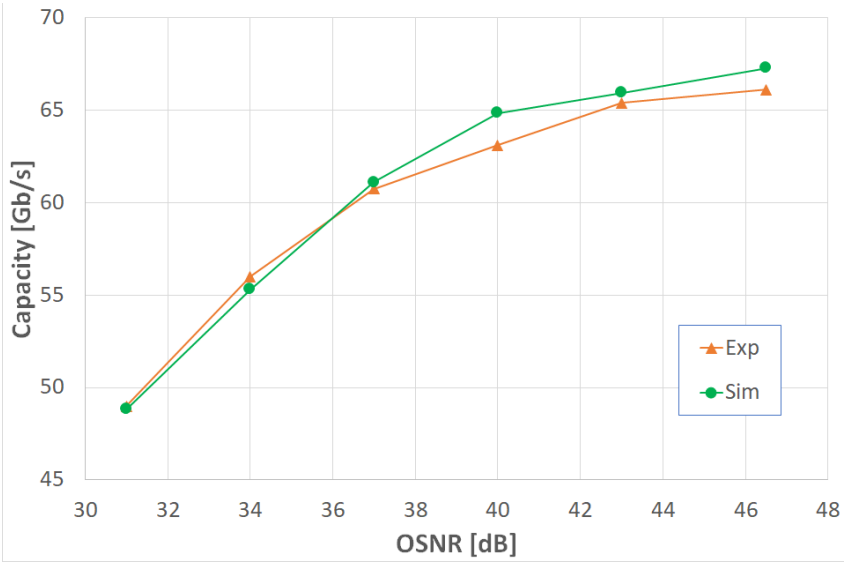

Figure 4.14: Capacity for BTB propagation and its validation via simulations.

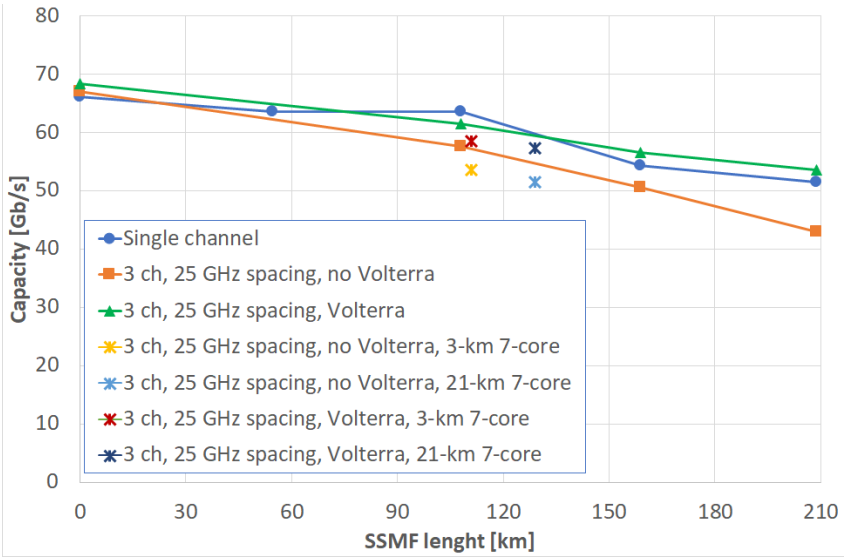

Figure 4.15: Capacity dependence on the propagation length for single and three-channel propagation.

and 208.9 km. Furthermore, another scenario provides the propagation along 2.9-km of 7-core MCF preceded by the aforementioned 104.5 km of SSMF. Two situations are analyzed: i) the three channels propagate through all the cores simultaneously; ii) the optical signal at the output of one core is sent through another core, for all the seven cores. In the last case, the signal propagates along 21 km of MCF and 104.5 km of SSMF. The launch power per span of the three channels is set to +5 dBm. Another Waveshaper emulates the TF of a DEMUX 25-GHz WSS [152]. The signal is then coherently received and acquired with a real-time oscilloscope with 8-bit vertical resolution, 100 GS/s and 33-GHz electrical bandwidth. Besides the operations described in Section 3.5, the distortions due to nonlinear multichannel propagation are mitigated with a 3^{rd} order Volterra equalizer [94].

In Figure 4.14 the dependence of the measured transmitted capacity for a target BER of $4.6 \cdot 10^{-3}$ on the OSNR for a single-channel propagation is represented with an orange line, along with the simulation results obtained in the same conditions. A good consistency of the simulations is achieved in every point, with a maximum deviation between the two curves of 2.7% at 40 dB. When the performance is dominated by the noise introduced by the components, the agreement allows to achieve very similar capacities, while for higher OSNR the simulations slightly overestimate the performance due to some other effects, such as the noise introduced by the receiver, which are not perfectly emulated. The accordance in the results presented both here and in Section 4.1 is encouraging to employ the simulator to investigate the system performance in contexts where it is difficult to set up experimental measurements, such as for the networks presented in Sections 4.5 and 4.6.

The BTB capacities of Figure 4.14 give an information on the impact of noise on the transmitted capacity. On the top of it, the nonlinear impairments further worsen the achievable capacity. The capacity is reduced by only 3 Gb/s when the OSNR is decreased from 46.5 dB to 40 dB, by 7 Gb/s for OSNR

lowering from 40 dB to 34 dB, and of other 7 Gb/s from 34 dB to 31 dB OSNR.

Figure 4.15 depicts the capacities for the previously introduced scenarios. In BTB the performances for single channel and three-channel transmission are comparable, also after the application of Volterra algorithm (an increase of 1 Gb/s is achieved in the transmitted capacity). These results are not in contrast to what explained in Section 4.3 about interchannel crosstalk, but the laboratory measurements have been performed in different conditions. First of all, in the experimental setup the adjacent channels are generated with externally modulated lasers, which, as stated in Section 4.2, suffer less chirp than the directly-modulated VCSELs employed in the simulations. Moreover, the modulators limit the bandwidth of the interfering channels, reducing their crosstalk. It is also worth noticing that the central VCSEL in the experimental setup is a different source than the simulated one, since it has different intrinsic and parasitic bandwidths. The positions in frequency of MUX and DEMUX are independently optimized, while the simulated ones are perfectly superimposed. Furthermore, the experimental results are subject to a variability which is more pronounced than in simulations (see the point at 110 km in Figure 4.15 which allows to carry the same capacity as at 54 km, despite the more nonlinear impairments accumulated during propagation and a slight reduction in the OSNR due to the presence of another fiber span). So, the results discussed in the previous paragraph are still valid for the previously simulated scenario, which is different, but not in contrast, from the experimental one described in this section. When the propagation distance is increased, the three-channel capacity encounters a reduction due to XPM and FWM accumulated during propagation up to 17% at 208 km with respect to single-channel at the same transmission length. The Volterra equalization algorithm allows to compensate for both XPM and SPM. In this way, the three-channel transmission outperforms the single-channel signal, leading to

an increase of the capacity of 4% with respect to the single-channel and of 24.5% with respect to the three-channel propagation without the application of the algorithm, for a transmission distance of 208.9 km. With the employment of Volterra equalization algorithm, the three-channel capacity is reduced by 22% at 208.9 km, in the face of a reduction of the 36% without applying it. In this way the target capacity of 50 Gb/s per polarization per channel can be achieved for more than 210 km distances and for three 25-GHz spaced channels.

The performance for three-channel transmission in presence of the MCF is lower than the one achieved neglecting its presence both with and without the application of the Volterra equalization algorithm. The employed MCF introduces a loss of 4 dB per core in its 3 km length. The nonlinear impairments, along with the ICXT and the coupling losses of the Fan-In Fan-Out devices, cause a reduction in the transmitted capacity, when all the channels simultaneously propagate in all the cores for the 3 km, of 4 Gb/s with respect to the corresponding values without the presence of the MCF. In the case when one core at a time is crossed, the Volterra algorithm compensates for some impairments, leading to an increase of 5 Gb/s of the capacity with respect to the simultaneous transmission and a loss of 3 Gb/s with respect to the correspondent capacity for three-channel propagation and the employment of Volterra algorithm. In this last case, an amplifier is employed to recover the signal power after four core crossings.

4.5 OSNR requirements for given target capacities in multi-hop transmission systems

The impact of HL4, HL3, and HL2/1 node crossing has been evaluated by single-polarization simulations in terms of OSNR to reach a target capacity (50 Gb/s, 40 Gb/s, and 25 Gb/s). At most 11 nodes are crossed, since from a

previous analysis [167] this choice covers the 90% of the cases for the MAN under study. Every possible combination of network nodes have been analyzed, considering that at least one HL3 node has to be crossed to properly select the desired channel. Seven channels are simulated, each one of them is generated by a 18-GHz VCSEL with $\alpha = 3.7$ and $\kappa = 1.526 \cdot 10^{13}$ chirp parameters and 0-dBm power. It is directly modulated with a 16-GHz DMT signal constituted of 256 subcarriers. Its bias current and modulation amplitude are 9 mA and 10 mA, respectively. The HL4 nodes are constituted of two 50-GHz spacing AWG flat-top, the HL3 and the HL2/1 nodes are composed of two 100-GHz bandwidth DEMUX/MUX and one WSS for 25-GHz channel spacing, as introduced in Section 3.4. For the sake of simplicity, since the nodes are designed in the same fashion, from now on the term "HL3 node" (or "HL3 level") will indicate both HL3 and HL2/1 nodes, no matter the actual hierarchical level. In every HL3 node but the first one (which adds the adjacent channels) and the last one (by which the desired channel is dropped) the signal recirculates, so it is crossed twice. The seven simulated channels are 25-GHz spaced, but at the HL4 node level the transmitted signal consists of three channels, which are 50-GHz spaced, and they are modulated with DSB DMT signals. At the first HL3 node, four other channels are added, shifted in frequency of $\pm$ 25 GHz with respect to the other three channels, so that at the output of the first HL3 the seven channels are 25-GHz spaced (Figure 4.16). In order to fit the 25-GHz grid, the seven channels crossing at least 1 HL3 node are properly filtered to be SSB DMT modulated. The signal propagates through spans of SSMF, neglecting the nonlinear effects. Then it is coherently detected with a COH-RX having a 25-GHz electrical bandwidth and exploiting a 10-dBm per polarization LO with 100-kHz linewidth. The DSP at the receiver provides for CD compensation and the other functionalities described in Section 3.5. Thanks to Chow's bit- and power loading algorithm [127], the transmitted capacity for a target BER of $3.8 \cdot 10^{-3}$ is computed.

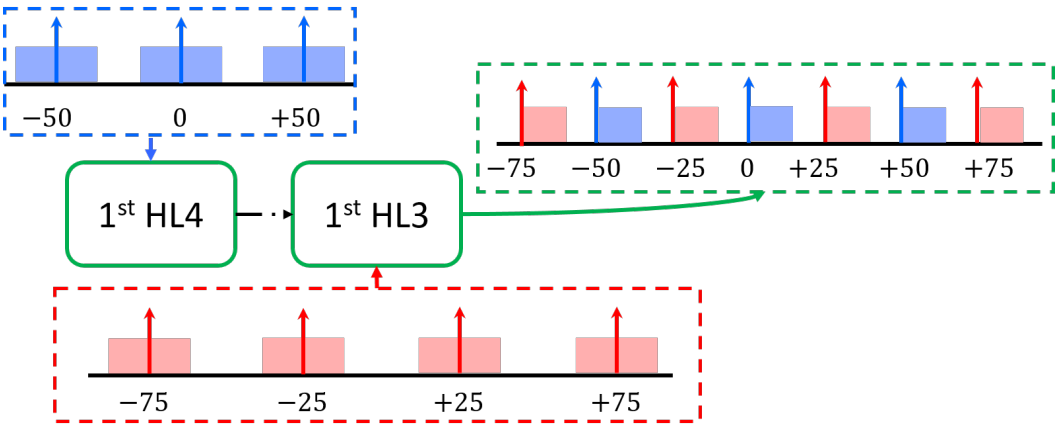

Figure 4.16: Representation of channel distribution. "0" represents the CUT, while the other numbers indicate the distance in frequency (in GHz) of the other channels with respect to the CUT.

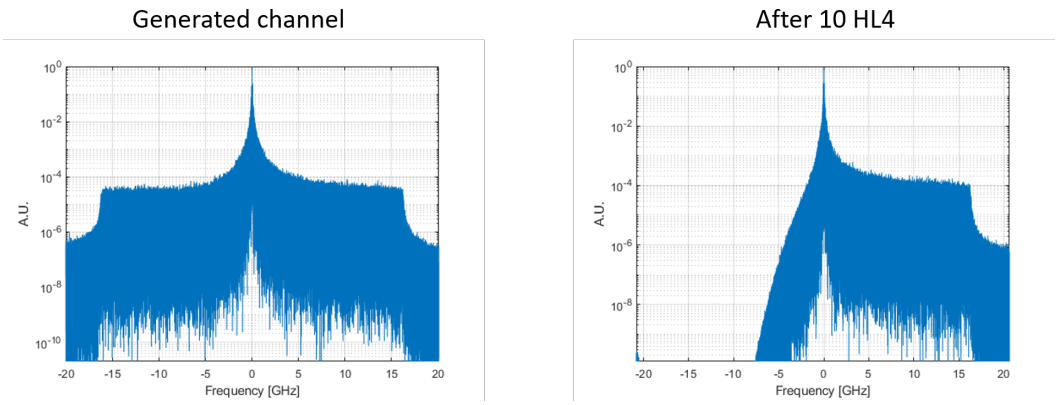

Figure 4.17: Comparison between the spectra of one generated channel and the same channel after crossing 10 HL4 nodes.

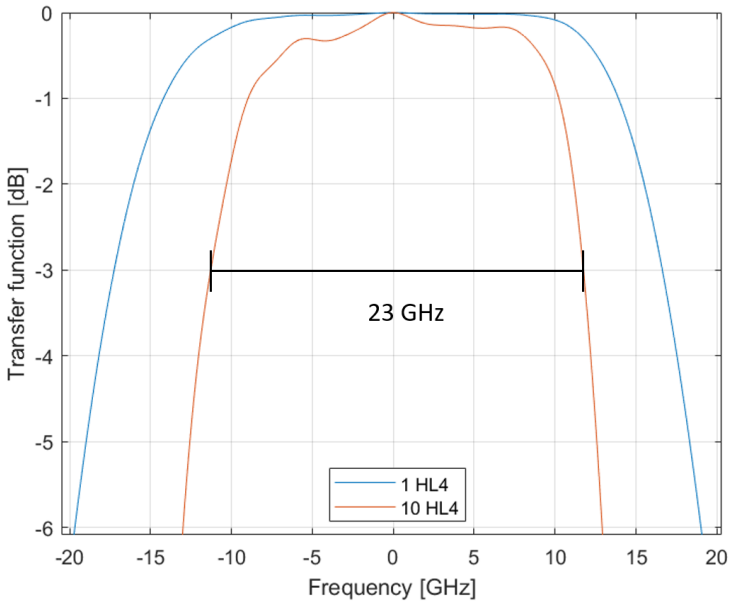

Figure 4.18: Comparison between the TFs of a single HL4 node and of 10 HL4 nodes.

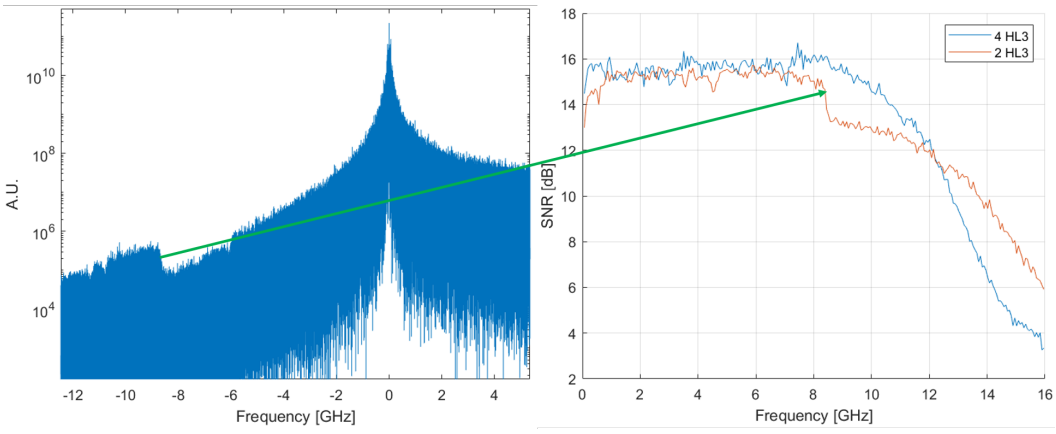

Figure 4.19: Spurious component from adjacent channel -25 GHz and its impact on the received SNR for a 50-Gb/s per channel transmission.

		HL3					
		1	**2**	**3**	**4**	**5**	**6**
HL4	**0**	32.4	35.6	34	35.1	36.2	38.4
	1	32.2	35.4	34	35	36	38.2
	2	32	35.4	34	35	36	38.2
	3	32	35.2	33.8	35	36	38.2
	4	32	35.2	33.8	34.8	35.8	38
	5	31.8	35	33.6	34.8	35.8	38
	6	31.8	35	33.6	34.6	35.7	
	7	31.8	34.8	33.5	34.6	35.5	
	8	31.6	34.8	33.5	34.3	35.1	37.8
	9	31.6	34.6	33.3	34.3		37.8
	10	31.5					

Table 4.5: Minimum OSNR (in dB) to reach a transmitted capacity of 50 Gb/s. The blue squares indicate a total number of nodes higher than 11. The light orange cells mark the cases, interesting for PASSION project, when the total number of nodes exceeds 11.

Tables 4.5, 4.6, and 4.7 report the required OSNRs for 50 Gb/s, 40 Gb/s, and 25 Gb/s capacity per channel respectively for several node topologies. By comparing the tables, it is quite straightforward to notice that, in order to achieve a lower target capacity, the constraint on the OSNR is looser. This is due to the adaptivity to the channel conditions provided by DMT modulation. A lower OSNR implies a higher level of noise, which can be tolerated by modulating the subcarriers with lower modulation formats that are more resistant to the noise. Lower modulation formats translate in a lower transmitted capacity. By reading each table, two trends can be identified: by increasing the number of HL4 nodes, the OSNR requisites lower, while by increasing the number of HL3 nodes, the OSNR has to increase to fulfill the

		HL3									
		1	**2**	**3**	**4**	**5**	**6**	**7**	**8**	**9**	**10**
HL4	**0**	28	31	29.7	30.5	31.4	32.2	33.3	35.2	37.2	46
	1	27.5	30.8	29.5	30.3	31.2	31.9	33	35	37	46
	2	27.3	30.6	29.3	30.3	31	31.7	32.8	34.8	37	
	3	27	30.4	29.1	30.1	30.8	31.5	32.8	34.7		
	4	26.8	30.1	29	30.1	30.8	31.5	32.6			
	5	26.6	29.9	28.8	29.9	30.6	31.2	32.4			
	6	26.4	29.7	28.8	29.7	30.6		32.4			
	7	26.3	29.5	28.7	29.7	30.6					
	8	26.3	29.2	28.7	29.7	30.6	31.2				
	9	26.1	28.8	28.7	29.7		31.2				
	10	26									

Table 4.6: Minimum OSNR (in dB) to reach a transmitted capacity of 40 Gb/s. The blue squares indicate a total number of nodes higher than 11. The light orange cells mark the cases, interesting for PASSION project, when the total number of nodes exceeds 11.

request in capacity. At a first glance, the first trend is quite counterintuitive. At HL3 level the filters have been simulated to perform SSB, so that their offset in frequency optimizes the suppression of one sideband. Even the TFs of the HL4 nodes are not centered on the channel, but they are translated in frequency to maximize the performance. This detachment causes one sideband to be progressively filtered out as the number of HL4 nodes increase. In fact, by increasing the number of HL4 nodes, the FWHM of the equivalent TF arising from the cascade of filters, decreases. From Figure 4.18 the reduction is evident: an HL4 introduces a 35-GHz bandwidth filtering, while for 10 of them the bandwidth decreases to 23 GHz, which is comparable to having another HL3 node in terms of filtering. In Figure 4.17 the comparison between the

		HL3									
		1	**2**	**3**	**4**	**5**	**6**	**7**	**8**	**9**	**10**
HL4	**0**	23.3	25.3	23.4	23.5	24.6	25.2	26	26.3	26.8	27
	1	22.5	24.8	23.1	23.4	24.2	24.8	25.5	25.8	26.3	26.5
	2	22.2	24.2	23	23.3	24	24.6	25.3	25.7	26.3	
	3	21.8	23.8	22.5	22.9	23.8	24.4	25.2	25.6		
	4	21.6	23.5	22.2	22.8	23.6	24.3	25			
	5	21.3	23.2	22	22.6	23.4	24.3	24.9			
	6	21	23	21.8	22.6	23.4		24.9			
	7	20.8	22.8	21.5	22.5	23.4					
	8	20.6	22.6	21.3	22.4	23.4	24.3				
	9	20.4	22.4	21	22.2		24.3				
	10	20.2									

Table 4.7: Minimum OSNR (in dB) to reach a transmitted capacity of 25 Gb/s. The blue squares indicate a total number of nodes higher than 11. The light orange cells mark the cases, interesting for PASSION project, when the total number of nodes exceeds 11.

spectra of a generated channel and after crossing 10 HL4 nodes is shown. It is visible the suppression of the left sideband, while the right sideband is left unchanged, and this leads to an increase of the performance. By reading the tables by row, *i.e.*, by increasing the number of HL3 nodes, the required OSNR increases. This is due to the tight filtering introduced by such nodes, which causes a reduction of the last subcarriers and a consequent requirement of a lower level of noise to achieve higher modulation formats in the remaining subcarriers. It is important to highlight that from 2 HL3 nodes on, moving to the next column implies that the signal is filtered by two more 25-GHz spacing WSS filters due to the recirculation. The presence of 2 HL3 nodes requires a higher OSNR. This is due to a spurious component of the adjacent

channel at -25 GHz with respect to the desired channel entering the signal bandwidth (as shown in Figure 4.19). This leads to a step in the SNR around -8.5 GHz, which causes lower modulation formats of the subcarriers at the frequencies in the range between 8 GHz and 12 GHz. This disturbance is completely suppressed in presence of 4 HL3 nodes or more. The SNRs in the two cases for 50 Gb/s required capacity show a different trend of the two topologies at 50 Gb/s: the SNR for 2 HL3 nodes crossing faces a reduction around 8 GHz, but then it lowers more slowly than in the case of 4 HL3 nodes, which is flat in the first 9 GHz, but then it has a steeper decrease in the last 7 GHz. These two situations are comparable in terms of required OSNR (35.6 dB for 2 HL3 nodes and 35.1 dB for 4 HL3). The same phenomenon does not happen in case of a single HL3 node, because in that case this node drops channels which are 50-GHz spaced, since no other HL3 node adds the adjacent 25-GHz spaced channels. The interchannel crosstalk for a 50-GHz granularity is much less relevant, so the required OSNR in this particular case has to be lowered to compensate for it. In case of 50 Gb/s target capacity, no more than 6 HL3 nodes can be crossed (so 2 HL3 nodes crossed once and 4 HL3 node crossed twice), since the filtering of the last subcarriers introduces a reduction of the capacity which cannot be coped even neglecting the presence of optical noise. The coloured cells in the table indicate that the number of crossed nodes exceeds 11 (some of the cases belonging to the remaining 10% of possible cases).

The presented OSNR values are valid for the *gross* transmitted capacity, *i.e.*, they consider the overheads and the FEC as well. For instance, in order to have a *net* target capacity of 50 Gb/s, the overall *gross* target capacity to achieve is 57 Gb/s (4% of alignment and training overheads, 2.1% of CP, and 7% of FEC have to be included). Table 4.8 summarize the required OSNR for the three *net* target capacities. A reduction of the number of possible use cases is evident (*e.g.*, the *net* 40 Gb/s can be achieved for no more than

HL4	HL3 1	2	3	4	5	6	7	8	9	10
0	33.5	39.2	37.8	39.6	47					
	30	33	32	32.7	33.6	35.1	38			
	23.6	25.6	24.2	24.7	26	26.8	28	28.2	28.6	29.1
1	33.3	39	37.8	39.6	47					
	29.8	32.8	31.8	32.5	33.4	34.9	37.6			
	23.1	25.1	23.8	24.5	25.9	26.6	27.8	28.1	28.5	28.8
2	33.1	39	37.7	39.6	47					
	29.6	32.6	31.6	32.5	33.2	34.7	37.4			
	22.8	24.7	23.5	24.2	25.7	26.4	27.7	27.9	28.3	
3	33.1	39	37.5	39.6	47					
	29.4	32.4	31.4	32.3	33	34.5	37.4			
	22.4	24.1	23	24	25.5	26.2	27.5	27.7		
4	33.1	38.8	37.4	39.4	46.9					
	29.2	32.2	31.3	32.3	33	34.5	37.2			
	22.2	23.9	22.7	23.8	25.3	26.1	27.3			
5	32.9	38.6	37.4	39.4	46.9					
	29	32	31.1	32.1	32.8	34.2	37			
	21.9	23.6	22.5	23.6	25.2	26	27.1			
6	32.9	38.6	37.3	39.2	46.8					
	28.8	31.8	31.1	31.9	32.8		37			
	21.6	23.4	22.3	23.6	25		27.1			
7	32.9	38.4	37.1	39.2	46.8					
	28.7	31.6	31	31.9	32.8					
	21.4	23.2	22.1	23.5	24.8					
8	32.8	38.2	37.1	39	46.8					
	28.7	31.6	31	31.9	32.8	34.2				
	21.2	23	21.9	23.4	24.8	26				
9	32.8	38.2	37	39						
	28.5	31.5	31	31.9		34.2				
	21	22.8	21.8	23.2		26				
10	32.7									
	28.4									
	20.2									

Table 4.8: OSNR minimum threshold (in dB) to get a transmitted net capacity of 50 Gb/s (green), 40 Gb/s (yellow), and 25 Gb/s (pink) as a function of the number of crossed HL4 and HL3 nodes. The blue squares indicate a total number of nodes higher than 11. The grey cells mark the impossibility of reaching such a target capacity. The darker cells pinpoint the MAN path cases with more than 11 hops.

7 HL3 node crossings, while with the *gross* 40 Gb/s 10 HL3 nodes can be reached). It is worth underlining that the discussed OSNRs for both *gross* and *net* target capacities constitute the lower bound when fiber nonlinear effects are neglected. With the introduction of nonlinear impairments, the tabulated values are not sufficient to fulfill the requests. For this reason, it is important to take a margin on the target capacity depending on the desired reach. For example, in the following section it will be highlighted that the introduction of nonlinear impairments causes a reduction of 6% of the capacity for 170-km propagation and on average of the 10% for 236 km. By reverting these results, in order to target 170 km, the minimum OSNRs for a target capacity will be computed by increasing this capacity of 6% in linear propagation.

4.6 Hundred-km MAN networks: two cases

Two different network topologies are here taken into consideration, namely "case study A" (Figure 4.20) and "case study B" (Figure 4.21). The analyses have been performed for a single polarization, direct modulation of the 16-GHz SSB DMT channels, and COH-D. The VCSEL parameters, the node architecture, and the channel spacings are the same as in the previous section. The only difference is that even the three 50-GHz spacing channels at HL4 level are modulated with an SSB DMT electrical signal. The signal propagates along SSMF fiber spans with attenuation coefficient of 0.25 dB/km, 17 ps/nm·km chromatic dispersion at 1550 nm and impaired by GVD, SPM, XPM, and FWM. EDFAs with a NF of 7 dB are employed to compensate for the transmission losses. For both the case studies several different scenarios have been hypothesised. In a scenario the amplifiers have been put after each span, while in the other(s) some spans have been rearranged considering a distance between two adjacent amplifiers around 35 km, where possible. Again the signal is coherently detected, with the same receiver and DSP algorithms as

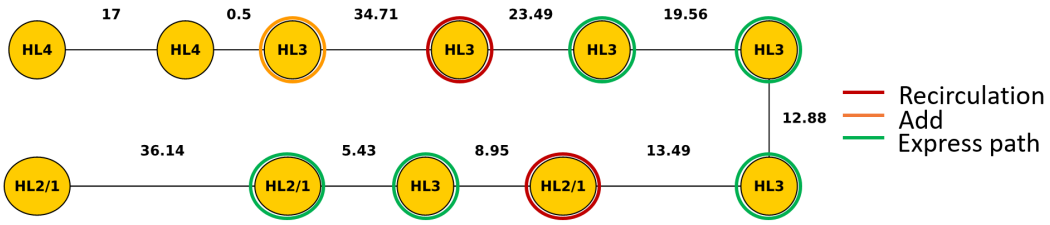

Figure 4.20: Topology of "case study A" with an overall transmission distance of 172.15 km.

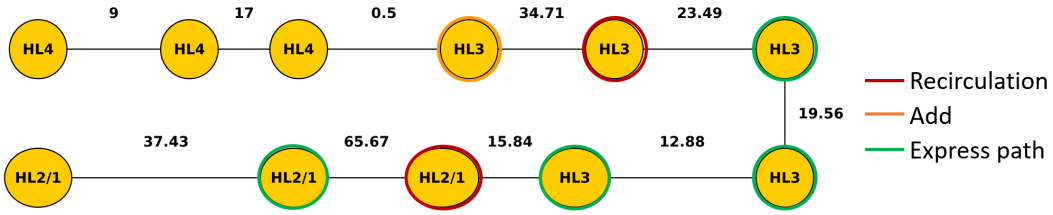

Figure 4.21: Topology of "case study B" with an overall transmission distance of 236.08 km.

the ones in the previous section. The performance is evaluated in terms of transmitted capacity for a target BER of $3.8 \cdot 10^{-3}$ [127].

The network topology for "case study A" is shown in Figure 4.20. The first HL4 node provides the multiplexing of the three 50-GHz spaced channels, along with the SSB transmission. The first HL3 node adds the adjacent 4 channels, and in the third HL3 node the signal recirculates. The other HL3 nodes are in express path configuration. In the first HL2/1 node the signal recirculates, while the second one is in express path as well. The last HL2/1 node demultiplies the signal, selecting the desired channel. The optimal optical launch power has been identified to be 1 dBm. Two different scenarios have been studied: in the first scenario the amplifiers have been placed after each span but 0.5 km, and in the other some spans have been aggregated. The aggregation of the spans has been achieved by considering 19.56 km and 12.88 km as a single span, and 13.49 km, 8.95 km, and 5.43 km as another single span. By comparing the graphs in Figure 4.22 (and the corresponding Tables 4.9(a)

and (b)) the capacity increases when some of the spans are aggregated, despise having a comparable value of OSNR. This is due to a reduction in the average carried power, which limits the impact of the nonlinear effects with a reasonable attenuation of the signal. The reduction due to the nonlinear effects is around 6% with respect to the propagation in linear regime (around 54.2 Gb/s).

The function of the nodes in "case study B" is the same as for "case study A" (Figure 4.21). Four different simulation scenarios have been classified: on the top of the choice of aggregating shorter spans or not, another couple of scenarios can be identified depending on whether in the 65-km span one amplifier or two have to be placed. Figure 4.23 and Tables 4.10(a)-(b) and 4.11(a)-(b) summarize the results of the four simulations. The optimal optical power is again 1 dBm for every topology. A more significant increase (2.6 Gb/s) of the transmitted capacity arises when the 65-km span is split in two separate spans (35 km and 30.67 km). This is due to both an increase in the OSNR of 2 dB and to a higher power at the output of the cascade of the two spans, which on one side increases the nonlinear effects, but it is less detrimental than a significant signal attenuation (16.4 dB) . By comparing the two scenarios in linear regime, the increase in the OSNR translates in an increase of 1.3 Gb/s in the corresponding transmitted capacity. The nonlinear effects lead to a reduction of the transmitted capacity of 11% in case of 65-km span, and of 8.5% when the span is divided. When the shorter spans are aggregated (9 km and 17 km as a span, 23.49 km and 19.56 km as another single span, and 12.88 km, and 15.84 km as a further single span), the OSNR and the transmitted capacities are comparable to the case of amplifiers installed at each node. A better performance is achieved in "case study A", because the signal propagates for a lower distance, the number of active nodes being the same. "Case study B" cannot target 50 Gb/s per channel in the network configurations presented in this section; however it cannot be excluded that some other configurations could allow to reach such a capacity.

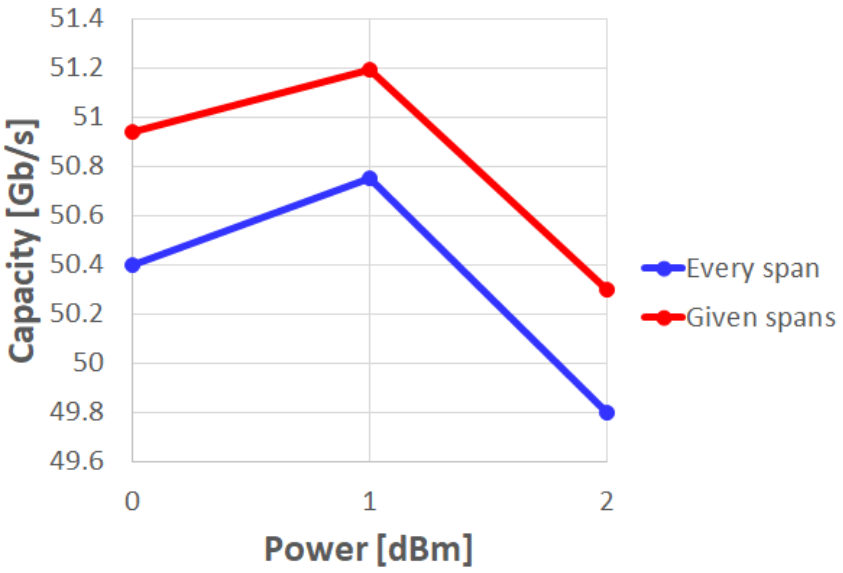

Figure 4.22: Transmitted capacities of "case study A" for two EDFA distributions.

(a) Every span

Input power [dBm]	OSNR [dB]	Capacity [Gb/s]
0	37.01	50.4
1	38.01	50.75
2	39.01	49.8

(b) Given span

Input power [dBm]	OSNR [dB]	Capacity [Gb/s]
0	37.19	50.9
1	38.19	51.19
2	39.19	50.3

Table 4.9: Achievable capacities in "case study A" for different launch powers.

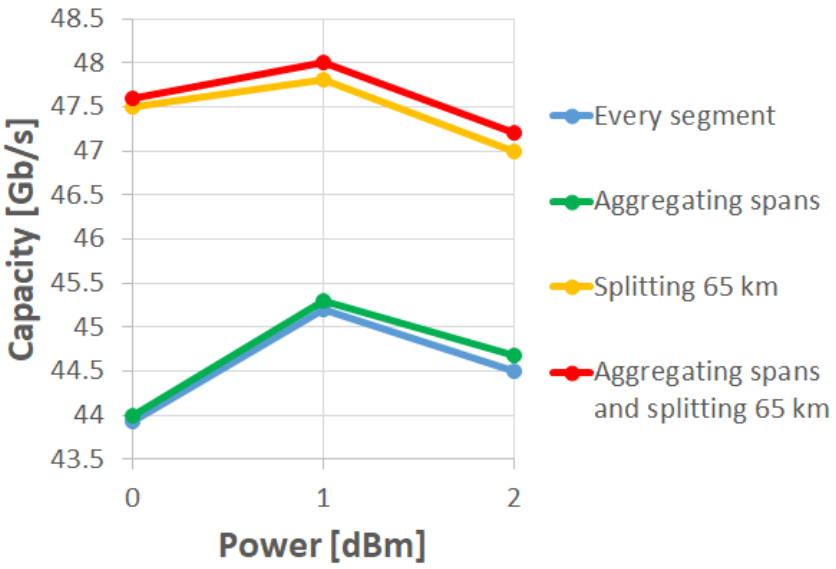

Figure 4.23: Transmitted capacities of "case study B" for four EDFA distributions.

(a) Every span

Input power [dBm]	OSNR [dB]	Capacity [Gb/s]
0	34.45	43.9
1	35.45	45.2
2	36.45	44.5

(b) Given span

Input power [dBm]	OSNR [dB]	Capacity [Gb/s]
0	34.32	44
1	35.32	45.3
2	36.32	44.68

Table 4.10: Capacities in "case study B" for different launch powers.

(a) Every span

Input power [dBm]	OSNR [dB]	Capacity [Gb/s]
0	36.32	47.5
1	37.32	47.8
2	38.32	47

(b) Given span

Input power [dBm]	OSNR [dB]	Capacity [Gb/s]
0	36.12	47.6
1	37.12	48
2	38.12	47.2

Table 4.11: Achievable capacities in "case study B" for different launch powers and splitting the 65-km span.

Chapter 5

Impact of Semiconductor Optical Amplifiers in MAN network node crossing

As previously introduced, MAN networks are composed of network nodes characterized by Semiconductor Optical Amplifier (SOA)-based Wavelength Blockers (WBLs). In this chapter the impact of SOAs on the transmission performances is evaluated. Firstly, these amplifiers are introduced with a very brief presentation of the nonlinear impairments introduced by the SOAs and some possible applications. The rate equations describing the transient behaviour of the SOA are presented and a model to numerically solve them is described. It is accurate, but it implies a complete knowledge of the device and a heavy computational complexity. The employed SOA is characterized in terms of CW gain and transfer function. This characterization is preparatory to the discussion of the application of SOAs as WBLs. The amplifier impact is evaluated for several SOA bias currents and input powers, for both DSB and SSB DMT signal modulating externally and directly a DFB laser and a VCSEL respectively. At last, the transmitted capacity of a multi-hop network constituted of a complete HL4 node and hundred-km SSMF propagation is

experimentally measured, where the nonlinear impairments introduced in the propagation are mitigated with the 3rd order Volterra algorithm.

5.1 Introduction to SOAs

A Semiconductor Optical Amplifier (SOA) is an optical amplifier based on a semiconductor gain medium. It is based on the same working principle as the laser, where at the end of the active region anti-reflection coatings replace the laser mirrors. They guarantee very low reflectivity (in the range $[10^{-4} - 10^{-3}]$ [168]), which prevents ripples to appear in the gain spectrum [169]. Furthermore, higher reflectivities increase the NF, since they cause a reduction in the carrier density, in the saturation power at the output, and in the gain bandwidth [170], [171]. The incoming light is coupled into a semiconductor single-mode waveguide, the length and the transverse dimension of which are generally in the ranges [200 μm - 2 mm] and [1 μm - 2μm] respectively. The length of the active region plays a crucial role in the SOA operation, as it will be briefly discussed later in this chapter. The active region is pumped with an electric current, which induces the inversion of free carrier population and generates the optical gain. In this way the incoming signal is amplified in the propagation along the amplifying medium and it exits from the opposite facet of the chip. When the photons energy is slightly higher than the band gap energy, the gain reaches its maximum value.

Some physical effects the amplified signal is subject to are:

- optical gain;
- Amplified Spontaneous Emission (ASE): it is the spontaneous emission of photons amplified in the active medium;
- Self-Phase Modulation (SPM): the output signal phase is modulated by the refractive index changes induced by the power variations of the

signal;

- Cross-Phase Modulation (XPM): the refractive index changes induce the phase of one signal to be affected by the power variation of all the other propagating signals;
- Four-Wave Mixing (FWM): the beating of two or more propagating signals generates beams at other frequencies;
- Self-Gain Modulation (SGM): analogously to SPM, it is the modulation of gain due to the variation of the signal power;
- Cross-Gain Modulation (XGM): it is the modulation of gain of one signal which is affected by all the other signals amplified by the SOA;
- Polarization rotation: the variation of the input signal power causes a rotation of the SOP of the signal at the output of the SOA due to birefringence effects.

SPM, XPM, and FWM are the same phenomena as the ones discussed in Chapter 3.2 for fiber propagation.

An SOA can be employed for several applications in an optical communication system [172]. Some of them are here mentioned. It can function as a booster amplifier to increase the transmitted power for medium-haul links consisting of an optical fiber between a transmitter and a receiver without the exploitation of active components. As shown in Chapter 2.2, SOAs can be used as booster amplifiers before the signal crosses a network node as well. Furthermore SOAs used as booster amplifiers are needed in case of WDM transmission, to concurrently amplify several optical signals at different wavelengths. SOAs can be employed as optical preamplifiers to enhance the signal power level before detection in order to increase the receiver sensitivity in case of long links without stages of amplification. In-line SOA amplifiers regenerate the signal power by compensating the transmission losses. They are advantageous for

their bidirectionality (on the contrary, EDFAs are unidirectional components), their low power consumption and compactness (these features are decisive for the employment of SOAs in MAN nodes as well), and WDM capability, as previously mentioned. Nonlinear effects can be used to perform several functionalities. An example is XGM, which allows to convert the wavelength of a weak CW signal when it is injected in a SOA along with a strong pump light. The SOA imposes the pump modulation on the probe, and so it works as a wavelength converter. Due to their reduced switching time (in the order of 100 ps) [173], SOAs can be employed to build gate arrays as optical switches by simply turning on/off their bias current. SOAs can function as Add/Drop Multiplexers (ADMs) to separate a specific wavelength from the others and leaving it unperturbed by interference arising from adjacent channels. In the MAN nodes taken into account in this thesis, the SOAs are used as wavelength blockers, by properly tuning each component to let some wavelengths cross the node and others be dropped.

An issue in the deployment of SOAs in an optical network is the coupling with the optical fibers. Considering that the cross-section of the SOA waveguide is in the order of 1 μm^2 and that the core radius of a SSMF is about 9 μm, the cross-section of a SSMF is about 80 times larger than the SOA one. This induces the necessity to couple the mode profiles of the two optical devices, in order to prevent the NF from increasing [174]. Tapers are then needed to match the mode profiles and they can be integrated either on the fiber [175] or in the SOA waveguide [176].

SOAs are flexible components, the gain peak wavelength can be tuned by properly choosing the material composition of the active layer. Moreover, they can be integrated with other active or passive optical components, and they are cheap: these are some of the reasons why SOAs are employed in the development of future MAN nodes.

5.2 Amplified Spontaneous Emission (ASE) and gain dependence on the active region length

One of the key parameters is the free carrier density inside the active region, which depends on the active region length. As it is quite straightforward, the longer is the active region, the smaller is the free carrier density in a given position, the cross section and the bias current being the same. Besides its level, two other aspects of the free carrier density are relevant: its spectral distribution and its spatial distribution along the SOA. The spatial distribution is mainly influenced by the ASE of the SOA. Forward and backward ASE components travel across the active region and they are amplified when propagating towards the facets. This causes the carrier consumption due to stimulated emission to be more consistent near the SOA facets than in the middle of the device. The photons of the incoming optical signal affect the free carrier density distribution as well. The enhancement of the input power diminishes the average free carrier density, but with different trends depending on the position along the SOA. At the output facet the free carrier density decreases with the increase of the optical power. At the input facet of the device the free carrier density increases with the signal power. In fact the reduction of free carrier density along the length of the SOA active region causes a decrease in the spontaneous emission of photons, which are then coupled in the backwards direction. This reduces the backward travelling ASE component and the stimulated recombination rate, causing an increase of the free carrier density [177], [178].

ASE combines spontaneous and stimulated emissions. The large carrier density in the conduction band causes the spontaneous emission to generate many photons, a portion of which is amplified after being coupled to the fundamental mode of the active guide. The large width of the ASE optical spectrum is caused by the spontaneous emission component, while its high intensity is induced by the stimulated emission. For more details, refer to [177].

As already introduced in Chapter 3.3 for EDFAs, the ASE is detrimental for the system performance in presence of SOAs, since it introduces noise which deteriorates the SNR of the amplified signal. Another effect of ASE is the depletion of carriers, which reduces the maximum small signal gain. This impacts on both the unsaturated gain and the CW gain, as it will be discussed in Section 5.4, modifying the functioning of the device.

The most important parameter of an optical amplifier is its gain, so it is worth a brief discussion about it. For high levels of input power the gain of an amplifier saturates, so it decreases when the signal power increases. The maximum achievable gain is the so-called *small signal gain* G_0, because it is the amplifier gain for a reduced value of the input power. The ASE saturation impacts on the value of G_0, which increases for longer SOA active regions [179].

The gain remains quite constant to G_0 for low input powers. When the power increases, a significant carrier depletion occurs and this causes the gain to decrease. The input power for which the gain is $G_{3dB} = G_0/2$ (so it is reduced by 3 dB) is the input saturation power P_{in-sat}, which corresponds to the output saturation power $P_{out-sat} = G_{3dB} \cdot P_{in-sat}$. Conventionally $P_{out-sat}$ is identified as the upper limit of the SOA linear operation. Figure 5.1 shows the characterization of the SOA employed in this thesis. The SOA in analysis is a polarization-insensitive 500-μm Optospeed 1550MRI/P device. The gain increases with the imposed bias current, and it saturates for high current densities. This phenomenon is related to the average carrier density in the active region. The pump rate proportionally increases with the bias current, but more slowly with respect to the total carrier recombination. This causes the gain to saturate. Table 5.1 summarizes the values of P_{in-sat} and $P_{out-sat}$ for bias currents in the range between 100 mA and 225 mA. For currents higher than 200 mA, the SOA saturates for the approximately same value of $P_{in-sat} \approx -9.2$ dBm. In fact, by comparing the trend of G_{CW} at 200 mA and at 250 mA, the CW gain at 200 mA is 1 dB less than the one achievable

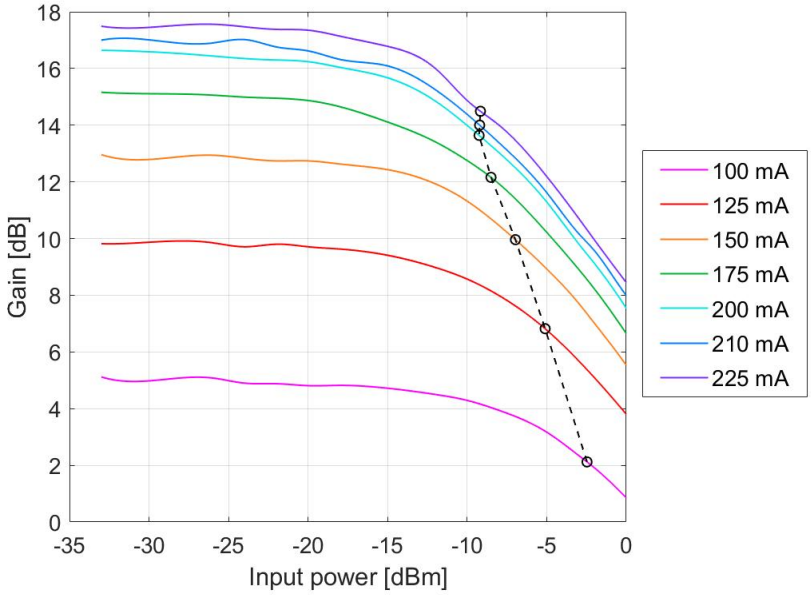

Figure 5.1: Dependence of the CW gain on the bias currents. In black, the trend of P_{in-sat}.

Bias current	G_{3dB} [dB]	$P_{in\text{-}sat}$ [dBm]	$P_{out\text{-}sat}$ [dBm]
100 mA	2.12	−2.47	−0.35
125 mA	6.28	−5.1	1.72
150 mA	9.96	−6.97	3
175 mA	12.16	−8.5	3.66
200 mA	13.64	−9.25	4.39
210 mA	14	−9.22	4.78
225 mA	14.49	−9.17	5.32

Table 5.1: Dependence of input and output saturation powers on the SOA bias currents.

at 250 mA for every bias current taken into account. When the bias current decreases, the SOA saturates for higher powers, but the more is the reduction of the bias current, the more the gain lowers as well. The gap between currents at 25 mA of distance increases with the reduction of the current itself, with less than 1 dB between 200 mA and 225 mA and 5 dB between G_0 at 100 mA and at 125 mA (3 dB for G_{CW}).

This discussion is valid when the steady-state condition is reached, *i.e.*, in CW. The temporal evolution of the gain is interesting to introduce to better understand the behaviour of the SOA. The following paragraph presents a mathematical model of the SOA working function.

5.3 SOA mathematical model

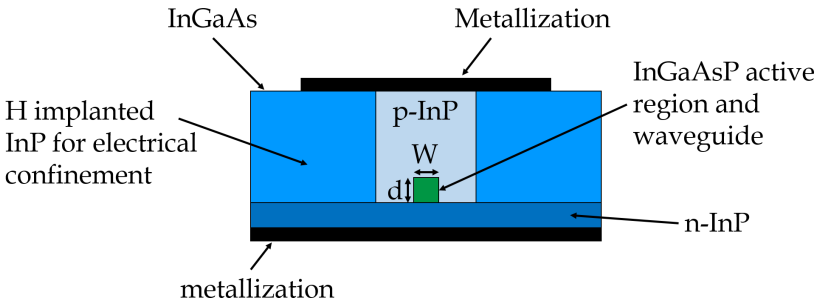

Figure 5.2: Schematic of the SOA modelled by Connelly [180].

The model here presented has been proposed by Michael Connelly [180], and takes into account a 1.55-μm InP − $In_{1-x}GaxAs_yP_{1-y}$ homogeneous buried ridge stripe device [181] (see Figure 5.2). The central active region is of length L_c, width W, thickness d, and its refractive index is n_m. It is a tapered device on both ends, and the length of the taper is L_t. The tapers reduce the confinement factor from the maximum value Γ at the center of the waveguide to zero at each end. So an equivalent SOA with the same geometrical and

optical characteristics as the active region and with a length L

$$L = L_c + L_t \tag{5.1}$$

can be used as a model of the actual device. The active region has a material gain coefficient g_m at frequency ν

$$\begin{aligned} g_m(\nu, n) = \frac{c^2}{4\sqrt{2\pi^3} n_m^2 \tau \nu^2} \left(\frac{2 m_e m_{hh}}{\hbar \left(m_e + m_{hh} \right)} \right)^{3/2} \times \\ \times \int_0^\infty \sqrt{\nu' - \frac{E_g(n)}{h}} (f_c(\nu') - f_v(\nu')) \times \\ \times \left(\frac{2 T_0}{(1 + (2\pi T_0)^2 (\nu' - \nu)^2} \right) d\nu'. \end{aligned} \tag{5.2}$$

n is the electron density in the conduction band, τ is the radiative carrier recombination lifetime, $\hbar = h/2\pi$ is the reduced Planck's constant, m_e and m_{hh} are the conduction band electron and hole effective masses, and T_0 is the mean lifetime of the electrons to coherently interact with a monochromatic field. The bandgap energy $E_g(n) = E_{g0} - \Delta E_g(n)$ is the sum of two contributions: the bandgap energy without the injection of carriers E_{g0} and the bandgap shrinkage due to the injection of carriers $\Delta E_g(n)$. The two Fermi-Dirac distributions in the conduction and valence bands [182] can be expressed as a function of the quasi-Fermi levels E_{fc} (referred to the bottom of the conduction band) and E_{fv} (relative to the top of the valence band) and the absolute temperature T:

$$\begin{aligned} f_c(\nu) = \frac{1}{\exp\left(\frac{E_1 - E_{fc}}{kT} \right) + 1} \\ f_v(\nu) = \frac{1}{\exp\left(\frac{E_2 - E_{fv}}{kT} \right) + 1}, \end{aligned} \tag{5.3}$$

where the energies E_1 and E_2 depend on both m_e and m_{hh} as

$$\begin{aligned} E_1 = (h\nu - E_g(n)) \frac{m_{hh}}{m_e + m_{hh}} \\ E_2 = -(h\nu - E_g(n)) \frac{m_e}{m_e + m_{hh}}. \end{aligned} \tag{5.4}$$

By properly approximating the values of E_{fc} and E_{fv} [183], Eq. (5.2) can be rewritten as

$$g_m(\nu, n) = \frac{c^2}{4\sqrt{2\pi^3} n_m^2 \tau \nu^2} \left(\frac{2 m_e m_{hh}}{\hbar (m_e + m_{hh})} \right)^{3/2} \times \sqrt{\nu' - \frac{E_g(n)}{h}} (f_c(\nu) - f_v(\nu)), \tag{5.5}$$

where a gain coefficient g'_m and an absorption coefficient g''_m

$$g'_m = \frac{c^2}{4\sqrt{2\pi^3} n_m^2 \tau \nu^2} \left(\frac{2 m_e m_{hh}}{\hbar (m_e + m_{hh})} \right)^{3/2} \times \sqrt{\nu' - \frac{E_g(n)}{h}} f_c(\nu)(1 - f_v(\nu)), \tag{5.6}$$

$$g''_m = \frac{c^2}{4\sqrt{2\pi^3} n_m^2 \tau \nu^2} \left(\frac{2 m_e m_{hh}}{\hbar (m_e + m_{hh})} \right)^{3/2} \times \sqrt{\nu' - \frac{E_g(n)}{h}} f_v(\nu)(1 - f_c(\nu)) \tag{5.7}$$

can be identified.

The material loss coefficient α is a linear function of the carrier density n:

$$\alpha(n) = K_0 + \Gamma K_1 n. \tag{5.8}$$

K_0 is the intrinsic material loss (carrier-independent) and K_1 is the intervalence band absorption (carrier-dependent).

The SOA model here characterized focuses on the interaction between the carrier density and the photon rates, which is described by coupled differential equations. The transverse variations in the carrier density and in the photon rates can be assumed to be negligible. The power reflectivities of the input and output facets are R_L and R_R, respectively, where L stands for *left* and R for *right*. Analogously, the amplitude reflectivity coefficients are $r_L = \sqrt{R_L}$ and $r_R = \sqrt{R_R}$. In this discussion a single signal is supposed to travel across the SOA. Its field can be decomposed in two counter-propagating travelling-waves, $E^+(z)$ in the positive z direction and $E^-(z)$ in the negative z direction. By definition, the axis z lies on the amplifier axis and its origin corresponds to the input facet. The photon rate of a travelling-wave can be expressed as the squared modulus of the amplitude of the wave itself:

$$\begin{aligned} N^+ &= \left| E^+(z) \right|^2; \\ N^- &= \left| E^-(z) \right|^2. \end{aligned} \tag{5.9}$$

$E^+(z)$ and $E^-(z)$ are subject to the following complex travelling-wave equations:

$$\frac{dE^+(z)}{dz} = \left(-j\beta + \frac{1}{2}\left(\Gamma g_m(\nu, n) - \alpha(n)\right)\right) E^+(z); \tag{5.10}$$

$$\frac{dE^-(z)}{dz} = \left(j\beta - \frac{1}{2}\left(\Gamma g_m(\nu, n) - \alpha(n)\right)\right) E^-(z). \tag{5.11}$$

Their boundary conditions impose that

$$\begin{aligned} E^+(0) &= (1 - r_1)E_{in} + r_1 E^-(0), \\ E^-(L) &= r_2 E^+(L), \end{aligned} \tag{5.12}$$

where E_{in} is the input signal field to the left of the input facet. The output signal field to the right of the output facet is

$$E_{out} = (1 - r_R)E^+(L), \tag{5.13}$$

having power after coupling loss

$$P_{out} = h\nu\eta_{out}|E_{out}|^2. \tag{5.14}$$

η_{out} is the output coupling efficiency. The propagation constant

$$\beta = \frac{2\pi n_{eq}\nu}{c}$$

depends on the frequency of the signal ν and on the equivalent refractive index n_{eq}. n_{eq} can be expressed in terms of the refractive indexes of the active region n_1 and of the surrounding material n_2 as

$$n_{eq} = \sqrt{(n_1^2 - n_2^2)\frac{\Gamma}{2 - \Gamma} + n_2^2} = n_{eq_0} + \frac{dn_{eq}}{dn}n. \tag{5.15}$$

n_{eq} is a linear function of the carrier density [184] and it is the sum between the equivalent refractive index without pumping n_{eq_0} and a differential component

$$\frac{dn_{eq}}{dn} = \frac{n_1\Gamma}{n_{eq_0}(2 - \Gamma)}\frac{dn_1}{dn}. \tag{5.16}$$

The discussion can be easily extended to N signals travelling along the SOA by expressing each signal s propagating at frequency ν_s with propagation constant β_s in terms of its travelling-waves $E_s^+(z)$ and $E_s^-(z)$ to which Eqs. (5.10)-(5.11) apply.

Due to the presence of reflecting facets, the ASE shows longitudinal modes, so noise photons can exist at discrete frequencies ν_i which are integer multiples of the cavity resonances:

$$\nu_i = \nu_c + \Delta\nu_c + iK_m\Delta\nu_m, \qquad i \in [0, N_m - 1]. \tag{5.17}$$

ν_c is the cut-off frequency when no carriers are injected, so it is function of E_{g0}:

$$\nu_c = \frac{E_{g0}}{h}. \tag{5.18}$$

The frequency offset $\Delta\nu_c$ is needed to match ν_0 to a resonance. The required accuracy of the numerical solutions of the model equations along with the gain bandwidth of the SOA influences the values of the integers N_m and K_m. $\Delta\nu_m$ is the longitudinal mode frequency spacing and it is given by

$$\Delta\nu_m = \frac{c}{2\int_0^L n_{eq}dz}. \tag{5.19}$$

The spontaneous emission photon rates N_i^+ and N_j^- in the frequency range $K_m\Delta\nu_m$ obey to the following travelling-wave equations:

$$\frac{dN_i^+(z)}{dz} = (\Gamma g_m(\nu_i, n) - \alpha(n))N_i^+ + R_{sp}(\nu_i, n), \tag{5.20}$$

$$\frac{dN_i^-(z)}{dz} = -(\Gamma g_m(\nu_i, n) - \alpha(n))N_i^- + R_{sp}(\nu_i, n) \tag{5.21}$$

for which the boundary conditions

$$\begin{aligned} N_i^+(0) &= R_L N_i^-(0), \\ N_i^-(L) &= R_R N_i^+(L) \end{aligned} \tag{5.22}$$

apply. R_{sp} is the spontaneously emitted noise coupled into N_i^+ or N_i^-. In order to simplify Eqs. (5.20) and (5.21), the SOA is supposed to be ideal,

i.e., without gain saturation, loss ($\alpha = 0$), facet reflectivities, and absorption component of g_m ($g_m = g'_m$). This leads N_i^+ and N_i^- to be obtained as the solution to

$$\frac{dN_i^+(z)}{dz} = \Gamma g'_m(\nu_i, n) N_i^+ + R_{sp}(\nu_i, n) \tag{5.23}$$

and

$$\frac{dN_i^-(z)}{dz} = -\Gamma g'_m(\nu_i, n) N_i^- + R_{sp}(\nu_i, n), \tag{5.24}$$

respectively.

The solution of these two equations leads to the expression to compute the noise power at the output of the SOA in the frequency band $K_m \Delta\nu_m$ around ν_i for which the gain is equal to G_i:

$$N_{out} = \frac{G_i - 1}{\Gamma g'_m(\nu_i, n)} h\nu_i R_{sp}(\nu_i, n), \tag{5.25}$$

where

$$R_{sp}(\nu_i, n) = \Gamma g'_m(\nu_i, n) K_m \Delta\nu_m. \tag{5.26}$$

In a real device, the gain dependence on the frequencies within the spacing $\Delta\nu_m$ around ν_i can be expressed in terms of the single-pass gain G_{SP} as

$$G(\nu) = \frac{(1 - R_L)(1 - R_R) G_{SP}}{\left(1 - \sqrt{R_L R_R G_{SP}}\right)^2 + 4 G_{SP} \sqrt{R_L R_R} \sin\left[\pi \left(\nu - \nu_i\right) / \Delta\nu_m\right]}. \tag{5.27}$$

At resonance (*i.e.*, for $\nu = \nu_i$),

$$G(\nu) = \frac{(1 - R_L)(1 - R_R) G_{SP}}{\left(1 - \sqrt{R_L R_R G_{SP}}\right)^2}. \tag{5.28}$$

The rate equation

$$\begin{aligned} \frac{dn(z)}{dt} = \frac{I}{eV_{SOA}} - R(n(z)) - \frac{\Gamma}{dW} \left\{ \sum_{k=1}^{N_s} g_m(\nu_k, n(z)) \left(N_{s_k}^+(z) + N_{s_k}^-(z) \right) \right\} - \\ - \frac{2\Gamma}{dW} \left\{ \sum_{i=1}^{N_m - 1} g_m(\nu_i, n(z)) K_i \left(N_i^+(z) + N_i^-(z) \right) \right\} \end{aligned} \tag{5.29}$$

describes the dependence of the carrier density on the position z for the bias current I which is supposed to be uniformly confined in the active region only.

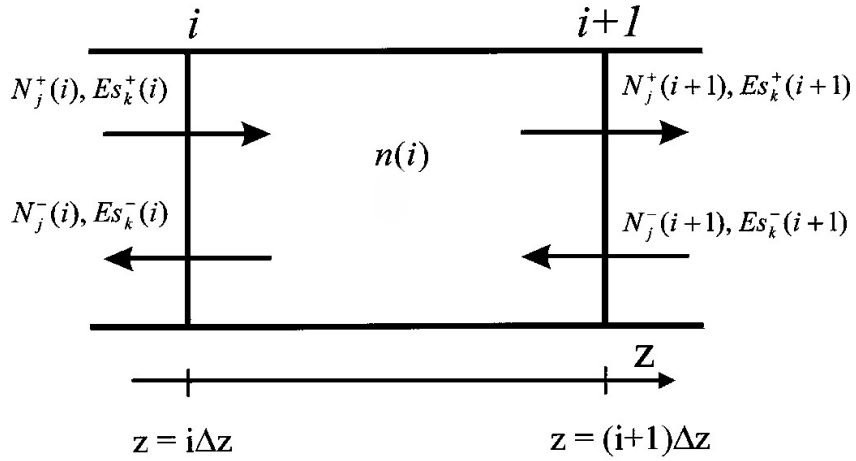

Figure 5.3: ith section of SOA model, as shown in [180].

V_{SOA} is the volume of the active region of the SOA. $I/(eV_{SOA})$ indicates the addition of carriers due to the bias current. $R(n(z))$ is the recombination rate, which is composed of two terms: radiative and non-radiative recombination rates [185]. The third component of Eq. (5.29) models the radiative recombination of the carrier induced by the amplified signal, while the fourth term of Eq. (5.29) describes the radiative recombination of the carrier due to the ASE. Only a fraction of the amplified photons populates the active region; from this phenomenon it arises the presence of Γ. The spontaneously emitted photons can exist either in TE or in TM polarizations, and the two contributions have to be summed. Since the SOA is supposed to be polarization-independent, the confinement factor Γ is supposed to be the same for both the polarization contributions; from here it results the factor 2 in the last term of the right-hand side of Eq. (5.29). If the SOA is polarization-dependent, this is taken into account with the two different confinement factors Γ_{TE} and Γ_{TM}.

The equations modelling the SOA functioning cannot be solved analytically. Connelly proposes a numerical solution which requires the amplifier to be split in N_{sec} sections. At each section interface i, the right-hand side of Eq. (5.29), $Q(i)$, is estimated by averaging the fields of every signal s E_s^+ and E_s^- and the noise photon rates N_j^+ and N_j^- at the boundaries (see Figure 5.3). The

algorithm has to predict the steady-state characteristics for which $Q(i) \to 0$ through the amplifier. The initial conditions for the signal fields, the spontaneous emission and the carrier density are set. After this initialization, the algorithm iteration begins. The first step is to compute the coefficients of the travelling-wave equations. Secondly, the fields $E_s^+(i)$ and $E_s^-(i)$ and the photon densities $N_j^+(i)$ and $N_j^-(i)$ are estimated as finite difference solutions of Eqs. (5.10) - (5.11) and (5.20) - (5.21) respectively as follows. The spatial derivative of a forward travelling-wave W^+ can be approximated as

$$\frac{dW^+}{dz} = \frac{W_i - W_{i-1}}{\Delta z}, \tag{5.30}$$

where $\Delta z = L/N_{sec}$ is the length of each section. Analogously, for a backward travelling-wave W^- the approximation is

$$\frac{dW^-}{dz} = \frac{W_{i+1} - W_i}{\Delta z}. \tag{5.31}$$

At this point, $Q(i)$ is evaluated. If $Q(i) > 0$, the carrier density has to be increased by a factor $1 + V(i)$, where $V(i)$ is a weight factor less than 1. Otherwise, if $Q(i) < 0$, the carrier density has to be decreased by a factor $1+V(i)$. Each time $Q(i)$ changes its sign with respect to the previous iteration, the weight $V(i)$ is halved. The iteration progresses until a given tolerance on the maximum change in the photon rates, in signal fields, and in the carrier density throughout the SOA is reached. At the end of the iteration, all the SOA parameters, such as the output spontaneous emission power spectral density, the ASE power, the signal gain, and the NF are computed.

Even if the presented model is very accurate, it is not feasible to apply it for the purposes of this thesis, since on one side it requires a complete knowledge of the device and on the other side it is computationally heavy.

5.4 SOA Transfer Function

When the gain is saturated, the SOA acts as a limiting amplifier, as demonstrated in [186]. The amplification of both optical pulses and modulated signals by SOAs is reduced by nonlinear phenomena induced by the amplifier itself. Some of them are the gain saturation generated by the carrier-density depletion, carrier transport in multiple layers and intraband carrier dynamics. The focus of this section is to evaluate the impact of gain saturation on the amplified signal. Supposing to neglect the nonlinearities induced by carrier transport and intraband carrier dynamics, the integrated gain $h(t)$ is, by definition,

$$h(t) = \int_0 Lg(z,\tau)dz, \tag{5.32}$$

where g is the gain, τ is the reduced time, z is the longitudinal position, and L is the length of the SOA. By differentiating Eq. (5.32) on the bases of the rate equations,

$$\frac{dh}{d\tau} = \frac{g_0 L - h}{\tau_c} - \frac{P_{in}(\tau)}{\tau_c P_S}\left[e^h - 1\right], \tag{5.33}$$

where g_0 is the unsaturated small-signal gain, τ_c is the carrier lifetime, $P_{in}(\tau)$ is the power envelope of the input signal, and P_S is the saturation power. The small-signal analysis on Eq. (5.33) gives rises to the SOAs transfer function in the frequency domain

$$H_{SOA}(\omega) = G_{CW}\frac{1 + \frac{\ln(G_0/G_{CW})}{G_{CW}-1} - j\omega\tau_c}{1 + G_{CW}\frac{\ln(G_0/G_{CW})}{G_{CW}-1} - j\omega\tau_c}. \tag{5.34}$$

ω is the modulation angular frequency, G_{CW} is the CW gain, and G_0 is the unsaturated gain, which, for the input power P_{in}, are given by

$$G_0 = \exp(g_0 L), \tag{5.35}$$

$$G_{CW} = G_0 \exp\left[-(G_{CW} - 1)\frac{P_{in}}{P_S}\right]. \tag{5.36}$$

The frequency response can be computed as the squared modulus of $H_{SOA}(\omega)$, $|H_{SOA}(\omega)|^2$. $|H_{SOA}(\omega)|^2$ provides the SOA output power frequency

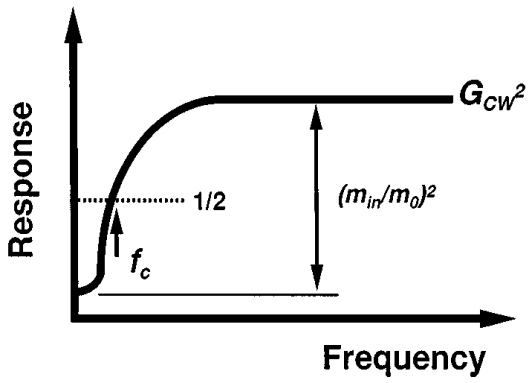

Figure 5.4: Schematic diagram of the frequency response of an SOA, as shown in [186].

response to the modulation of the input power. Figure 5.4 represents a schematic of the frequency response. The SOA works as a high-pass filter: at high frequencies, the response is flat and it is proportional to G_{CW}^2, the CW power gain. The output signal of the SOA has a modulation depth m, depending on the modulation depth of the input signal m_{in}, on the CW gain G_{CW}, and on the transfer function in frequency domain $H_{SOA}(\omega)$:

$$m = m_{in}\frac{|H_{SOA}(\omega)|}{G_{CW}}. \tag{5.37}$$

From Eq. (5.37) and Figure 5.4 two behaviours can be identified: at higher frequencies the modulation depth is preserved when the signal crosses the SOA ($m \to m_{in}$ for $\omega \to \infty$); at lower frequencies the modulation depth is reduced (since $|H_{SOA}(\omega)|/G_{CW} < 1,\ m < m_{in}$). This phenomenon is the SGM introduced in Chapter 5.1. At lower frequencies the carrier density is affected by the modulated signal, while at higher frequencies SGM does not occur due to the carrier lifetime.

Another useful parameter to evaluate the SOA is the *cut-off* frequency f_c, at which $m = m_{in}/\sqrt{2}$, *i.e.*, when the output electrical power is halved with respect to the input power. f_c can be expressed in terms of G_0, G_{CW}, and τ_c as

$$\frac{1}{2\pi\tau_c}\sqrt{G_{CW}^2\overline{g}^2 + 2G_{CW}\overline{g} - 2\overline{g}^2 - 4\overline{g} - 1}, \tag{5.38}$$

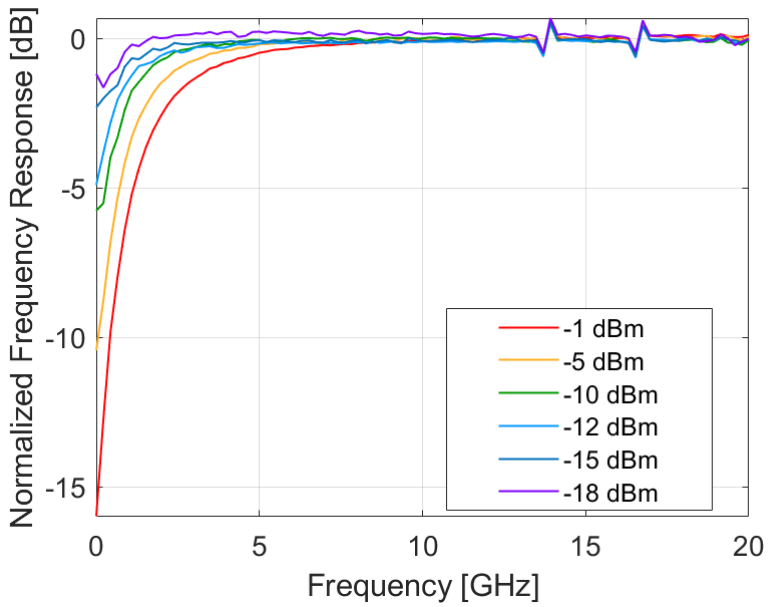

Figure 5.5: SOA TFs computed with a VNA for a bias current of 225 mA and an input power ranging from -18 dBm to -1 dBm.

where

$$\overline{g} = \frac{\ln\left(\frac{G_0}{G_{CW}}\right)}{G_{CW} - 1}. \tag{5.39}$$

The response reduction efficiency is measured by the ratio m/m_{in}, while f_c shrinks the bandwidth. When $\omega \to 0$, the modulation depth can be defined as

$$m_0 = m_{in}\frac{1 - \overline{g}}{1 + G_{CW}\overline{g}}. \tag{5.40}$$

In the unsaturated case, *i.e.*, when $G_{CW} = G_0$, the output modulation depth is unvaried with respect to the input modulation depth, so $m_0 = m_{in}$ since $\overline{g} = 0$. In the saturated case, when G_{CW} decreases, the modulation depth ratio m_0/m_{in} is reduced.

The SOA high-pass filter behaviour is enhanced by increasing the input power, as it will be shown in the following sections. The limiting function at lower frequencies can be used to reduce the noise components at lower frequencies, but it lowers the signal components as well, causing distortions [186].

Figure 5.5 depicts the comparison among some of the SOA TFs obtained

with a VNA for input power ranging between -18 dBm and -1 dBm and a bias current of 225 mA. It is evident that for higher input powers the notch introduced by high-pass filtering of the SOA TF is deeper, and so it introduces a distortion in the first subcarriers of the DMT signal, as it will be discussed in the following sections.

These measured TFs can be matched to the theoretical TFs previously introduced. The model requires the knowledge of the small-signal gain G_0, of the CW gain G_{CW}, and of the carrier lifetime τ_c. The first two parameters have been measured (see Figure 5.1), while τ_c has been obtained by fitting the theoretical curves: the correct modelling of the SOA TF translates in finding the best τ_c. To achieve this objective, the TFs for a wide range of values of τ_c are computed. For each TF two parameters of merit have been calculated:

1. the Sum of Squared estimate of Errors (SSE):

$$SSE = \sum_{i=1}^{N} (y_i - x_i)^2; \tag{5.41}$$

2. the adjusted coefficient of determination, or adjusted R-squared ($\overline{R}^2$) [187]:

$$\overline{R}^2 = 1 - \left[1 - \frac{SSE}{\sum_{i=1}^{N} (y_i - y_{av})^2} \right] \cdot \frac{N-1}{N-(k+1)}, \tag{5.42}$$

where x_i are the predicted values from the fitting, y_i are the samples of the frequency response from VNA, their average is y_{av}, N is the sample size, and k is the number of independent variables, in this case $k = 1$ (*i.e.*, τ_c). The best value of τ_c satisfies these two conditions:

$$\begin{gathered} \min\left(SSE\right) \\ \max\left(\overline{R}^2\right). \end{gathered} \tag{5.43}$$

In Figure 5.6 an example of this process of fitting is shown for a bias current of 225 mA and -1 dBm of input optical power, which leads the best choice of τ_c to be equal to 233 ps. The model does not perfectly follow the low-frequency

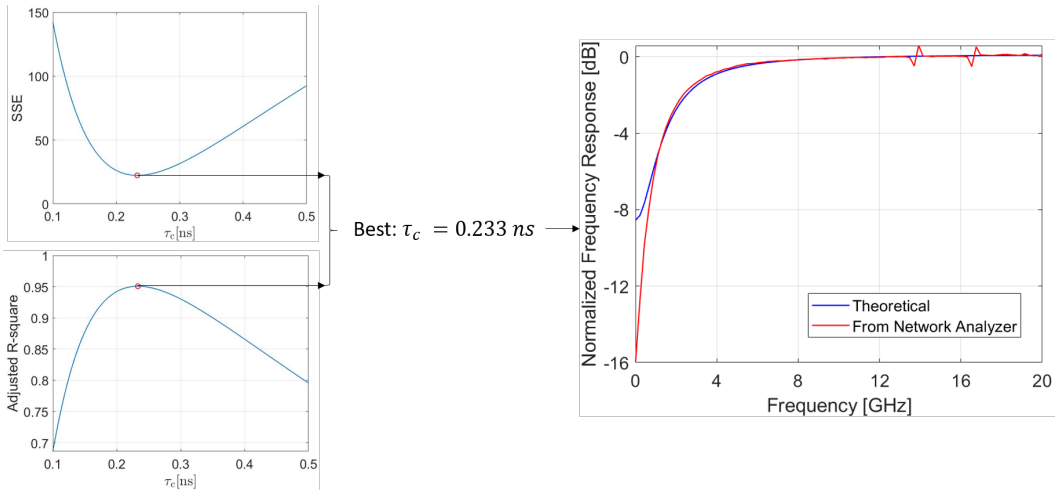

Figure 5.6: Example of choice of the best τ_c. In the left upper graph, the trend of SSE, in the left down graph, the trend of $\overline{R}^2$, and in the right graph the obtained fitting of the TF (in blue) along with the measured one (in red).

notch for a high value of the input power, but, as demonstrated in Figure 5.7(a) for a bias current of 200 mA and an input power of -12 dBm, when the power is lower, the model perfectly matches. In Figure 5.7(b) the dependence of the optimum values of τ_c on the values of power and bias current are presented. As expected, higher saturation conditions induce a reduction of the carrier lifetime, since they lead to a higher stimulated recombination rate. τ_c is then inversely proportional to saturation intensity of light [188]. τ_c can be experimentally measured as well, as demonstrated in [189], where the polarized ASE noise has been exploited to characterize the SOA in terms of bandwidth.

Another parameter taken into account in [186] is the cut-off frequency. It gives an indication to evaluate the suppression of the first subcarriers: the subcarriers at frequencies lower than f_c face a significant reduction with respect to the high frequency subcarriers. Figure 5.8 shows the theoretical TFs for 225 mA and input powers ranging between -14 dBm and -1 dBm. For a power of -1 dBm, all the subcarriers at frequencies lower than 2 GHz are heavily impaired. This means that the bit-loading algorithm loads the subcarriers

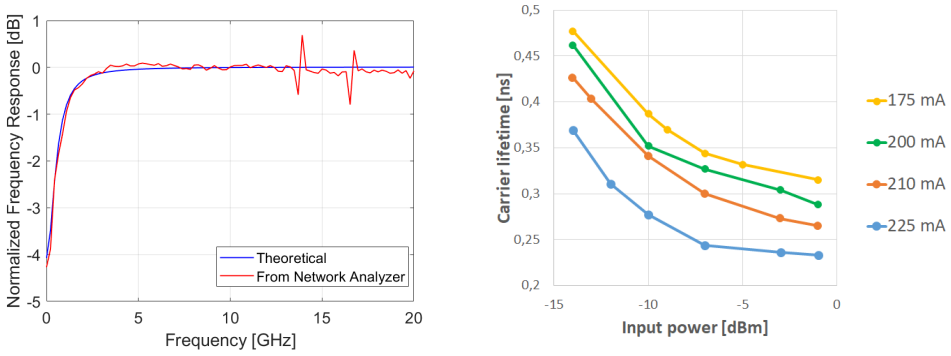

(a) 200 mA, -12 dBm **(b)** Carrier lifetime

Figure 5.7: (a) SOA TF fitting for 200 mA bias current and -12 dBm input power; (b) Dependence of carrier lifetime τ_c on the saturation conditions, for bias currents in the range between 175 mA and 225 mA and for input powers between -14 dBm and -1 dBm.

of the modulating DMT signal with a lower modulation format [127]: in the following paragraphs the impact of this reduction on the transported capacity will be quantified. By lowering the input power, the value of f_c decreases as well, and for -14 dBm it is close to 0. The same happens by reducing the value of the bias current: high saturation conditions correspond to high values of cut-off frequency. The cut-off frequency cannot be computed for all the SOA operation conditions, since for low input powers and/or for low values of current the gain gap between 0 GHz and high frequencies can be lower than 3 dB: the lower is the bias current, the more conditions fall in this casuistry.

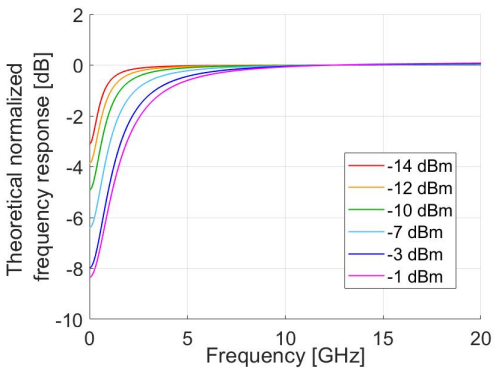

(a) Theoretical frequency responses at 225mA

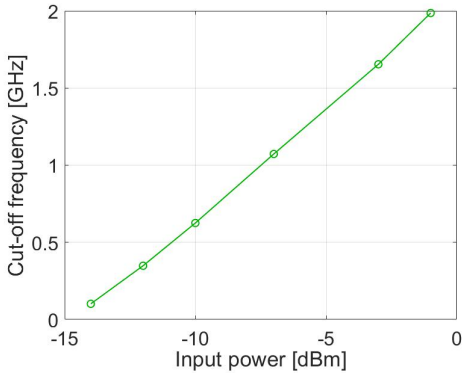

(b) Cut-off frequencies at 225mA

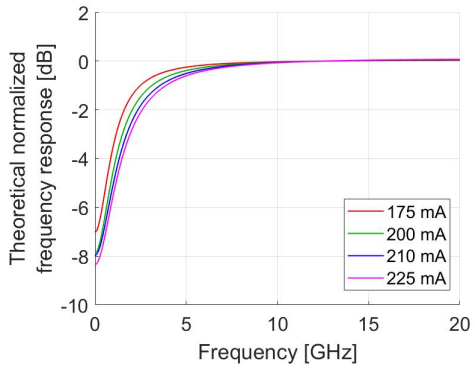

(c) Theoretical frequency responses at -1 dBm

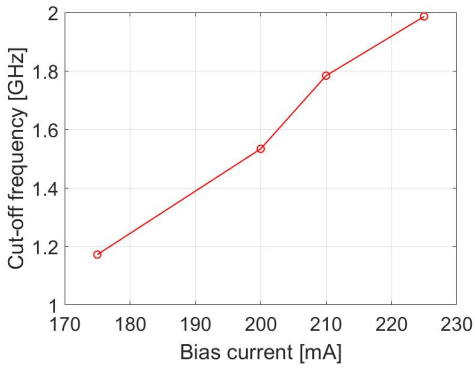

(d) Cut-off frequencies at -1 dBm

Figure 5.8: Theoretical frequency responses and corresponding cut-off frequencies.

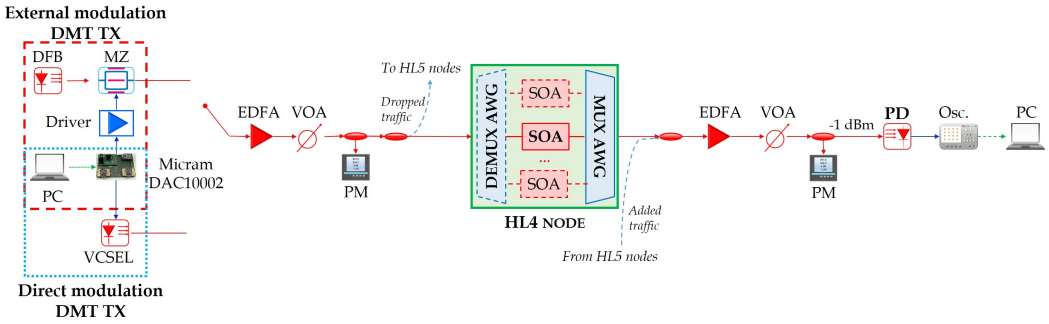

Figure 5.9: Experimental setup for DSB and SSB DMT signal externally modulating a DFB laser (red box) and directly modulating a VCSEL (blue box).

5.5 SOA impact on DMT channels generated with externally modulated DFB lasers

5.5.1 Dual Sideband DMT signal

In Chapter 4.5 the effect of node crossing in absence of SOAs has been evaluated. In the following section the effect of the complete HL4 node crossing (100-GHz spacing filters and SOA) on the high-capacity DMT signal performance is assessed with the experimental setup reported in Figure 5.9. A 1558-nm DFB laser is externally modulated by a 25-GHz intensity Mach-Zehnder (MZ) modulator with a DSB DMT signal. The DMT signal is composed of 256 subcarriers in 20-GHz range, so the subcarrier spacing is 78.125 MHz. A CP of 2.1% of the symbol length is added. The DMT signal is generated by a 100 GS/s MICRAM DAC (DAC10002) with 40-GHz electrical bandwidth and 6-bit vertical resolution. The cascade of an EDFA and a VOA sets the input power to the HL4 node between -14 dBm and 0 dBm. The bias current of the SOA ranges between 100 mA and 225 mA, to modify the saturation conditions within the working range. The optical signal is received by a 14-GHz PIN photodiode keeping the received power to the constant value of -1 dBm for all the measurement conditions; the received signal is then

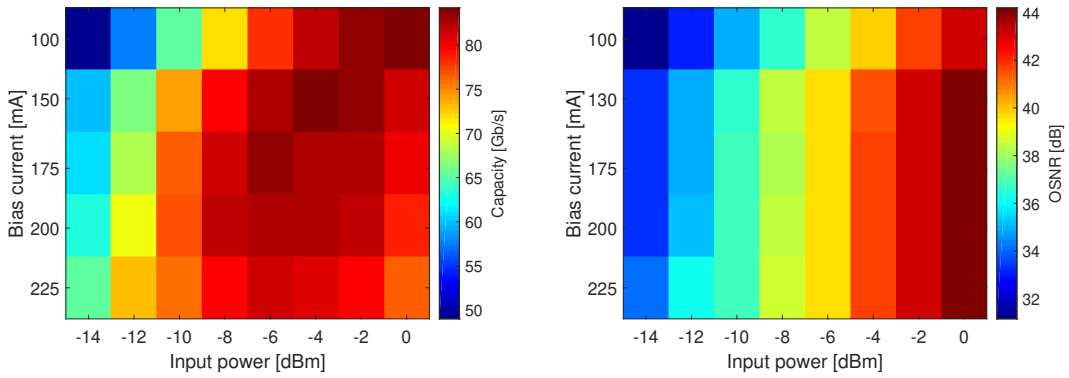

(a) Transmitted capacity **(b)** Measured OSNR

Figure 5.10: Heatmaps of the measured capacity and OSNR for several bias currents in case of DSB DMT signal crossing a HL4 node.

acquired by a Tektronix real-time oscilloscope with 8-bit vertical resolution, 100 GS/s and 33-GHz electrical bandwidth. Off-line processing provides the features described in Section 3.5, *i.e.*, digital symbol synchronization, CP removal, subcarriers phase recovery and demodulation and BER count. The total transported capacity gives a measurement of the system performance and it is achieved by performing the standard Chow's bit- and power-loading algorithm [127] with a target BER of $3.8 \cdot 10^{-3}$ (in order to exploit an advanced hard-decision FEC code with 7% overhead [159]) for different SOA bias currents and SOA input optical powers.

Figure 5.10(a) reports the capacity dependence on the input power and SOA bias current. As it can be easily foreseen, the capacity increases for higher SOA input powers for each bias current in analysis, thanks to the higher OSNR (see Figure 5.10(b)). However, the maximum capacity obtained at higher input powers is reduced for higher bias currents and the maximum capacity is achieved for input powers ranging from 0 dBm to -5 dBm for bias currents increasing from 100 mA to 225 mA. The capacity in these deeper saturation conditions is reduced by the more effective SOA gain compression, which, as shown in Section 5.4 and in [186], leads the SOA to act as an electrical

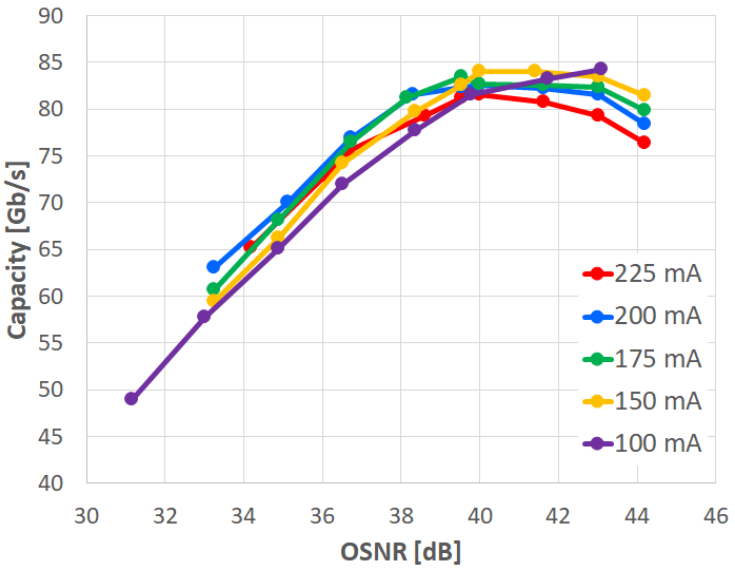

Figure 5.11: Dependence of the capacity on the measured OSNR for DSB DMT transmission.

high-pass filter. Both the magnitude and the width of the low-frequency notch is significantly enhanced for higher bias currents. By comparing the curves in Figure 5.12, the SNR achievable by low-frequency subcarriers at 225 mA is at least 3 dB lower than for 100 mA and this limits the overall capacity. On the contrary, the SOA working at lower bias current does not introduce distortions, as it can be noticed by the almost perfect superposition with the case in absence of SOA.

The performance is a trade-off between the OSNR and the SOA gain saturation, so an optimum bias condition with respect to the input optical power can be identified by Figure 5.10(a) in order to maximize the transported capacity after the HL4 node. Figure 5.10(b) shows the dependence of the OSNR on the SOA bias current and input power. The OSNR faces a reduction of more than 10 dB when the power lessens of 14 dB. By analyzing the dependence of the measured capacity on the OSNR (see Figure 5.11), for lower input powers (*i.e.*, for lower OSNRs) the most significant contribution to the reduction of the capacity is the noise the SOA introduces in the system: the

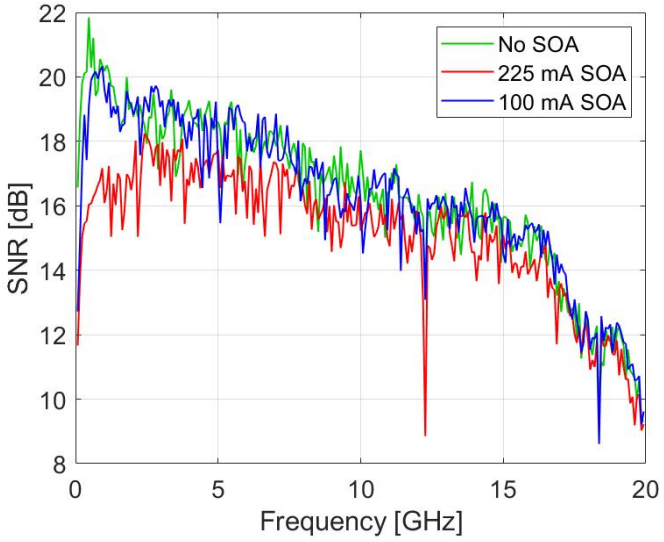

Figure 5.12: Measured SNRs for BTB without SOA, for SOA bias current of 225 mA, and 100 mA, and an input power of -1 dBm.

capacities are comparable, no matter the SOA bias current. The reduction of the OSNR at 100 mA (already observed in CW) causes a shift of 1 dB of the capacity curve towards lower OSNRs, which highlights the strict dependence of the performance on the introduced noise at low power.

5.5.1.1 Optical SSB induced by SOA

In Figure 5.13 the optical spectra for two SOA operation conditions are shown. Especially for high bias currents and input powers, the optical signal at the output of the SOA shows a suppression of one of the two DMT signal sidebands. This is due to the frequency chirp $\Delta f_{SOA}(t)$ introduced by the SOA when it amplifies an intensity-modulated signal. Δf_{SOA} is a function of the SOA SPM $\phi_{SOA}(t)$ [190]:

$$\Delta f_{SOA}(t) = -\frac{1}{2\pi} \cdot \frac{d\left[\phi_{SOA}(t)\right]}{dt}. \tag{5.44}$$

The signal after the SOA presents a negative chirp peak after the leading edge of the pulses (red chirp) and a positive chirp peak (blue chirp) after the tailing edge of the pulses. This leads to the suppression of one sideband. Since

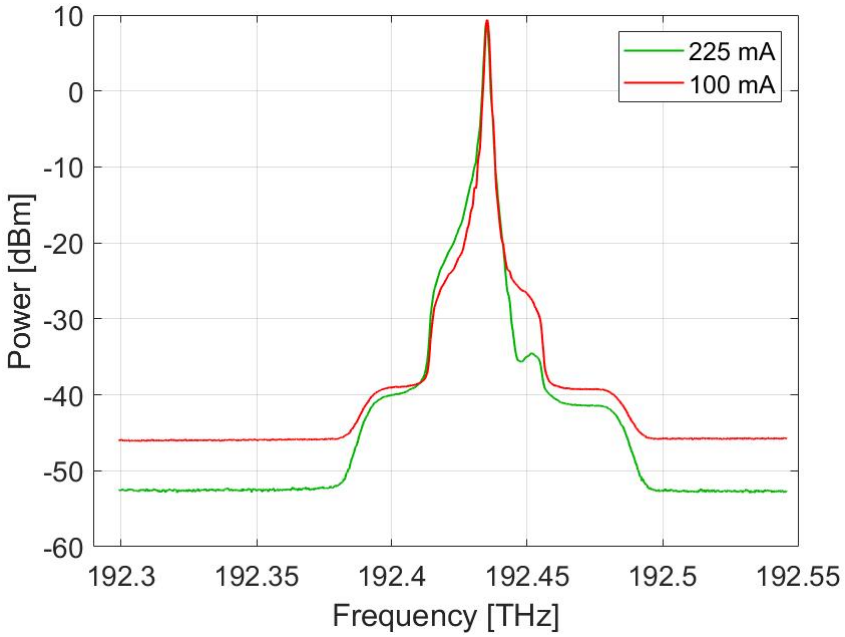

Figure 5.13: Optical spectrum produced by an OSA at the output of the SOA for an optical power of -1 dBm and a bias current of 225 mA (green) and of 100 mA (red), when the optical signal is generated by externally modulating a DFB laser with a DSB DMT signal.

SPM is dependent on the signal power, the conversion from optical DSB to optical Vestigial Sideband (VSB) is emphasized for higher bias currents, the input power being the same. Some works exploit SOAs to filter out a sideband instead of the classical filtering, but SGM can cause amplitude distortion in broadband signals if this effect is not properly minimized [191]-[192].

5.5.2 Single Sideband DMT signal

The same experimental setup shown in Figure 5.9 has been employed to evaluate the impact of SSB external modulation of a DFB laser (see Figure 5.14). The only difference is that a Finisar Waveshaper emulating the TF of a 25-GHz spacing WSS [152] provides the SSB filtering before setting the desired optical power.

At 0 dBm, the capacity faces a reduction in the range between 4.5%

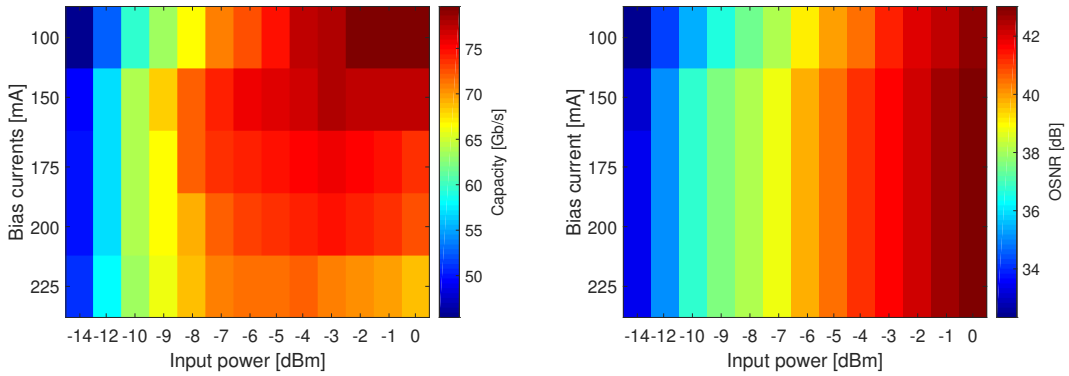

(a) Transmitted capacity **(b)** Measured OSNR

Figure 5.14: Heatmaps of the measured capacity and OSNR for several bias currents in case of SSB DMT signal crossing a HL4 node.

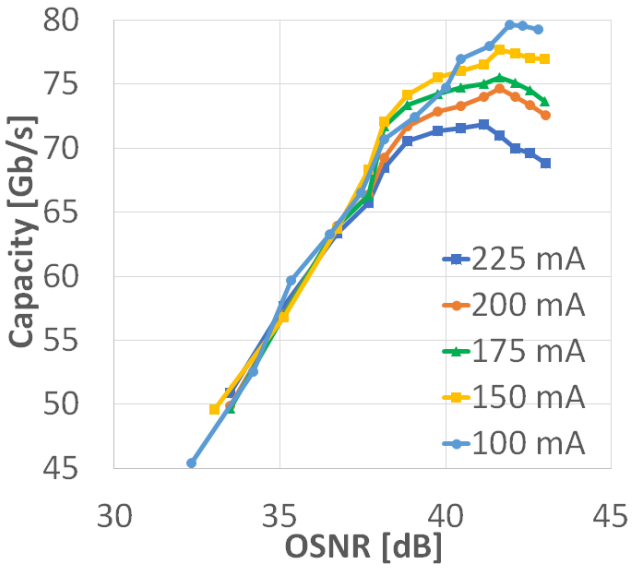

Figure 5.15: Dependence of the capacity on the measured OSNR for SSB DMT transmission.

and 9% with respect to DSB DMT modulation, the values of OSNR being comparable. By decreasing the power, the capacity increases: the increment is more significant at high bias currents (at 225 mA the capacity increases of 3 Gb/s by decreasing the power of 4 dB) than at lower bias currents (0.7 Gb/s by decreasing the power of 3 dB at 150 mA and 0.3 Gb/s by decreasing the power of 2 dB). Moreover, the maximum achievable capacity is reached at lower powers for higher currents: this may be due on one side to a reduced high-pass filtering introduced by the SOA with respect to higher powers (see Section 5.4) and on the other side on the limited amount of noise introduced by the amplifier. As shown in Figure 5.15, the capacity increases for values of OSNR higher than 40 dB, so in this range the main effect is the SOA filtering. For OSNRs lower than 37 dB, the capacity is strictly related to the noise introduced by the SOA, and no more dependent on the bias current of the SOA, and it decreases with it. This phenomenon has been already observed for DSB modulation; the capacity at low powers is reduced with respect to the DSB modulation. For an OSNR of 33.5 dB, the capacity is approximately equal to the target 50 Gb/s for SSB modulation, while for DSB modulation the capacity is nearly ranges between 58 Gb/s and 65 Gb/s. This reduction of the 20% is due to a higher robustness to noise and to a better spectral efficiency of the SSB DMT modulation with respect to the DSB modulation, which have already been discussed in the previous chapter.

5.6 SOA impact on DMT channels generated with directly modulated VCSELs

5.6.1 Dual Sideband DMT signal

The impact of SOA crossing in case of DMT DM has been studied for a 1535-nm VCSEL. In this paragraph and in the following, 20-GHz DSB and

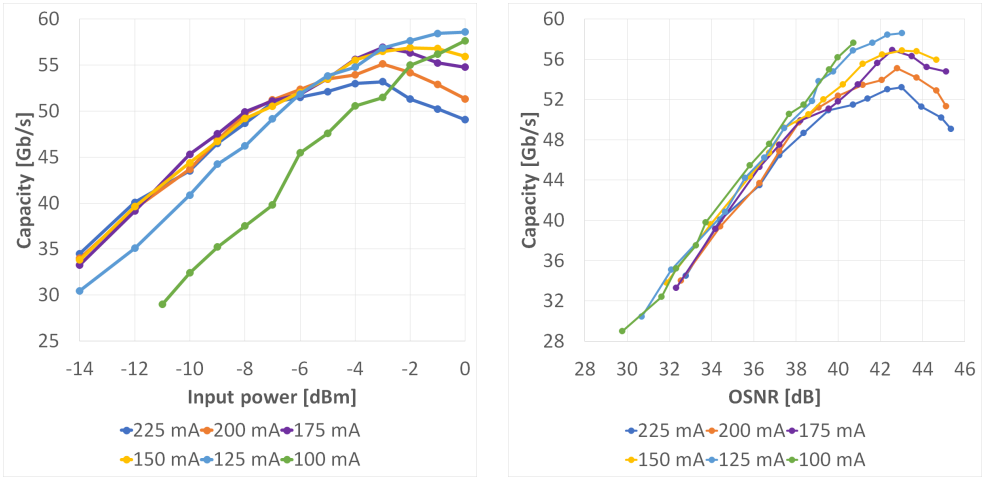

(a) Capacity versus input power **(b)** Capacity versus OSNR

Figure 5.16: Transmitted capacity for DM-VCSEL modulated with a 20-GHz DSB DMT signal.

SSB modulations are investigated, respectively. The evaluation is performed by directly detecting the optical signal again with a PD with 14-GHz electrical bandwidth. The input power to the receiver is set to -1 dBm.

Figure 5.16(a) shows the dependence of the measured capacity on the SOA bias current and input power. By increasing the optical power, for each bias current, the capacity increases thanks to a higher OSNR. This happens till a given optical power ranging between -4 dBm and -2 dBm for bias currents higher than 150 mA. When the power is further increased, the capacity decreases. At 225 mA the capacity decreases of 8.2% at 0 dBm with respect to the peak value. This percentage diminishes with the bias current. This is due to the gain compression and the significant low-frequency notch already discussed in the previous sections. By comparing the measured SNR for a bias current of 225 mA and an input power of -1 dBm and the SNR without the presence of the SOA but introducing the same noise level (so with the same OSNR as the one measured with the SOA), the first subcarriers face a reduction of 10 dB due to the high-pass filtering of the SOA. The same measurement has been performed

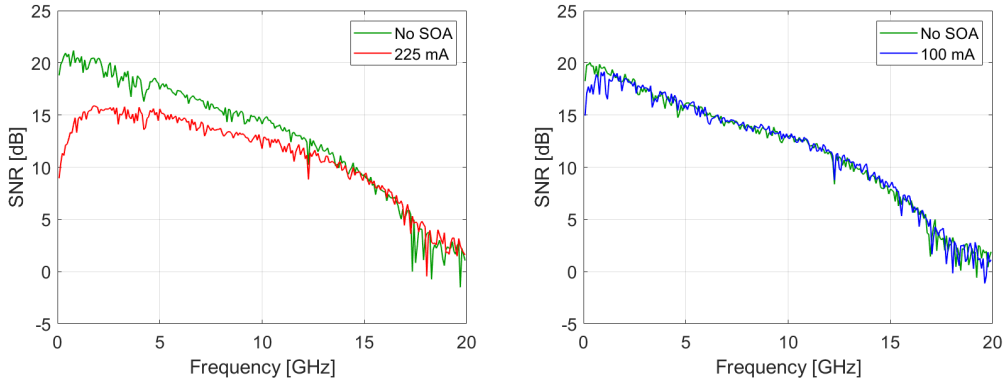

(a) 225 mA **(b)** 100 mA

Figure 5.17: Measured SNRs for 100 mA and 225 mA bias currents and -1 dBm input power along with the corresponding curves without the SOA. The effect of SOA high-pass filtering causes a reduction of 10 dB at low frequencies for 225 mA.

again for -1 dBm input power, but lowering the bias current to 100 mA: in this case, the reduction of the low-frequency subcarriers due to the presence of the SOA is only 3 dB and it is concentrated on the very first subcarriers, while for 225 mA the SNRs become comparable only for frequencies higher than 13 GHz. The same effect can be detected on the correspondent received reconstructed electrical spectra shown in Figure 5.18.

For input powers higher than -6 dBm, the optimal regime of functioning of the SOA in presence of a directly-modulated VCSEL with DSB DMT modulation is achieved for 125 mA, because it is the best trade-off between gain compression and OSNR. For lower powers, the most impacting factor on the achievable transmitted capacity is the noise introduced by the amplifier; lower bias currents correspond to lower values of OSNR, so higher currents guarantee a better performance. At 100 mA the capacity is heavily impaired by the noise introduced by the SOA, and this leads to a reduction of the capacity of 20% at -10 dBm with respect to 125 mA and of the 30% when compared to the other bias currents. The minimum input power for which the

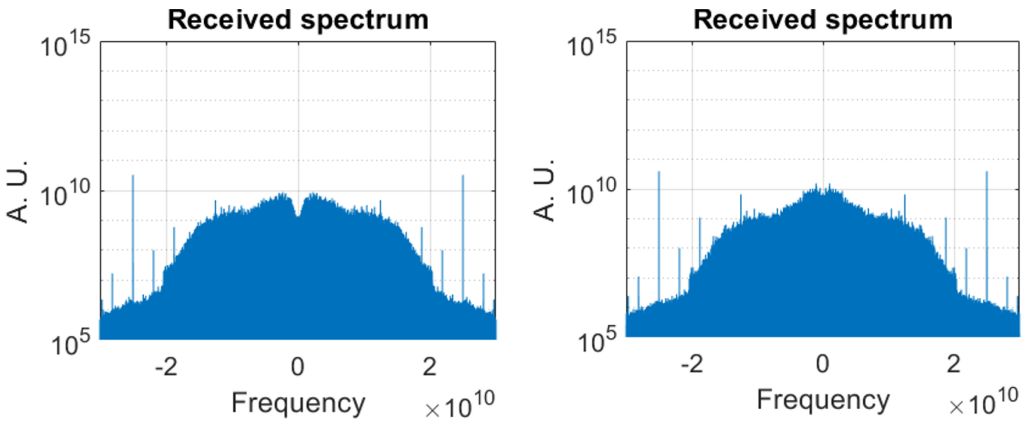

(a) 225 mA **(b)** 100 mA

Figure 5.18: Received electrical spectra for 100 mA and 225 mA bias currents and -1 dBm input power. The effect of SOA high-pass filtering is more noticeable for higher bias currents.

SOA correctly works in DSB modulation for 20-GHz DMT signal is -11 dBm at 100 mA. For this current, in order to further decrease the optical input power, the modulating signal bandwidth has to be reduced to fit the 14-GHz bandwidth of the PIN photodiode. Moreover, the target capacity of 50 Gb/s can be achieved with this operation conditions for input powers higher than -8 dBm for bias currents higher than 150 mA, while for 125 mA the minimum power is increased to -6 dBm.

5.6.2 Single Sideband DMT signal

The same measurements as the ones discussed in the previous sections have been performed for 20-GHz SSB DMT direct modulation of the aforementioned VCSEL and the optical signal is detected by the same 14-GHz PIN photodiode as the previous section for a received power of -1 dBm. Figure 5.19(a) depicts the dependence of the transmitted capacity on the input power. As previously described, a peak in the transmitted capacity is reached for input powers around -3 dBm/-2 dBm for high bias currents. It increases of 7.9% at 225 mA and the

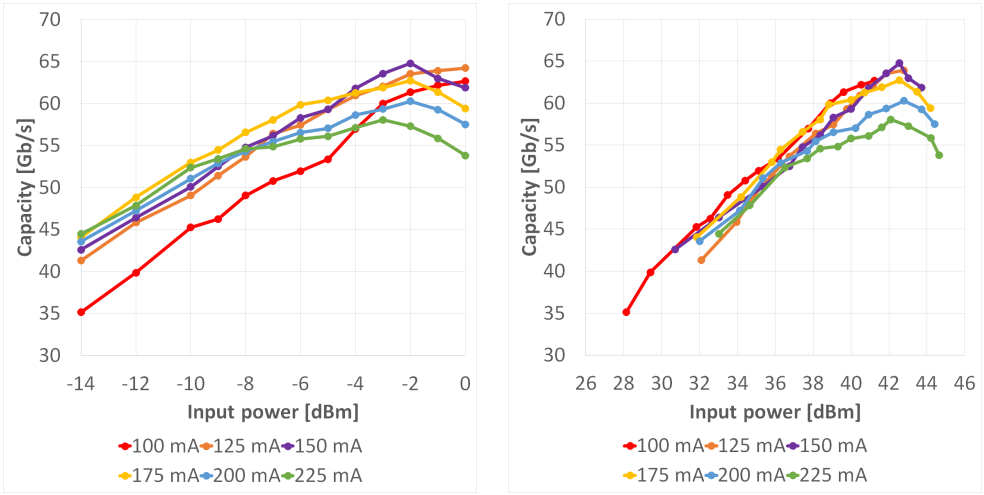

(a) Capacity versus input power **(b)** Capacity versus OSNR

Figure 5.19: Transmitted capacity for DM-VCSEL modulated with a 20-GHz SSB DMT signal.

percentage decreases with the bias current, as previously highlighted for DSB modulation. Again, from Figure 5.19(b) it is evident that the capacity depends on the gain saturation for high input powers, while the predominant impairment for low bias currents is the noise introduced by the SOA. The curves for OSNR up to 38 dB highlight that the measured capacity is comparable for every bias current, while for higher saturation conditions lower bias currents can achieve higher capacities, the OSNR level being the same.

By comparing the capacities achieved with SSB modulation with the ones obtained by modulating the VCSEL with a DSB DMT electrical signal, SSB outperforms DSB. For high powers, SSB-modulated optical signals suffer 40% less reduction in the low-frequency subcarriers with respect to DSB modulation at 225 mA, as shown in Figure 5.20, which compares the normalized SNRs, *i.e.*, the curve obtained by subtracting the SNR achieved for a given SOA saturation condition to the BTB SNR estimated by imposing the same noise level measured in presence of the SOA. A hypothesis to justify this phenomenon could be the partial reduction of the carrier introduced by the SSB filtering,

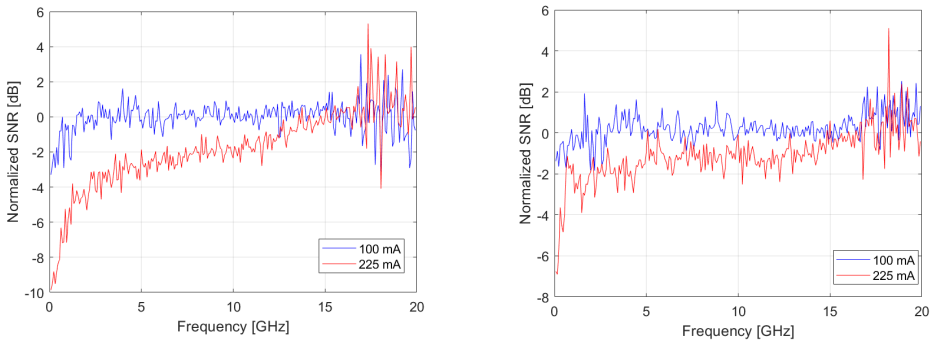

(a) DSB modulation **(b)** SSB modulation

Figure 5.20: Normalized SNRs for 100 mA and 225 mA for an input power of -1 dBm.

so the lowering of the CSPR [164], defined for an electric field E_s as the ratio between the squared modulus and the variance of the field,

$$CSPR = \frac{|E_s|^2}{\sigma^2_{E_s}}, \tag{5.45}$$

could cause a less significant impact of the SGM of SOA on the first DMT subcarriers. Table 5.2 shows the dependence of the CSPR on the SOA saturation condition, where it is evident that lower saturation conditions face a less significant increase of the CSPR with respect to higher saturation conditions. Another hypothesis explaining the different behaviour of DSB DM modulation with respect to SSB DM modulation could be the interplay between chirp parameters and SOA filtering, analogously to what has been presented in Section 4.2 [161] for tight optical filtering. Further evaluations to validate this hypothesis are still to be performed.

For lower bias currents, the SSB modulation is more robust to the introduction of noise, so the capacity is less impaired by SOA ASE level. The capacity is increased by 30% at low input power when the VCSEL is modulated with the 20-GHz SSB rather than with DSB signal with the same electrical bandwidth. This reduction is due to a higher robustness to noise and to a better spectral efficiency of the SSB DMT direct modulation with respect

Modulating signal	BTB	SOA input power	225 mA	125 mA
20-GHz DSB DMT	17.34	0 dBm	21.20	18.75
		-14 dBm	18.81	17.66
20-GHz SSB DMT	15.94	0 dBm	17.68	16.87
		-14 dBm	14.82	14.552

Table 5.2: CSPR for different SOA operating conditions along with the BTB measurement.

to the DSB modulation, which have already been discussed in the previous chapter. The resilience of SSB to the channel conditions leads to a slight reduction in the minimum input power required to achieve the target capacity of 50 Gb/s with respect to DSB modulation. For bias currents higher than 125 mA, the minimum requested input power ranges between -11 dBm and -9 dBm, and a reduction of only 8 Gb/s is faced when the input power is set to -14 dBm.

This study allows to evaluate the impact of the presence of an SOA as WBL in HL4 and HL3 nodes. In both cases, the proper bias current has to be chosen to minimize the impact of the SOA in terms of signal distortion due to the high-pass filtering and of output OSNR. From these measurements, it can be hypothesised that the SOA influences the system performance to a greater extent when the channels are DSB-modulated, *i.e.* in a HL4 node and when they are first added in an HL3 node. In fact, a channel which is added in an HL3 node has to cross a WBL at HL4 level, a WBL and a booster SOA at HL3 level. A DSB channel has to cross at least 3 SOAs (refer to Figures 2.6 and 2.7 to remind the schematic of the network nodes). The dropped channels sent to lower HL4 nodes are SSB-modulated, so the crossings of the WBL and of the booster SOA cause less significant impairments. Anyway, it is important to notice that the dropped channels by an HL3 node have crossed at least 5 SOAs (1 at HL4 level and 4 in the HL3 node), so in absolute terms they face

a more significant capacity reduction due to the cascade of 5 SOAs than the single DSB-modulated channel at HL4 level; however this reduction could be more due to the add phase than to the drop one. Some other measurements are required to support this hypothesis.

5.7 SOA application in an HL4-like node

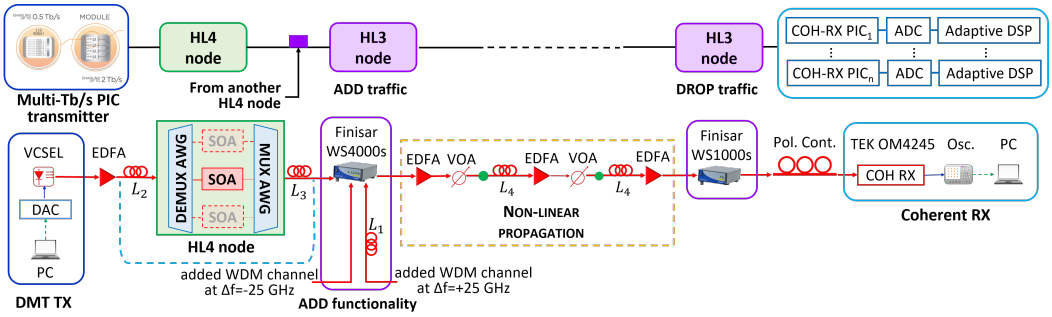

Figure 5.21: Schematic of the network architecture with HL4 and HL3 node (top) along with the experimental setup (bottom).

The transmission performance in presence of three DM DMT-based high-capacity channels, multi-hop transmission consisting of a 100-GHz HL4 node, two 25-GHz spaced HL3 filters and medium-reach propagation is evaluated with the experimental setup shown in Figure 5.21. It differs from the setup employed in Figure 4.13 for the presence of an HL4 ring, indicated with a dashed light-blue line, made up of an HL4 node and two SSMF fiber spans, a $L_2 = 9$ km SSMF span before the node and a $L_3 = 6$ km SSMF fiber after it. The HL4 node is composed of two 100-GHz AWGs and the SOA characterized in the previous sections, which works as a WBL. From the evaluations in the previous sections, the chosen operation condition of the SOA implies a bias current of 200 mA and an input power of -10.5 dBm: in this way the losses in the HL4 link are recovered without introducing the effects of gain saturation. Moreover, the overall transmission length sums up to 116 km, while in Figure 4.13 the signal propagates along 100 km, 150 km, and 200 km.

The two other channels at 25-GHz spacing are added after the HL4 node, and aggregated with a Waveshaper emulating the TF of a 25-GHz WSS [152], which performs the SSB filtering of all the channels as well. The channels propagate along two SSMF spans, $L_4 = 50$ km long. The launch power per span of the three channels is set to +5 dBm. After the crossing of a Waveshaper emulating the TF of a DEMUX 25-GHz WSS, the signal is then coherently received as in Section 4.4. The distortions due to nonlinear multichannel propagation are mitigated with a 3$^{\text{rd}}$ order Volterra equalizer [94].

In order to evaluate the effects of node filtering and of the SOA presence on single-channel transmission, the transmitted capacities in several conditions have been measured:

1. in Back-to-Back (BTB) with the DEMUX WSS both with and without the 2 HL4 AWGs, without the SOA;

2. considering the entire HL4 ring, both with and without the SOA, with only the DEMUX WSS;

3. taking into account the whole HL4 ring, with both the add and the drop stages, *i.e.*, with both the 25-GHz WSS filters;

4. crossing the entire setup depicted in Figure 5.21, with an overall propagation length of 116 km.

The multichannel propagation has been analyzed with the entire setup.

In Table 5.3 the measured capacities are summed up. The capacity in presence of 25-GHz SSB modulation and BTB condition is 68.3 Gb/s, which is taken as a reference. A capacity reduction of 4 Gb/s is faced when the two 100-GHz AWGs forming the HL4 node are crossed. The propagation along 16 km introduces a reduction of other 2 Gb/s with respect to the BTB case. The single-channel capacity is further diminished in presence of the SOA, which lowers the OSNR, to 55.9 Gb/s. The addition of the HL3 aggregation

Distance	Configuration	Capacity
BTB	1 WSS (DEMUX)	68.3 Gb/s
	2 HL4 AWG, w/o SOA, 1 WSS	64.5 Gb/s
16 km	2 HL4 AWG, w/o SOA, 1 WSS	62.5 Gb/s
	HL4 node, 1 WSS	55.9 Gb/s
	HL4 node, 2 WSSs	54 Gb/s
116 km	Single channel	52.5 Gb/s
	3 25-GHz spaced channels	52.3 Gb/s

Table 5.3: Transmitted capacities with the setup shown in Figure 5.21.

25-GHz WSS causes a tight filtering due to the cascade of two 25-GHz WSSs, which limits the capacity to 54 Gb/s. In case of single-channel condition in the multi-hop configuration constituted of a HL4 ring, an add and a drop HL3 nodes, and an overall SSMF 116-km propagation, a capacity of 52.5 Gb/s can be reached. This limited capacity reduction with respect to the 16-km propagation is due to the CD compensation performed off-line. At last, a capacity of 52.3 Gb/s can be achieved in presence of three 25-GHz spaced channels. The 3rd order Volterra equalizer lessens the penalty to 1.7 Gb/s with respect to 16-km single-channel propagation and to only 200 Mb/s with respect to 116-km single-channel propagation.

Conclusions

In the next years, future Metropolitan Area Networks (MANs) will have to support a large range of resource-hungry applications and cope with requirements in terms of reduction of costs, energy consumption, and footprint. Several solutions to increase the transmission rates are proposed in these years. Some of them imply the exploitation of high modulation formats, up to 256-QAM, for single-channel transmission in the C-band, demonstrating up to 600 Gb/s for a 100 km Standard Single-Mode Fiber (SSMF) propagation. Other works propose the extension of the transmission band to the S-band and the L-band and multichannel transmission, where ultra-wide amplification is performed with Semiconductor Optical Amplifiers (SOAs). A capacity of 115.9 Tb/s has been demonstrated for 250 Probabilistically-Shaped 64-QAM (PS64QAM) channels for 100-km SSMF propagation.

The solution described in this thesis, developed in PASSION project, consists in the transmission of up to 160 25-GHz spaced channels in the C-band in the range between 191.9 THz and 195.875 THz. A modular approach in the design of the transmitters and of the receivers, the Sliceable Bandwidth/Bitrate Variable Transceivers (S-BVTs), provides flexibility and adaptability to the network conditions. The source constituting each Submodule of the transmitting part of the S-BVT is the Vertical-Cavity Surface-Emitting Laser (VCSEL), which is directly modulated with Discrete Multitone (DMT) signals. Thanks to its multicarrier nature, DMT allows to optimize the signal bandwidth depending on the conditions of the channel, giving more flexibility to the transmission.

The MAN network has a hierarchical topology, from an user-centered zone to the national backbone. The focus is put on the intermediate Hierarchical Levels (HLs), the HL4 and HL3 nodes. The channels which are added, dropped or which cross an HL4 node are 50-GHz spaced. The channel selection is performed by an array of SOAs. The dropped channels are forwarded to the lower HL5 nodes, which interface with the users. The forwarded channels are instead destined to other HL4 or to HL3 nodes. The HL3 nodes are structured to manage 25-GHz spaced channels, which are again selected with SOA-based wavelength blockers. In order to further increase the transmission rate, Space Division Multiplexing (SDM) can be employed by exploiting a bundle of fibers or MultiCore Fibers (MCFs). A brief introduction on MCFs, their Intercore Crosstalk (ICXT) and some multiplexing devices have been presented, but the system evaluations have been performed with Standard Single-Mode Fiber (SSMF) spans. Since MAN networks cover distances in the order of hundreds of km, the accumulated Chromatic Dispersion (CD) heavily impairs the performance. This is the reason why Coherent Detection (COH-D) is preferred to Direct Detection (DD): the signal field recovery allows to compensate for the CD by Digital Signal Processing (DSP). Some algorithms which can be applied to off-line postprocess the signal have been presented.

For this thesis a simulation tool has been developed. Each VCSEL is modelled with its electro-optical bandwidth, its chirp parameters, and its lineshape. The bit- and power-loading alogirthms are applied to the DMT signal to optimize the transmission bandwidth. The nonlinear impairments introduced by fiber propagation, due to the *Kerr effect*, are emulated with Non-Linear Schrödinger Equations (NLSEs), when the fiber birefringence is neglected, and with Coupled Non-Linear Schrödinger Equations (CNLSEs) otherwise. The simulation of the fiber propagation has been then validated with a commercial simulation tool, showing a very good agreement. In order to recover the transmitted power, an Erbium-Doped Fiber Amplifier (EDFA)

is placed after each fiber span. The noise contribution of all the EDFAs is introduced as an Additive White Gaussian Noise (AWGN) by computing the overall Optical Signal-to-Noise Ratio (OSNR) arising from the cascade of all the amplifiers OSNRs. The network nodes are emulated considering only the Tranfer Functions (TFs) of the Multiplexers (MUXs) and Demultiplexers (DEMUXs), neglecting the presence of the SOAs. A particular focus is put on the Wavelength Selective Switch (WSS), chosen for the channel interleaving part for its steepness. Anyway, the Waveshaper used to emulate the theoretical WSS TF is not able to perfectly follow the steepness, and the result is a filter which is characterized by a lower bandwidth and extinction ratio. In this work, a simplified Coherent Receiver (COH-RX) is employed: *simplified* means that after the compensation of CD, the squared modulus of the signal is performed. In this way the signal is just intensity modulated, and this avoids to recover phase and frequency.

In order to validate the complete simulator, a set of experimental measurements has been arranged. The measurements imply the crossing of 1, 3, and 5 25-GHz spacing WSS filters for OSNR values of 30 dB, 35 dB, and 40 dB, direct modulation of a 18-GHz VCSEL and SSB DMT modulation (one of the WSS is employed to perform SSB filtering). The target 50 Gb/s can be achieved for up to 5 WSS filters and 30-dB OSNR. By inverting the formula to compute the OSNR for equally-spaced spans, a reach of 260 km can be achieved for 65-km span length, and 735 km for 35-km span length. The interplay between optical filtering and chirp parameters has been investigated for the same OSNR values and number of 25-GHz WSS filters with three different sources: a 20-GHz short-cavity Directly-Modulated (DM) VCSEL, an 8-GHz tunable VCSEL, and a CW 500-kHz followed by an Electro-absorption Modulated Laser (EML). The chirp parameters of the two VCSELs have been measured by exploiting the uncompensated TF of the channel in presence of several distances propagation (10 km, 24 km, and 34 km), and the short-cavity source has resulted to be

a worse device with respect to the tunable one in terms of chirp parameters. The comparison among the sources have been performed for both DSB and SSB DMT modulation, resulting in the tunable VCSEL outperforming the short-cavity laser. The target capacity of 50 Gb/s is again achieved for both the VCSELs at 30-dB OSNR for SSB DMT modulation. DSB is instead heavily impaired by the interplay between chirp and tight filtering, which causes an average reduction of the transmitted capacity around 45%. All these results have been obtained for a single-channel transmission. An evaluation of the interchannel crosstalk has been performed for three 25-GHz spaced channels modulated with a 16-GHz and a 20-GHz SSB DMT signals, and the transmitted capacities have been compared with the ones achieved with single-channel transmission. When the channels are modulated with the smaller bandwidth signal, they suffer less from the interchannel crosstalk than with the wider one. Moreover, filtering the signal three times appears to be the best solution, since with two filters the interchannel crosstalk has a more significant impact, while a higher number of filters suppress the useful components of the signal. The HL4 and HL3 nodes have been deployed to evaluate the minimum OSNRs required by the network to achieve a given target capacity (25 Gb/s, 40 Gb/s, and 50 Gb/s). For this purpose, every possible combination of 11 or less nodes has been investigated in presence of only linear effects in the fiber propagation. The impact of HL3 nodes in the performance is more significant than the effect of HL4 nodes, due to the tight filtering. When many of them are cascaded, part of the useful signal is suppressed, leading to higher requirements in OSNR to achieve a given target capacity. The values of required OSNRs have been achieved with linear propagation, so, in order to be applied to a real network, a margin should be taken. With this evaluation in mind, some network topologies have been evaluated by measuring the transmitted capacity for an optimized launch optical power and setting up different EDFA distributions along the network. A network composed of 2 HL4 nodes, 6 HL3 nodes (with

only 2 "active" nodes and the other 4 in express path configuration), and 3 HL2/1 nodes (2 "active" nodes and the other in express path configuration) for 172-km SSMF propagation, a capacity of 51.19 Gb/s can be achieved with a launch power of 1 dBm, considering the effect of nonlinear impairments, and by aggregating some short spans together. A trade-off between the span length and the number of EDFAs to put in-line has to be found: if many short spans are cascaded, the accumulated nonlinear impairments, along with the noise introduced by many amplifiers, are detrimental for the performance, while few long spans cause a significant signal attenuation.

The SOA HL4 node crossing evaluation has been performed by experimental results. After having introduced the amplifier and having presented an interesting yet time-consuming algorithm to emulate the SOA transient behaviour, the employed polarization-insensitive SOA has been characterized in terms of its CW gain and TF for several bias currents and input powers. Then, the SOA response to DMT signal has been investigated. Two different sources have been employed: a DFB laser emitting at 1558 nm and a 1535-nm VCSEL. They have been modulated externally and directly respectively with both a DSB and an SSB 20-GHz electrical signal. In direct modulation, the effect of SOA high-pass filtering is more pronounced than in external modulation, with a reduction of 10 dB for low frequency subcarriers. On the other side, with external modulation of the optical signal, the amplifier introduces a Vestigial Sideband (VSB) filtering on the optical spectrum, which is more marked for high saturation conditions (*i.e.*, for high bias currents and input powers). When the VCSEL is directly modulated with a 20-GHz DSB DMT signal, the target capacity of 50 Gb/s is achieved for input powers higher than -8 dBm for bias currents higher than 150 mA and for powers higher than -6 dBm for 125 mA. In case of SSB modulation, the same target capacity can be achieved for input powers higher than -9 dBm, but a capacity reduction of only 8 Gb/s is faced when the input power is lowered by 5 dB, in the face of

a decrement of 13 Gb/s in the same power range for DSB modulation. The complete HL4 node crossing, including the presence of the SOA, has been evaluated for both single and three-channel transmission, for propagation lengths of 16 km (only single channel) and 116 km (both single and multichannel), and coherent detection. The introduction of the SOA in the HL4 node has caused a reduction of 6.5 Gb/s in the transmitted capacity, which, however, exceeds the target capacity of 50 Gb/s for 116-km SSMF propagation and three 25-GHz spaced channels, provided the exploitation of 3rd order Volterra equalizer to compensate for the fiber nonlinear impairments and the interchannel crosstalk.

This thesis has demonstrated that S-BVTs deployed in hierarchical MAN networks with several node architectures can guarantee at least 50 Gb/s per channel per polarization in almost all the analyzed scenarios, including real network topologies and also in presence of SOA-based nodes.

Further work will foresee the integration in MATLAB® simulator of a simplified SOA model consisting of the measured CW gain and of the TF retrieved with the Vector Network Analyzer (VNA). In order to achieve this objective, further measurements on Cross-Gain Modulation (XGM) will be performed for different channel spacings. Moreover, the emulation of the complete HL4 and HL3 nodes, along with the experimental results for hundred-km propagation presented in Section 4.4 which can give an indication on the required margin on the capacity in presence of nonlinear propagation, will refine the estimation of the required OSNR for given target capacities discussed in Section 4.5. Another interesting activity is the emulation of the propagation along spans of MultiCore Fiber (MCF). Some preliminary measurements on the time-dependence of Intercore Crosstalk (ICXT) have already been performed for both DSB and SSB DMT modulation.

Acronyms

AAG	Asia-America Gateway
ADC	Analog to Digital Converter
ADM	Add/Drop Multiplexer
ASE	Amplified Spontaneous Emission
AWG	Arrayed Waveguide Grating
AWGN	Additive White Gaussian Noise
BER	Bit Error Rate
BS	Base Station
BTB	Back-to-Back
BTJ	Buried Tunnel Junction
CAGR	Compound Annual Growth Rate
CD	Chromatic Dispersion
CNLSE	Coupled Non-Linear Schrödinger Equation
CO	Central Office
COH-D	Coherent Detection
COH-RX	Coherent Receiver

CP	Cyclic Prefix
CPE	Customer Premises Equipment
CRZ	Chirped Return-to-Zero
CSPR	Carrier to Signal Power Ratio
CUT	Channel Under Test
CW	Continuous Wave
DAC	Digital to Analog Converter
DBR	Distributed Bragg Reflector
DC	Direct Current
DD	Direct Detection
DEMUX	Demultiplexing
DFB	Distributed FeedBack
DM	Direct Modulation
DML	Directly Modulated Laser
DMT	Discrete Multitone
DSB	Dual Sideband
DSLAM	Digital Subscriber Line Access Multiplexer
DSP	Digital Signal Processing
DWDM	Dense Wavelength Division Multiplexing
EAM	Electro-Absorption Modulator

EDFA	Erbium-Doped Fiber Amplifier
EML	Electro-absorption Modulated Laser
EPON	Ethernet Passive Optical Network
ER	Extinction Ratio
EVM	Error Vector Magnitude
E/O	Electro-optic
FEC	Forward Error Correction
FFT	Fast Fourier Transform
FIR	Finite Impulse Response
FM-MCF	Few-Mode Multicore Fiber
FFTX	Fiber to the x
FWHM	Full Width Half Maximum
FWM	Four-Wave Mixing
GVD	Group Velocity Dispersion
HL	Hierarchical Level
ICXT	Intercore Crosstalk
IEEE	Institute of Electrical and Electronics Engineers
IFFT	Inverse Fast Fourier Transform
IIR	Infinite Impulse Response
IL	Insertion Loss

IM	Intensity-Modulated
IP	Internet Protocol
IP/MPLS	Internet Protocol over MultiProtocol Label Switching
IQ	In-phase and Quadrature
ISI	InterSymbol Interference
ISP	Internet Service Provider
ITU	International Telecommunication Union
LCoS	Liquid Crystal on Silicon
LCP	Local Connection Point
LO	Local Oscillator
LPF	Low-Pass Filter
MAN	Metropolitan Area Network
MCF	MultiCore Fiber
MEMS	Micro Electro-Mechanical Systems
MM-MCF	Multimode Multicore Fiber
MUX	Multiplexing
MZ	Mach-Zehnder
NEC	Noise Equivalent Current
NF	Noise Figure
NIU	Network Interface Unit

NLSE	Non-Linear Schrödinger Equation
NRZ	Non-Return to Zero
OFDM	Orthogonal Frequency Division Multiplexing
OLT	Optical Line Termination
ONT	Optical Network Terminal
OOK	On-Off Keying
OSA	Optical Spectrum Analyser
OSNR	Optical Signal-to-Noise Ratio
OTF	Optical Transfer Function
OTN	Optical Transport Network
O/E	Opto-electronic
PAM	Pulse Amplitude Modulation
PAPR	Peak-to-Average Power Ratio
PBS	Polarization Beam Splitter
PDM	Polarization Division Multiplexing
PD	Photodiode
PIC	Photonic Integrated Circuit
PIN	Positive-Intrinsic-Negative
PM	Polarization Multiplexed
PMD	Polarization Mode Dispersion

PMF	Polarization Maintaining Fiber
PMP	Phase-Matching Points
PON	Passive Optical Network
POP	Point of Presence
PRBS	Pseudo-Random Binary Sequence
PS	Photonic Switch
PS64QAM	Probabilistically-Shaped 64-QAM
QAM	Quadrature Division Multiplexing
QPSK	Quadrature Phase Shift Keying
RF	Radio Frequency
ROADM	Reconfigurable Optical Add-Drop Multiplexer
RX	Receiver
RZ	Return-to-Zero
SOA	Semiconductor Optical Amplifier
SDM	Space Division Multiplexing
SDN	Software Defined Network
SER	Symbol Error Rate
SGM	Self-Gain Modulation
SiPh	Silicon-Photonics
SM-MCF	Single Mode Multicore Fiber

SNR	Signal to Noise Ratio
SOI	Silicon-on-Insulator
SOP	State of Polarization
SPM	Self-Phase Modulation
SSB	Single Sideband
SSBI	Signal-Signal Beating Interference
SSE	Sum of Squared estimate of Errors
SSMF	Standard Single-Mode Fiber
S-BVT	Sliceable Bandwidth/Bitrate Variable Transceiver
S-BVRx	Sliceable Bandwidth Variable Receiver
S-BVTx	Sliceable Bandwidth Variable Transmitter
TA-MCF	Trench-Assisted Multicore Fiber
TE	Transverse Electric
TF	Transfer Function
TM	Transverse Magnetic
TX	Transmitter
UHD	UltraHigh Definition
UWB	Ultra-Wideband
VOA	Variable Optical Attenuator
VCSEL	Vertical-Cavity Surface-Emitting Laser

VNA	Vector Network Analyzer
VSB	Vestigial Sideband
WBL	Wavelength Blocker
WDM	Wavelength Division Multiplexing
WSS	Wavelength Selective Switch
XGM	Cross-Gain Modulation
XPM	Cross-Phase Modulation

List of Figures

List of Tables

Bibliography

[1] Cisco Global Cloud Index. "Forecast and methodology, 2015-2020 white paper". In: *Retrieved 1st June* (2016), p. 15.

[2] statista. *Data volume of global consumer internet traffic from 2017 to 2022, by subsegment*. 2019. URL: https://www.statista.com/statistics/267194/forecast-of-internet-traffic-by-subsegment/.

[3] Nasir Ghani, Jin-Yi Pan, and Xin Cheng. "Metropolitan optical networks". In: *Optical Fiber Telecommunications IV-B*. Elsevier, 2002, pp. 329–403.

[4] Rajiv Ramaswami, Kumar Sivarajan, and Galen Sasaki. "CHAPTER 11 - Access Networks". In: *Optical networks: a practical perspective*. Ed. by Jennifer Mann. Burlington: Morgan Kaufmann, 2010, pp. 629–652. ISBN: 978-0-12-374092-2.

[5] Tomas Horvath, Petr Munster, Vaclav Oujezsky, et al. "Passive Optical Networks Progress: A Tutorial". In: *Electronics* 9.7 (2020), pp. 1–31.

[6] Dezhi Zhang, Dekun Liu, Xuming Wu, et al. "Progress of ITU-T higher speed passive optical network (50G-PON) standardization". In: *Journal of Optical Communications and Networking* 12.10 (2020), pp. D99–D108.

[7] Jun Shan Wey. "The outlook for PON standardization: a tutorial". In: *Journal of Lightwave Technology* 38.1 (2020), pp. 31–42.

[8] Biswanath Mukherjee, Ioannis Tomkos, Massimo Tornatore, et al. "CHAPTER 18 - Metropolitan Networks". In: *Springer Handbook of Optical Networks*. Ed. by Biswanath Mukherjee, Ioannis Tomkos, Massimo Tornatore, et al. Gewerbestrasse 11, 6330 Cham, Switzerland: Springer Nature, 2020, pp. 609–630. ISBN: 978-3-030-16249-8.

[9] Biswanath Mukherjee, Ioannis Tomkos, Massimo Tornatore, et al. "CHAPTER 11 - Carrier Network Architectures and Resiliency". In: *Springer Handbook of Optical Networks*. Ed. by Biswanath Mukherjee, Ioannis Tomkos, Massimo Tornatore, et al. Gewerbestrasse 11, 6330 Cham, Switzerland: Springer Nature, 2020, pp. 399–446. ISBN: 978-3-030-16249-8.

[10] Rajiv Ramaswami, Kumar Sivarajan, and Galen Sasaki. "CHAPTER 13 - Deployment Considerations". In: *Optical networks: a practical perspective*. Ed. by Jennifer Mann. Burlington: Morgan Kaufmann, 2010, pp. 707–738. ISBN: 978-0-12-374092-2.

[11] Submarine Cable Networks. *Trans-Pacific*. 2020. URL: `https://www.submarinenetworks.com/en`.

[12] Jane M. Simmons. "On determining the optimal optical reach for a long-haul network". In: *Journal of Lightwave Technology* 23.3 (2005), p. 1039.

[13] Xiang Zhou, Lynn E Nelson, and Peter Magill. "Rate-adaptable optics for next generation long-haul transport networks". In: *IEEE Communications Magazine* 51.3 (2013), pp. 41–49.

[14] I Haxell, M Ding, A Akhtar, et al. "52× 12.3 Gbit/s DWDM transmission over 3600km of True Wave fiber with 100km amplifier spans". In: *Optical Amplifiers and Their Applications*. Optical Society of America. 2000, OTuC7.

[15] Bamdad Bakhshi, M Vaa, EA Golovchenko, et al. "Comparison of CRZ, RZ and NRZ modulation formats in a 64/spl times/12.3 Gb/s WDM transmission experiment over 9000 km". In: *OFC 2001. Optical Fiber Communication Conference and Exhibit. Technical Digest Postconference Edition (IEEE Cat. 01CH37171)*. Vol. 3. IEEE. 2001, WF4–WF4.

[16] Biswanath Mukherjee, Ioannis Tomkos, Massimo Tornatore, et al. "CHAPTER 21 - Evolving Requirements and Trends in Datacenter Networks". In: *Springer Handbook of Optical Networks*. Ed. by Biswanath Mukherjee, Ioannis Tomkos, Massimo Tornatore, et al. Gewerbestrasse 11, 6330 Cham, Switzerland: Springer Nature, 2020, pp. 709–722. ISBN: 978-3-030-16249-8.

[17] Jiachuan Lin, Hassan Sepehrian, Leslie A. Rusch, et al. "Joint digital and optical pre-compensation for 720 Gb/s all-silicon IQ modulator single carrier transmission". In: *2018 European Conference on Optical Communication (ECOC)*. IEEE. 2018, pp. 1–3.

[18] Michael Hochberg, Nicholas C. Harris, Ran Ding, et al. "Silicon photonics: the next fabless semiconductor industry". In: *IEEE Solid-State Circuits Magazine* 5.1 (2013), pp. 48–58.

[19] Jeremie Renaudier. "Recent advances in ultra-wideband WDM transmission based on semiconductor optical amplifiers". In: *Optical Fiber Communication Conference*. Optical Society of America. 2019, Tu3F.5.

[20] Christopher Doerr and Long Chen. "Silicon photonics in optical coherent systems". In: *Proceedings of the IEEE* 106.12 (2018), pp. 2291–2301.

[21] Biljana Milivojevic, Stefan Wiese, Sean Anderson, et al. "Demonstration of optical transmission at bit rates of up to 321.4 Gb/s using compact silicon based modulator and linear BiCMOS MZM driver". In: *Journal of Lightwave Technology* 35.4 (2016), pp. 768–774.

[22] Li Chen, Chris Doerr, Ricardo Aroca, et al. "Silicon photonics for 100G-and-beyond coherent transmissions". In: *Optical Fiber Communication Conference*. Optical Society of America. 2016, Th1B.1.

[23] Chi Yan Wong, Sen Zhang, Yuanyuan Fang, et al. "Silicon IQ modulator for next-generation metro network". In: *Journal of Lightwave Technology* 34.2 (2016), pp. 730–736.

[24] Asuka Matsushita, Masanori Nakamura, Fukutaro Hamaoka, et al. "High-spectral-efficiency 600-Gbps/carrier transmission using PDM-256QAM format". In: *Journal of Lightwave Technology* 37.2 (2018), pp. 470–476.

[25] Jeremie Renaudier, Aymeric Arnould, Amirhossein Ghazisaeidi, et al. "Recent Advances in 100+nm Ultra-Wideband Fiber-Optic Transmission Systems Using Semiconductor Optical Amplifiers". In: *Journal of Lightwave Technology* 38.5 (2020), pp. 1071–1079. DOI: 10.1109/JLT.2020.2966491.

[26] Jeremie Renaudier and Amirhossein Ghazisaeidi. "Scaling capacity growth of fiber-optic transmission systems using 100+ nm ultra-wideband semiconductor optical amplifiers". In: *Journal of Lightwave Technology* 37.8 (2019), pp. 1831–1838.

[27] Aymeric Arnould, David Le Gac, Amirhossein Ghazisaeidi, et al. "Impact of the number of channels on the induced nonlinear distortions in ultra-wideband SOAs". In: *Optical Fiber Communication Conference*. Optical Society of America. 2019, Tu3F.1.

[28] Georg Böcherer, Patrick Schulte, and Fabian Steiner. "Probabilistic shaping and forward error correction for fiber-optic communication systems". In: *Journal of Lightwave Technology* 37.2 (2019), pp. 230–244.

[29] Fukutaro Hamaoka, Masanori Nakamura, Seiji Okamoto, et al. "Ultra-wideband WDM transmission in S-, C-, and L-bands using signal power optimization scheme". In: *Journal of Lightwave Technology* 37.8 (2019), pp. 1764–1771.

[30] Jiawei Meng, Mario Miscuglio, Jonathan K. George, et al. "Electronic Bottleneck Suppression in Next-generation Networks with Integrated Photonic Digital-to-analog Converters". In: *arXiv preprint arXiv:1911.02511* (2019), pp. 1–12.

[31] EU H2020 PASSION project. *D 2.2: Overall network architecture and control aspects definition*. Tech. rep. 2020.

[32] EU H2020 PASSION project. *D 2.1: Definition of the use cases for network, systems and subsystems*. Tech. rep. 2018.

[33] Michela Svaluto Moreolo, Josep M. Fabrega, Laia Nadal, et al. "SDN-enabled sliceable BVT based on multicarrier technology for multiflow rate/distance and grid adaptation". In: *Journal of Lightwave Technology* 34.6 (2016), pp. 1516–1522.

[34] "13 - Low-Dimensional Quantum Systems". In: *Quantum Mechanics with Applications to Nanotechnology and Information Science*. Ed. by Yehuda B. Band and Yshai Avishai. Amsterdam: Academic Press, 2013, pp. 749–823. ISBN: 978-0-444-53786-7. DOI: 10.1016/B978-0-444-53786-7.00013-7.

[35] Shyh Wang. "Principles of distributed feedback and distributed Bragg-reflector lasers". In: *IEEE Journal of Quantum Electronics* 10.4 (1974), pp. 413–427.

[36] Francesco De Leonardis, Francesca Magno, Alessandro Rizzato, et al. "Accurate modelling of VCSEL distributed Bragg reflectors by Floquet-Bloch theory". In: *Semiconductor Lasers and Laser Dynamics*

II. Vol. 6184. International Society for Optics and Photonics. 2006, pp. 618422-1–618422-11.

[37] Nur Ismail, Cristine Calil Kores, Dimitri Geskus, et al. "Fabry-Pérot resonator: spectral line shapes, generic and related Airy distributions, linewidths, finesses, and performance at low or frequency-dependent reflectivity". In: *Optics express* 24.15 (2016), pp. 16366–16389.

[38] John Michael Dallesasse, Nick Holonyak Jr, Alan R. Sugg, et al. "Hydrolyzation oxidation of Al x Ga1- x As-AlAs-GaAs quantum well heterostructures and superlattices". In: *Applied Physics Letters* 57.26 (1990), pp. 2844–2846.

[39] Kent D. Choquette, Richard P. Schneider, Kevin L. Lear, et al. "Low threshold voltage vertical-cavity lasers fabricated by selective oxidation". In: *Electronics Letters* 30.24 (1994), pp. 2043–2044.

[40] R.S. Geels, S.W. Corzine, J.W. Scott, et al. "Low threshold planarized vertical-cavity surface-emitting lasers". In: *Optical Fiber Communication Conference*. Optical Society of America. 1990, PD31.

[41] Meir Orenstein, Anne C. Von Lehmen, Connie Chang-Hasnain, et al. "Vertical-cavity surface-emitting InGaAs/GaAs lasers with planar lateral definition". In: *Applied physics letters* 56.24 (1990), pp. 2384–2386.

[42] Werner Hofmann. "High-speed buried tunnel junction vertical-cavity surface-emitting lasers". In: *IEEE Photonics Journal* 2.5 (2010), pp. 802–815.

[43] Diana L. Huffaker, Dennis G. Deppe, Krishna Kumar, et al. "Native-oxide defined ring contact for low threshold vertical-cavity lasers". In: *Applied Physics Letters* 65.1 (1994), pp. 97–99.

[44] Manfred Grabherr, Roland Jäger, Michael Miller, et al. "Bottom-emitting VCSEL's for high-CW optical output power". In: *IEEE Photonics Technology Letters* 10.8 (1998), pp. 1061–1063.

[45] Rainer Michalzik and Karl Joachim Ebeling. "Operating principles of VCSELs". In: *Vertical-Cavity Surface-Emitting Laser Devices*. Springer, 2003, pp. 53–98.

[46] Fotini Karinou, Nebojsa Stojanovic, Aidan Daly, et al. "1.55-μm long-wavelength VCSEL-based optical interconnects for short-reach networks". In: *Journal of Lightwave Technology* 34.12 (2016), pp. 2897–2904.

[47] Jeffrey Lee. "Discrete multitone modulation for short-range optical communications". In: *Eindhoven: Technische Universiteit Eindhoven* (2009).

[48] William Shieh and Ivan Djordjevic. "Chapter 2 - OFDM Principles". In: *OFDM for Optical Communications*. Ed. by William Shieh and Ivan Djordjevic. Oxford: Academic Press, 2010, pp. 31–52. ISBN: 978-0-12-374879-9. DOI: https://doi.org/10.1016/B978-0-12-374879-9.00002-2.

[49] Jean Armstrong. "OFDM for optical communications". In: *Journal of Lightwave Technology* 27.3 (2009), pp. 189–204.

[50] Henrik V. Sorensen, Douglas L. Jones, Michael T. Heideman, et al. "Real-valued fast Fourier transform algorithms". In: *IEEE Transactions on acoustics, speech, and signal processing* 35.6 (1987), pp. 849–863.

[51] Pierpaolo Boffi, Paola Parolari, Alberto Gatto, et al. "Multi-Tb/s sustainable MAN scenario enabled by VCSEL-based innovative technological solutions". In: *Metro and Data Center Optical Networks and Short-Reach Links III*. Vol. 11308. International Society for Optics and Photonics. 2020, 113080G.

[52] David Larrabeiti, Juan Fernández-Palacios, Gabriel Otero, et al. "All-optical paths across multiple hierarchical levels in large metropolitan area networks". In: *2019 Asia Communications and Photonics Conference (ACP)*. IEEE. 2019, pp. 1–3.

[53] Kristif Prifti, Xuwei Xue, Netsanet Tessema, et al. "Lossless Photonic Integrated Add-Drop Switch Node for Metro-Access Networks". In: *IEEE Photonics Technology Letters* 32.7 (2020), pp. 387–390.

[54] Nicola Calabretta, Kristif Prifti, Netsanet Tessema, et al. "Photonic integrated WDM cross-connects for optical metro and data center networks". In: *Metro and Data Center Optical Networks and Short-Reach Links II*. Vol. 10946. International Society for Optics and Photonics. 2019, p. 1094603.

[55] Takayuki Mizuno, Kohki Shibahara, Feihong Ye, et al. "Long-haul dense space-division multiplexed transmission over low-crosstalk heterogeneous 32-core transmission line using a partial recirculating loop system". In: *Journal of Lightwave Technology* 35.3 (2017), pp. 488–498.

[56] Kunimasa Saitoh, Masanori Koshiba, Katsuhiro Takenaga, et al. "Homogeneous and heterogeneous multi-core fibers". In: *2012 IEEE Photonics Society Summer Topical Meeting Series*. IEEE. 2012, pp. 210–211.

[57] Masanori Koshiba, Kunimasa Saitoh, and Yasuo Kokubun. "Heterogeneous multi-core fibers: proposal and design principle". In: *IEICE Electronics Express* 6.2 (2009), pp. 98–103.

[58] Roland Ryf, Nicolas K. Fontaine, Steffen Wittek, et al. "High-spectral-efficiency mode-multiplexed transmission over graded-index multimode fiber". In: *2018 European Conference on Optical Communication (ECOC)*. IEEE. 2018, pp. 1–3.

[59] Daiki Soma, Yuta Wakayama, Shohei Beppu, et al. "10.16-Peta-B/s dense SDM/WDM transmission over 6-mode 19-core fiber across the C+ L band". In: *Journal of Lightwave Technology* 36.6 (2018), pp. 1362–1368.

[60] Georg Rademacher, Ruben S. Luís, Benjamin J. Puttnam, et al. "Crosstalk dynamics in multi-core fibers". In: *Optics express* 25.10 (2017), pp. 12020–12028.

[61] Tetsuya Hayashi, Toshiki Taru, Osamu Shimakawa, et al. "Characterization of crosstalk in ultra-low-crosstalk multi-core fiber". In: *Journal of Lightwave Technology* 30.4 (2011), pp. 583–589.

[62] Tetsuya Hayashi, Toshiki Taru, Osamu Shimakawa, et al. "Uncoupled multi-core fiber enhancing signal-to-noise ratio". In: *Optics express* 20.26 (2012), B94–B103.

[63] Katsuhiro Takenaga, Yoko Arakawa, Shoji Tanigawa, et al. "An investigation on crosstalk in multi-core fibers by introducing random fluctuation along longitudinal direction". In: *IEICE transactions on communications* 94.2 (2011), pp. 409–416.

[64] Ruben S. Luís, Benjamin J. Puttnam, Adolfo V.T. Cartaxo, et al. "Time and modulation frequency dependence of crosstalk in homogeneous multi-core fibers". In: *Journal of Lightwave Technology* 34.2 (2015), pp. 441–447.

[65] Benjamin J. Puttnam, Ruben S. Luís, Georg Rademacher, et al. "Characteristics of homogeneous multi-core fibers for SDM transmission". In: *APL Photonics* 4.2 (2019), pp. 022804-1–022804-10.

[66] Feihong Ye, Jiajing Tu, Kunimasa Saitoh, et al. "Wavelength-dependence of inter-core crosstalk in homogeneous multi-core fibers". In: *IEEE Photonics Technology Letters* 28.1 (2015), pp. 27–30.

[67] Tiago M.F. Alves, Ruben S. Luís, Benjamin J. Puttnam, et al. "Performance of adaptive DD-OFDM multicore fiber links and its relation with intercore crosstalk". In: *Optics Express* 25.14 (2017), pp. 16017–16027.

[68] Benjamin J. Puttnam, Ruben S. Luís, Erik Agrell, et al. "High capacity transmission systems using homogeneous multi-core fibers". In: *Journal of Lightwave Technology* 35.6 (2017), pp. 1157–1167.

[69] Tetsuya Hayashi, Tetsuya Nakanishi, Fumiaki Sato, et al. "Characterization of interconnect multi-core fiber cable: Mechanical/thermal characteristics and inter-core crosstalk of the straightened cable". In: *2016 IEEE Optical Interconnects Conference (OI)*. IEEE. 2016, pp. 92–93.

[70] Tetsuya Hayashi, Toshiki Taru, Osamu Shimakawa, et al. "Design and fabrication of ultra-low crosstalk and low-loss multi-core fiber". In: *Optics express* 19.17 (2011), pp. 16576–16592.

[71] Werner Klaus, Jun Sakaguchi, Benjamin J. Puttnam, et al. "Free-space coupling optics for multicore fibers". In: *IEEE Photonics Technology Letters* 24.21 (2012), pp. 1902–1905.

[72] Hidehiko Takara, Akihide Sano, Takayuki Kobayashi, et al. "1.01-Pb/s (12 SDM/222 WDM/456 Gb/s) crosstalk-managed transmission with 91.4-b/s/Hz aggregate spectral efficiency". In: *2012 European Conference and Exhibition on Optical Communication*. Optical Society of America. 2012, Th.3.C.1.

[73] Lin Gan, Jiajun Zhou, Li Shen, et al. "Ultra-low crosstalk fused taper type fan-in/fan-out devices for multicore fibers". In: *2019 Optical Fiber Communications Conference and Exhibition (OFC)*. IEEE. 2019, pp. 1–3.

[74] Benyuan Zhu, Thierry F. Taunay, Man F. Yan, et al. "Seven-core multicore fiber transmissions for passive optical network". In: *Optics Express* 18.11 (2010), pp. 11117–11122.

[75] Robert R. Thomson, Henry T. Bookey, Nicholas D. Psaila, et al. "Ultrafast-laser inscription of a three dimensional fan-out device for multicore fiber coupling applications". In: *Optics express* 15.18 (2007), pp. 11691–11697.

[76] Kazuro Kikuchi. "Fundamentals of coherent optical fiber communications". In: *Journal of Lightwave Technology* 34.1 (2015), pp. 157–179.

[77] Ezra Ip, Alan Pak Tao Lau, Daniel J.F. Barros, et al. "Coherent detection in optical fiber systems". In: *Optics express* 16.2 (2008), pp. 753–791.

[78] T. G. Hodgkinson, R.A. Harmon, and D.W. Smith. "Demodulation of optical DPSK using in-phase and quadrature detection". In: *Electronics Letters* 21.19 (1985), pp. 867–868.

[79] Xiaofei Lu and Xi-Cheng Zhang. "Balanced terahertz wave air-biased-coherent-detection". In: *Applied Physics Letters* 98.15 (2011), p. 151111.

[80] Anthony Davis, Martin Pettitt, Jonathan King, et al. "Phase diversity techniques for coherent optical receivers". In: *Journal of Lightwave Technology* 5.4 (1987), pp. 561–572.

[81] Satoshi Tsukamoto, Yuta Ishikawa, and Kazuro Kikuchi. "Optical homodyne receiver comprising phase and polarization diversities with digital signal processing". In: *2006 European Conference on Optical Communications*. IEEE. 2006, pp. 1–2.

[82] Erik Agrell and Magnus Karlsson. "Power-efficient modulation formats in coherent transmission systems". In: *Journal of Lightwave Technology* 27.22 (2009), pp. 5115–5126.

[83] Timo Pfau, Sebastian Hoffmann, and Reinhold Noé. "Hardware-efficient coherent digital receiver concept with feedforward carrier recovery for M-QAM constellations". In: *Journal of Lightwave Technology* 27.8 (2009), pp. 989–999.

[84] Michela Svaluto Moreolo, Laia Nadal, Josep M. Fabrega, et al. "Modular SDN-enabled S-BVT adopting widely tunable MEMS VCSEL for flexible/elastic optical metro networks". In: *2018 Optical Fiber Communications Conference and Exposition (OFC)*. IEEE. 2018, pp. 1–3.

[85] Seb J. Savory. "Digital coherent optical receivers: Algorithms and subsystems". In: *IEEE Journal of selected topics in quantum electronics* 16.5 (2010), pp. 1164–1179.

[86] Maxim Kuschnerov, Fabian N. Hauske, Kittipong Piyawanno, et al. "DSP for coherent single-carrier receivers". In: *Journal of Lightwave Technology* 27.16 (2009), pp. 3614–3622.

[87] Takahito Tanimura, Shoichiro Oda, Toshiki Tanaka, et al. "A simple digital skew compensator for coherent receiver". In: *2009 35th European Conference on Optical Communication*. IEEE. 2009, pp. 1–2.

[88] Paolo Prandoni and Martin Vetterli. "From Lagrange to Shannon... and back: another look at sampling [DSP Education]". In: *IEEE Signal Processing Magazine* 26.5 (2009), pp. 138–144.

[89] Irshaad Fatadin, Seb J. Savory, and David Ives. "Compensation of quadrature imbalance in an optical QPSK coherent receiver". In: *IEEE Photonics Technology Letters* 20.20 (2008), pp. 1733–1735.

[90] István Mayer. "On Löwdin's method of symmetric orthogonalization". In: *International Journal of Quantum Chemistry* 90.1 (2002), pp. 63–65.

[91] Tianhua Xu, Gunnar Jacobsen, Sergei Popov, et al. "Chromatic dispersion compensation in coherent transmission system using digital filters". In: *Optics express* 18.15 (2010), pp. 16243–16257.

[92] David S. Millar, Sergejs Makovejs, Carsten Behrens, et al. "Mitigation of fiber nonlinearity using a digital coherent receiver". In: *IEEE Journal of Selected Topics in Quantum Electronics* 16.5 (2010), pp. 1217–1226.

[93] John Tsimbinos and Kenneth V. Lever. "Computational complexity of Volterra based nonlinear compensators". In: *Electronics Letters* 32.9 (1996), pp. 852–854.

[94] Nikolaos-Panteleimon Diamantopoulos, Hidetaka Nishi, Wataru Kobayashi, et al. "On the complexity reduction of the second-order Volterra nonlinear equalizer for IM/DD systems". In: *Journal of Lightwave Technology* 37.4 (2019), pp. 1214–1224.

[95] Riccardo Raheli and Giorgio Picchi. "Synchronous and fractionally-spaced blind equalization in dually-polarized digital radio links". In: *ICC 91 International Conference on Communications Conference Record*. IEEE. 1991, pp. 156–161.

[96] Kazuro Kikuchi. "Polarization-demultiplexing algorithm in the digital coherent receiver". In: *2008 Digest of the IEEE/LEOS Summer Topical Meetings*. IEEE. 2008, pp. 101–102.

[97] Thierry Pollet and Miguel Peeters. "Synchronization with DMT modulation". In: *IEEE Communications Magazine* 37.4 (1999), pp. 80–86.

[98] Floyd Gardner. "A BPSK/QPSK timing-error detector for sampled receivers". In: *IEEE Transactions on communications* 34.5 (1986), pp. 423–429.

[99] Kurth Mueller and Markus Muller. "Timing recovery in digital synchronous data receivers". In: *IEEE transactions on communications* 24.5 (1976), pp. 516–531.

[100] Andreas Leven, Noriaki Kaneda, Ut-Va Koc, et al. "Frequency estimation in intradyne reception". In: *IEEE Photonics Technology Letters* 19.6 (2007), pp. 366–368.

[101] Sebastian Hoffmann, Suhas Bhandare, Timo Pfau, et al. "Frequency and phase estimation for coherent QPSK transmission with unlocked DFB lasers". In: *IEEE Photonics Technology Letters* 20.18 (2008), pp. 1569–1571.

[102] Mehrez Selmi, Yves Jaouen, and Philippe Ciblat. "Accurate digital frequency offset estimator for coherent PolMux QAM transmission systems". In: *2009 35th European Conference on Optical Communication*. IEEE. 2009, pp. 1–2.

[103] Oriol Bertran Pardo, Jérémie Renaudier, Haïk Mardoyan, et al. "Investigation of design options for overlaying 40Gb/s coherent PDM-QPSK channels over a 10Gb/s system infrastructure". In: *Optical Fiber Communication Conference*. Optical Society of America. 2008, OTuM5.

[104] Dirk Van Den Borne. "Robust optical transmission systems: modulation and equalization". In: (2008).

[105] Chongjin Xie, Silvia Spiga, Po Dong, et al. "400-Gb/s PDM-4PAM WDM system using a monolithic 2× 4 VCSEL array and coherent detection". In: *Journal of Lightwave Technology* 33.3 (2014), pp. 670–677.

[106] Rodney S. Tucker. "High-speed modulation of semiconductor lasers". In: *IEEE transactions on electron devices* 32.12 (1985), pp. 2572–2584.

[107] Silvia Spiga, Dean Schoke, Alexander Andrejew, et al. "Effect of cavity length, strain, and mesa capacitance on 1.5-μm VCSELs performance". In: *Journal of Lightwave Technology* 35.15 (2017), pp. 3130–3141.

[108] Ahmad N. Al-Omari, I.K. Al-Kofahi, and Kevin L. Lear. "Fabrication, performance and parasitic parameter extraction of 850 nm high-speed vertical-cavity lasers". In: *Semiconductor science and technology* 24.9 (2009), pp. 1–9.

[109] Ikuo Suemune. "Theoretical study of differential gain in strained quantum well structures". In: *IEEE Journal of Quantum Electronics* 27.5 (1991), pp. 1149–1159.

[110] Michael Muller, Werner Hofmann, Tobias Grundl, et al. "1550-nm high-speed short-cavity VCSELs". In: *IEEE Journal of selected topics in Quantum Electronics* 17.5 (2011), pp. 1158–1166.

[111] Thomas L. Koch and John E. Bowers. "Nature of wavelength chirping in directly modulated semiconductor lasers". In: *Electronics Letters* 20.25 (1984), pp. 1038–1040.

[112] Charles Henry. "Theory of the linewidth of semiconductor lasers". In: *IEEE Journal of Quantum Electronics* 18.2 (1982), pp. 259–264.

[113] Eva Peral, William K. Marshall, and Amnon Yariv. "Precise measurement of semiconductor laser chirp using effect of propagation in dispersive fiber and application to simulation of transmission through fiber gratings". In: *Journal of Lightwave Technology* 16.10 (1998), pp. 1874–1880.

[114] Luiz Anet Neto, Didier Erasme, Naveena Genay, et al. "Simple estimation of fiber dispersion and laser chirp parameters using the downhill simplex fitting algorithm". In: *Journal of Lightwave Technology* 31.2 (2012), pp. 334–342.

[115] Raghu C Srinivasan and John C. Cartledge. "On using fiber transfer functions to characterize laser chirp and fiber dispersion". In: *IEEE Photonics Technology Letters* 7.11 (1995), pp. 1327–1329.

[116] Philippe Gallion and Guy Debarge. "Quantum phase noise and field correlation in single frequency semiconductor laser systems". In: *IEEE Journal of Quantum Electronics* 20.4 (1984), pp. 343–349.

[117] Aditya Kakkar, Jaime Rodrigo Navarro, Richard Schatz, et al. "Laser frequency noise in coherent optical systems: spectral regimes and impairments". In: *Scientific reports* 7.1 (2017), pp. 1–10.

[118] Miguel Iglesias Olmedo, Xiaodan Pang, Richard Schatz, et al. "Effective linewidth of semiconductor lasers for coherent optical data links". In: *Photonics*. Vol. 3. 2. Multidisciplinary Digital Publishing Institute. 2016, pp. 1–10.

[119] Gianni Di Domenico, Stéphane Schilt, and Pierre Thomann. "Simple approach to the relation between laser frequency noise and laser line shape". In: *Applied optics* 49.25 (2010), pp. 4801–4807.

[120] Silvia Viciani, Mathias Gabrysch, Francesco Marin, et al. "Lineshape of a vertical cavity surface emitting laser". In: *Optics communications* 206.1-3 (2002), pp. 89–97.

[121] Ellis E. Whiting. "An empirical approximation to the Voigt profile". In: *Journal of Quantitative Spectroscopy and Radiative Transfer* 8.6 (1968), pp. 1379–1384.

[122] Hidenori Takahashi, Abdullah Al Amin, Sander L. Jansen, et al. "Highly Spectrally Efficient DWDM Transmission at 7.0 b/s/Hz Using 8 × 65.1-Gb/s Coherent PDM-OFDM". In: *Journal of Lightwave Technology* 28.4 (2009), pp. 406–414.

[123] Laia Nadal, Michela Svaluto Moreolo, Josep M. Fàbrega, et al. "DMT modulation with adaptive loading for high bit rate transmission over directly detected optical channels". In: *Journal of Lightwave Technology* 32.21 (2014), pp. 3541–3551.

[124] Laia Nadal, Michela Svaluto Moreolo, Josep M. Fàbrega, et al. "Clipping and quantization noise mitigation in intensity-modulated direct detection O-OFDM systems based on the FHT". In: *2012 14th International Conference on Transparent Optical Networks (ICTON)*. IEEE. 2012, pp. 1–4.

[125] Sebastian Randel, Florian Breyer, Sian C.J. Lee, et al. "Advanced modulation schemes for short-range optical communications". In: *IEEE Journal of Selected Topics in Quantum Electronics* 16.5 (2010), pp. 1280–1289.

[126] Chloé Milion, Thanh-Nga Duong, Naveena Genay, et al. "High bit rate transmission for NG-PON by direct modulation of DFB laser using discrete multi-tone". In: *2009 35th European Conference on Optical Communication*. IEEE. 2009, pp. 1–2.

[127] Peter S. Chow, John M. Cioffi, and John A.C. Bingham. "A practical discrete multitone transceiver loading algorithm for data transmission over spectrally shaped channels". In: *IEEE Transactions on communications* 43.2/3/4 (1995), pp. 773–775.

[128] Ana I. Pérez-Neira, Marc Realp Campalans, and co-authored by Dr. Stephen Pfletschinger. "Chapter 2 - Different views of spectral efficiency". In: *Cross-Layer Resource Allocation in Wireless Communications*. Ed. by Ana I. Pérez-Neira and Marc Realp Campalans. Oxford: Academic Press, 2009, pp. 13–33.

[129] Ana Garcia-Armada. "SNR gap approximation for M-PSK-based bit loading". In: *IEEE Transactions on Wireless Communications* 5.1 (2006), pp. 57–60.

[130] Simon A. Gebrewold. "Reflective Semiconductor Optical Amplifiers (RSOAs) as Colorless Sources in Access Networks". en. PhD thesis. Zürich: ETH Zurich, 2016. DOI: 10.3929/ethz-a-010781780.

[131] Fabrizio Forghieri, Robert W. Tkach, and Andrew R. Chraplyvy. "Chapter 8 - Fiber Nonlinearities and Their Impact on Transmission Systems". In: *Optical Fiber Telecommunications IIIA (Third Edition)*. Ed. by Ivan P. Kaminow and Thomas L. Koch. Third Edition. Boston: Academic Press, 1997, pp. 196–264. ISBN: 978-0-08-051316-4. DOI: https://doi.org/10.1016/B978-0-08-051316-4.50012-6.

[132] Raul Del Coso and Javier Solis. "Relation between nonlinear refractive index and third-order susceptibility in absorbing media". In: *JOSA B* 21.3 (2004), pp. 640–644.

[133] Mansoor Sheik-Bahae, Ali A. Said, and Eric W. Van Stryland. "High-sensitivity, single-beam n 2 measurements". In: *Optics letters* 14.17 (1989), pp. 955–957.

[134] Jiangwei Wang, Mansour Sheik-Bahae, AA Said, et al. "Time-resolved Z-scan measurements of optical nonlinearities". In: *JOSA B* 11.6 (1994), pp. 1009–1017.

[135] K.S. Kim, R.H. Stolen, W.A. Reed, et al. "Measurement of the nonlinear index of silica-core and dispersion-shifted fibers". In: *Optics letters* 19.4 (1994), pp. 257–259.

[136] RH Stolen and Chinlon Lin. "Self-phase-modulation in silica optical fibers". In: *Physical Review A* 17.4 (1978), p. 1448.

[137] Rongqing Hui and Maurice O'Sullivan. "Chapter 4 - Optical Fiber Measurement". In: *Fiber Optic Measurement Techniques*. Ed. by Rongqing Hui and Maurice O'Sullivan. Boston: Academic Press, 2009, pp. 365–479. ISBN: 978-0-12-373865-3. DOI: https://doi.org/10.1016/B978-0-12-373865-3.00004-5.

[138] Roger Stolen and John Bjorkholm. "Parametric amplification and frequency conversion in optical fibers". In: *IEEE Journal of Quantum Electronics* 18.7 (1982), pp. 1062–1072.

[139] Thomas Schneider. "Four-Wave-Mixing (FWM)". In: *Nonlinear Optics in Telecommunications*. Berlin, Heidelberg: Springer Berlin Heidelberg, 2004, pp. 167–200. ISBN: 978-3-662-08996-5. DOI: 10.1007/978-3-662-08996-5_7.

[140] Krishna Thyagarajan and Ajoy Ghatak. "CHAPTER 6 - Some Important Nonlinear Effects in Optical Fibers". In: *Guided Wave Optical Components and Devices*. Ed. by Bishnu P. Pal. Burlington: Academic Press, 2006, pp. 91–100. ISBN: 978-0-12-088481-0. DOI: https://doi.org/10.1016/B978-012088481-0/50007-3.

[141] Karsten Rottwitt and Peter Tidemand-Lichtenberg. *Nonlinear optics: principles and applications*. Vol. 3. CRC Press, 2014. ISBN: 978-981-10-1488-8. DOI: 10.1007/978-981-10-1488-8.

[142] Govind P Agrawal. "Nonlinear fiber optics". In: *Nonlinear Science at the Dawn of the 21st Century*. Springer, 2000, pp. 195–211.

[143] Le Nguyen Binh. *Optical fiber communication systems with Matlab and Simulink models*. CRC press, 2014. ISBN: 978-1482217513. DOI: https://doi.org/10.1201/b17781.

[144] Curtis R. Menyuk and Brian S. Marks. "Interaction of polarization mode dispersion and nonlinearity in optical fiber transmission systems". In: *Journal of Lightwave Technology* 24.7 (2006), p. 2806.

[145] JP Gordon and H Kogelnik. "PMD fundamentals: Polarization mode dispersion in optical fibers". In: *Proceedings of the National Academy of Sciences* 97.9 (2000), pp. 4541–4550.

[146] Alberto Bononi and Armando Vannucci. "Is there life beyond the principal states of polarization?" In: *Optical Fiber Technology* 8.4 (2002), pp. 257–294.

[147] Yoshiyuki Suetsugu, Takatoshi Kato, and Masayuki Nishimura. "Full characterization of polarization-mode dispersion with random-mode coupling in single-mode optical fibers". In: *IEEE Photonics Technology Letters* 7.8 (1995), pp. 887–889.

[148] Roderich Tumulka. "Pauli spin matrices". In: *Compendium of Quantum Physics*. Springer, 2009, pp. 470–472.

[149] Dietrich Marcuse, Curtis R. Manyuk, and P.K.A. Wai. "Application of the Manakov-PMD equation to studies of signal propagation in optical fibers with randomly varying birefringence". In: *Journal of Lightwave Technology* 15.9 (1997), pp. 1735–1746.

[150] Nils Langloh, Vassilios Christopoulos, Sofie Van Langendonck, et al. "Optsim: A Tool for the Design of Optical Parallel Computer Architectures". In: *Applications of Photonic Technology 2*. Springer, 1997, pp. 553–561.

[151] René-Jean Essiambre, Gerhard Kramer, Peter J. Winzer, et al. "Capacity limits of optical fiber networks". In: *Journal of Lightwave Technology* 28.4 (2010), pp. 662–701.

[152] Cibby Pulikkaseril, Luke A. Stewart, Michaël A.F. Roelens, et al. "Spectral modeling of channel band shapes in wavelength selective switches". In: *Optics express* 19.9 (2011), pp. 8458–8470.

[153] Glenn Baxter, Steven Frisken, Dmitri Abakoumov, et al. "Highly programmable wavelength selective switch based on liquid crystal on silicon switching elements". In: *2006 Optical Fiber Communication Conference and the National Fiber Optic Engineers Conference*. IEEE. 2006, 3–pp.

[154] Michaël AF Roelens, Steven Frisken, Jeremy A. Bolger, et al. "Dispersion trimming in a reconfigurable wavelength selective switch". In: *Journal of Lightwave Technology* 26.1 (2008), pp. 73–78.

[155] Dan M. Marom, David T. Neilson, Dennis S. Greywall, et al. "Wavelength-selective 1 x K switches using free-space optics and MEMS micromirrors: theory, design, and implementation". In: *Journal of Lightwave Technology* 23.4 (2005), p. 1620.

[156] Christian Malouin, Jon Bennike, and Theodore J Schmidt. "Differential phase-shift keying receiver design applied to strong optical filtering". In: *Journal of Lightwave Technology* 25.11 (2007), pp. 3536–3542.

[157] Timothy M. Schmidl and Don C. Cox. "Robust frequency and timing synchronization for OFDM". In: *IEEE Transactions on Communications* 45.12 (1997), pp. 1613–1621.

[158] Rishad Ahmed Shafik, M.D. Shahriar Rahman, and A.H.M. Razibul Islam. "On the extended relationships among EVM, BER and SNR as performance metrics". In: *ICECE'06. International Conference on Electrical and Computer Engineering*. IEEE. 2006, pp. 408–411.

[159] Alex Alvarado, David J. Ives, Seb J. Savory, et al. "On the impact of optimal modulation and FEC overhead on future optical networks". In: *Journal of Lightwave Technology* 34.9 (2016), pp. 2339–2352.

[160] Paola Parolari, Alberto Gatto, Mariangela Rapisarda, et al. "Preliminary assessment of photonic solutions based on C-band VCSELs for multi-Tb/s metro networks". In: *2020 22nd International Conference on Transparent Optical Networks (ICTON)*. IEEE. 2020, pp. 1–5.

[161] Mariangela Rapisarda, Alberto Gatto, Paolo Martelli, et al. "Impact of chirp in high-capacity optical metro networks employing directly-modulated VCSELs". In: *Photonics*. Vol. 5. 4. Multidisciplinary Digital Publishing Institute. 2018, p. 51.

[162] Sujoy Paul, Christian Gierl, Julijan Cesar, et al. "10-Gb/s direct modulation of widely tunable 1550-nm MEMS VCSEL". In: *IEEE Journal of Selected Topics in Quantum Electronics* 21.6 (2015), pp. 436–443.

[163] Arthur James Lowery and Jean Armstrong. "Orthogonal-frequency-division multiplexing for dispersion compensation of long-haul optical systems". In: *Optics express* 14.6 (2006), pp. 2079–2084.

[164] Dario Pilori, Chris Fludger, and Roberto Gaudino. "Comparing DMT variants in medium-reach 100G optically amplified systems". In: *Journal of Lightwave Technology* 34.14 (2016), pp. 3389–3399.

[165] William A Ling and Ilya Lyubomirsky. "Electronic dispersion compensation in a 50 Gb/s optically unamplified direct-detection receiver enabled by vestigial-sideband orthogonal frequency division multiplexing". In: *Optics Express* 22.6 (2014), pp. 6984–6995.

[166] Paola Parolari, Alberto Gatto, Mariangela Rapisarda, et al. "Effect of filtering in dense WDM metro networks adopting VCSEL-based multi-Tb/s transmitters". In: *2019 21st International Conference on Transparent Optical Networks (ICTON)*. IEEE. 2019, pp. 1–4.

[167] M Svaluto Moreolo, JM Fabrega, L Nadal, et al. "Programmable VCSEL-based photonic system architecture for future agile Tb/s metro networks". In: *Journal of Optical Communications and Networking* 13.2 (2021), A187–A199.

[168] Emilia Pruszyńska-Karbownik and B Mroziewicz Mroziewicz. "Measurements and analysis of antireflection coatings reflectivity related to external cavity lasers". In: *Optics communications* 284.1 (2011), pp. 373–375.

[169] R. G. Broeke, M. Binsma J.J.M. nd Van Geemert, T. De Vries, et al. "Monolithical integration of semiconductor optical amplifiers and passive modefilters for low facet reflectivity". In: *IEEE/LEOS Symp. Benelux Chapter, Brussels, Belgium*. Citeseer. 2001.

[170] Yann Boucher and Ammar Sharaiha. "Spectral properties of amplified spontaneous emission in semiconductor optical amplifiers". In: *IEEE Journal of Quantum Electronics* 36.6 (2000), pp. 708–720.

[171] Enbo Zhou, Xinliang Zhang, and Dexiu Huang. "Analysis on dynamic characteristics of semiconductor optical amplifiers with certain facet reflection based on detailed wideband model". In: *Optics express* 15.14 (2007), pp. 9096–9106.

[172] Michael Connelly. "Semiconductor Optical Amplifiers and their Applications". In: *3rd Spanish Meeting of Optoelectronics, OPTOEL'03* (Aug. 2003), pp. 1–6.

[173] Cristiano M. Gallep and Evandro Conforti. "Reduction of semiconductor optical amplifier switching times by preimpulse step-injected current technique". In: *IEEE Photonics Technology Letters* 14.7 (2002), pp. 902–904.

[174] Ian Armstrong, Ivan Andonovic, and Anthony Kelly. "Semiconductor optical amplifiers: performance and applications in optical packet switching". In: *Journal of Optical Networking* 3.12 (2004), pp. 882–897.

[175] N.A.N.M. Mookran, N.A.M.A. Hambali, M.H.A. Wahid, et al. "Single wavelength fiber laser employing SOA incorporating with a tapered fiber". In: *AIP Conference Proceedings*. Vol. 2045. 1. AIP Publishing LLC. 2018, p. 020043.

[176] Takeshi Matsumoto, Teruo Kurahashi, Ryotaro Konoike, et al. "Hybrid-integration of SOA on silicon photonics platform based on flip-chip bonding". In: *Journal of Lightwave Technology* 37.2 (2018), pp. 307–313.

[177] Lorenzo Occhi. "Semiconductor optical amplifiers made of ridge waveguide bulk InGaAsP/InP: Experimental characterisation and numerical modelling of gain, phase, and noise". PhD thesis. ETH Zurich, 2002.

[178] Jean-Noël Fehr, Marc-André Dupertuis, Thierry P. Hessler, et al. "Hot phonons and Auger related carrier heating in semiconductor optical amplifiers". In: *IEEE journal of quantum electronics* 38.6 (2002), pp. 674–681.

[179] Mostafa Fedawy, M. Bashir Saleh, and Moustafa H. Aly. "SOA Output Characteristics: Effect of Amplifier Length and Injected Carrier Density". In: *Proceedings of the Twenty Third National Radio Science Conference (NRSC'2006)*. IEEE. 2006, pp. 1–7.

[180] Michael J. Connelly. "Wideband semiconductor optical amplifier steady-state numerical model". In: *IEEE Journal of Quantum Electronics* 37.3 (2001), pp. 439–447.

[181] C. Deguet, D. Delprat, G. Crouzel, et al. "Homogeneous buried ridge stripe semiconductor optical amplifier with near polarization independence". In: *Proceedings of European Conference on Optical Communications*. 1999, pp. 46–47.

[182] Paul Adrien Maurice Dirac. "On the theory of quantum mechanics". In: *Proceedings of the Royal Society of London. Series A, Containing Papers of a Mathematical and Physical Character* 112.762 (1926), pp. 661–677.

[183] N.G. Nilsson. "Empirical approximations for the Fermi energy in a semiconductor with parabolic bands". In: *Applied Physics Letters* 33.7 (1978), pp. 653–654.

[184] Brian R. Bennett, Richard A. Soref, and Jesus A. Del Alamo. "Carrier-induced change in refractive index of InP, GaAs and InGaAsP". In: *IEEE Journal of Quantum Electronics* 26.1 (1990), pp. 113–122.

[185] Robert Olshansky, Ching Su, Joanne Manning, et al. "Measurement of radiative and nonradiative recombination rates in InGaAsP and AlGaAs light sources". In: *IEEE Journal of Quantum Electronics* 20.8 (1984), pp. 838–854.

[186] Kenji Sato and Hiromu Toba. "Reduction of mode partition noise by using semiconductor optical amplifiers". In: *IEEE Journal of Selected Topics in Quantum Electronics* 7.2 (2001), pp. 328–333.

[187] Jeremy Miles. "R squared, adjusted R squared". In: *Wiley StatsRef: Statistics Reference Online* (2014).

[188] Osayd M. Kharraz, Abu Sahmah M. Supa'at, Ahmad Fauzi Abas, et al. "Acceleration of carrier lifetime in gain-clamped semiconductor optical amplifiers". In: *IEEE photonics journal* 10.5 (2018), pp. 1–13.

[189] Guido Hunziker, Roberto Paiella, Kerry J. Vahala, et al. "Measurement of the stimulated carrier lifetime in semiconductor optical amplifiers by four-wave mixing of polarized ASE noise". In: *IEEE Photonics Technology Letters* 9.7 (1997), pp. 907–909.

[190] Govind P. Agrawal and N. Anders Olsson. "Self-phase modulation and spectral broadening of optical pulses in semiconductor laser amplifiers". In: *IEEE Journal of Quantum Electronics* 25.11 (1989), pp. 2297–2306.

[191] Ui-Soo Lee, Hyun-Do Jung, and Sang-Kook Han. "Optical single sideband signal generation using phase modulation of semiconductor optical amplifier". In: *IEEE Photonics Technology Letters* 16.5 (2004), pp. 1373–1375.

[192] Tiago G. Silveira, Antonio L.J. Teixeira, Ana P.S. Ferreira, et al. "All-optical vestigial sideband generation using a semiconductor optical amplifier". In: *IEEE photonics technology letters* 18.21 (2006), pp. 2212–2214.

List of Publications

Peer-reviewed papers

1. M. Rapisarda, A. Gatto, P. Martelli, P. Parolari, C. Neumeyr, M. Svaluto Moreolo, J.M. Fabrega, L. Nadal, P. Boffi; **"Impact of Chirp in High-Capacity Optical Metro Networks Employing Directly-Modulated VCSELs"**; *Photonics*, **5**, 51 (2018); DOI:10.3390/photonics5040051;

2. A. Gatto, M. Rapisarda, P. Parolari, P. Boffi; **"Discrete multitone modulation for short-reach mode division multiplexing transmission"**, *Journal of Lightwave Technology*, **37**, 20 (2019); DOI:10.1109/JLT.2019.2929829.

Conference proceedings

1. S. Al Chalabi, M. Rapisarda, A. Gatto, P. Parolari, P. Boffi; **"MDM based on photonic lanterns supported by DMT for MIMO-free short-reach systems**", *IET Conference Publications, FOTONICA 2018 - 20th Italian National Conference on Photonic Technologies* (2018);

2. M. Rapisarda, A. Gatto, P. Parolari, P. Boffi; **"Impact of crosstalk in SDM short-reach systems in presence of multicarrier transmission"**, *ICTON 2018 - 20th International Conference on Transparent*

Optical Networks (2018);

3. A. Gatto, P. Parolari, M. Rapisarda, C. Neumeyr, S. Bhat, G. Delrosso, M. Svaluto Moreolo, J. M. Fabrega, L. Nadal, P. Boffi; **"Disruptive photonic technologies for the future sustainable high-capacity metro network"**, *ICTON 2019 – 21st International Conference on Transparent Optical Networks* (2019);

4. P. Parolari, A. Gatto, M. Rapisarda, C. Neumeyr, M. Svaluto Moreolo, J. M. Fabrega, L. Nadal, P. Boffi; **"Effect of filtering in dense WDM metro networks adopting VCSEL-based multi-Tb/s transmitters"**, *ICTON 2019 – 21st International Conference on Transparent Optical Networks* (2019);

5. A. Gatto, M. Rapisarda, P. Parolari, C. Neumeyr, P. Boffi; **"Beyond 50 Gb/s Directly-Modulated Long Wavelength VCSELs for Next-Gen Access Network"**, *IEEE Photonics Society Summer Topical Meeting Series 2019, SUM 2019* (2019);

6. P. Boffi, P. Parolari, A. Gatto, M. Rapisarda, M. Svaluto Moreolo, L. Nadal, J. M. Fabrega, N. Calabretta, R. Stabile, N. Tessema, D. Larrabeiti, J. P. Fernández-Palacios, G. Otero, C. Neumeyr, G. Delrosso, S. Bhat, K. Solis-Trapala, G. Parladori; **"Multi-Tb/s sustainable MAN scenario enabled by VCSEL-based innovative technological solutions"**, *Proceedings of SPIE - The International Society for Optical Engineering* (2020);

7. J. M. Fabrega, M. Svaluto Moreolo, L. Nadal, R. Martínez, C. Neumeyr, A. Gatto, P. Parolari, M. Rapisarda, P. Boffi; **"Programmable transmission systems using coherent detection enabling multi-Tb/s interfaces for IT-communications convergence in optical networks"**, *Proceedings of SPIE - The International Society for Optical*

Engineering (2020);

8. A. Gatto, M. Rapisarda, P. Parolari, M. Svaluto Moreolo, C. Neumeyr, P. Boffi; **"Long-wavelength VCSEL-based System Exploiting Direct DMT Modulation and Coherent Detection for multi-Tb/s Metro Link"**, *ONDM 2020 – 24th International conference on Optical Network Design and Modelling* (2020);

9. M. Rapisarda, A. Gatto, P. Parolari, N. Tessema, N. Calabretta and P. Boffi; **"SOA impact on high-capacity DMT signals in switching/aggregation node for future MAN"**, *OSA Advanced Photonics Congress* (2020);

10. P. Parolari, A. Gatto, M. Rapisarda, F. Lipparini, C. Neumeyr, M. Svaluto Moreolo, and P. Boffi; **"Preliminary assessment of photonic solutions based on C-band VCSELs for multi-Tb/s metro networks"**, *ICTON 2020 – 22nd International Conference on Transparent Optical Networks.*

Ringraziamenti

Nel corso di questi tre anni di dottorato mi è stata data la possibilità di lavorare nell'ambito di un progetto europeo che mi ha aperto ad esperienze che non avrei mai immaginato prima dell'inizio di questo percorso. Di questo devo ringraziare il prof. Pierpaolo Boffi e la prof.ssa Paola Parolari che, dopo il periodo di tesi, hanno creduto in me e mi hanno permesso di lavorare a questo progetto. Inoltre devo ringraziare il Prof. Paolo Martelli, che è stato un tutor di dottorato sempre presente e disponibile. La mia enorme riconscenza va soprattutto ad Alberto, che nei quattro anni in cui mi ha seguito è stata una guida sempre presente e disponibile con cui scambiare opinioni e consigli anche in ambito extra-accademico. Nulla di tutto questo sarebbe stato possibile senza di lui, quindi grazie infinite. Le lunghe giornate in dipartimento sarebbero state molto più difficili da affrontare senza Alberto, Andrea, Ilaria, Jacopo e Marco, che hanno saputo aiutarmi al bisogno con enorme pazienza. Vi porterò sempre nel cuore. Per tre mesi ho avuto la fortuna di poter lavorare fianco a fianco con il gruppo di ricerca del prof. Nicola Calabretta, che ringrazio insieme a Netsanet per avermi accolto e aiutato in un'esperienza che ritengo molto formativa non solo professionalmente, ma anche umanamente Ringrazio il prof. Maurizio Magarini, il prof. Marco Ferrari ed Eric con cui ho avuto l'onore di collaborare in un interessantissimo progetto che esulava dal mio argomento di dottorato.

Se sono arrivata a raggiungere questo traguardo, sento di dovere tutto alla mia famiglia. Ringrazio mio padre, Giuseppe, per avermi supportato e

per aver condiviso con me gioie e difficoltà di questo percorso. Ringrazio mia madre, Ida, per avermi ascoltata e confortata quando le difficoltà, soprattutto dell'ultimo periodo, mi hanno fatto brancolare nell'incertezza e nell'insicurezza, mettendo spesso da parte i suoi problemi per ascoltare i miei. Ringrazio mio fratello, Eugenio, che è sempre stato per me un punto di riferimento ed un modello per tendere a diventare la persona che vorrei essere. Ringrazio mia sorella non di sangue, Francesca, per essere la persona meravigliosa che è, perché è sempre presente per me con quella discrezione caratteristica solo delle grandi persone come lei. Ringrazio Massimiliano o come dicon tutti Massi, per amarmi con pazienza, nonostante la distanza, nonostante le difficoltà del mio carattere che spesso si è adombrato. Ringrazio tutta la mia famiglia, mia nonna Maria, che ha sempre avuto parole amorevoli per me, i miei zii Lello, Danilo, Roberto e Nellina, che sono da sempre dei punti di riferimento e dei modelli, anche se ho avuto poche occasioni per dir loro ciò che provo. Ringrazio i miei cugini, Giovanni e Rosangela, di cui, nonostante la distanza, sento sempre il supporto. Ringrazio anche quelle persone che non ci sono purtroppo più, ma che sento sempre con me: i miei nonni Eugenio, Angela (di cui ho l'onore di portare il nome) e Franco, che hanno costituito per me esempi di correttezza, professionalità e moralità che spesso si perdono in questi nostri giorni frenetici e un po' maleducati, e mio zio Enzo, che mi ha dato il grande insegnamento di affrontare con dignità le difficoltà che la vita porta con sé. Ringrazio Ivana e Maria, che mi hanno accolto nella loro famiglia come una seconda figlia e nipote: sento che posso sempre contare sul vostro supporto. Ringrazio la famiglia che mi sono scelta, quelle amiche e quegli amici che da più o meno tempo accompagnano la mia vita: Giulia, Agnese, Chiara, Eugenia, Obed, Silvia, Andrea, Jacopo, Marianna, Alessandro, Giulio, Federica, Elena, Sara. So che mi sono scordata qualcuno, ma siete sempre nei miei pensieri: grazie di essermi amici (molti nonostante la distanza).

Infine vorrei ringraziare gli insegnanti che mi hanno formata e hanno creduto

in me. La lista sarebbe realmente troppo lunga per citare tutti, però vi sarò sempre riconoscente.

Questo capitolo si è ormai concluso, ma, qualsiasi cosa mi riservi il futuro, so che avrò sempre il sostegno di coloro che mi vogliono bene e che hanno riempito il mio cuore di affetto.